

INVESTIGATION OF THE THERMAL BOUNDARY
LAYER DEVELOPMENT LENGTH IN UPWARD
HEATED ANNULAR SUPERCRITICAL FLUID
FLOWS

J. W. R. Peeters

Master Thesis
PNR-131-2011-013

Supervisors:
Dr M. Rohde
Dr C. T'Joen

Delft University of Technology
Faculty of Applied Sciences
Department of Radiation Radionuclides & Reactors
Section of Physics of Nuclear Reactors

October 16, 2011

R3
Mekelweg 15
2629 JB Delft

Abstract

The supercritical water reactor is a generation IV reactor design which uses supercritical water as a coolant. Supercritical fluids are unique in that there is no phase change during a heating process. By using supercritical water as a coolant, the reactor design can therefore be kept relatively simple and a higher thermal efficiency (44%) can be attained due to the huge increase in temperature (compared to for example a boiling water reactor).

Heat transfer to supercritical fluids is very different from heat transfer to subcritical fluids, due to sharp variations of the fluid properties with temperature. As a result, well-established heat transfer correlations fail to capture the heat transfer phenomena associated with supercritical fluids. A topic that has not yet been thoroughly investigated as well is the thermal development length of such fluids in channels, pipes and annuli. This is the length, measured from the inlet, it takes for the heat transfer coefficient to become constant.

To investigate this length, a semi analytical and a numerical study were made. For the numerical study, the open source software package OpenFOAM was used. The OpenFOAM code was validated against 18 cases selected from seven different literature sources. Only steady-state and laminar flow conditions were considered in order to focus on the variable property effect on heat transfer. For the investigation of the thermal development length, an annular geometry is chosen, with a constant uniform wall heat flux at the inner wall. The outer wall is considered to be adiabatic. This system can be related to a fuel rod, cooled by supercritical water.

Heat transfer to supercritical CO_2 was extensively investigated. It was found that an increase in heat transfer along the length of the annulus is due to the flow acceleration and the steep increase of the specific heat capacity c_p . An increase in the wall heat flux causes the thermal boundary layer thickness to become smaller, which is due to increasing c_p and decreasing thermal conductivity λ at the wall. Because fully developed flow was not apparent within the investigated domain, the coordinate at which a local increase of heat transfer enhancement occurs and where the inlet effect on heat transfer is no longer apparent is used to quantify the boundary layer behaviour.

This coordinate was investigated for a wide range of mass fluxes and wall heat fluxes. A relationship between system parameters and this coordinate was found for both supercritical CO_2 and supercritical water. The relationships are not able to capture the effect of different inlet temperatures yet.

A method to include the inlet temperature in the relationship is presented for future work. It is also recommended to find similar relations for the prediction of the coordinate where there is a local maximum in heat transfer. If these kind of relationships can also be made for turbulent cases, they will be not only valuable in the design of laminar, but also turbulent supercritical fluid heat transfer equipment.

Acknowledgements

I would like to thank both my supervisors dr M. Rohde and dr C. T'Joel for their guidance and time during this project. Their comments and insights did not only prove to be valuable for a wide range of subjects, but also stimulated me to look critically on my own work. More than once, it happened that I asked them for five minutes of their time, but which resulted in a discussion of over an hour. I would like to thank dr C. T'Joel for providing me with the property-splines that were used in the numerical code, as well.

Nomenclature

Table 1: Regular symbols

a, b	constants in power regression
A, H	matrices in discretized momentum equation
A, B, C, D, E	constants in integral approximation method
c	constant in integral approximation method
c_p	specific heat capacity
d	channel height, pipe diameter, annular hydraulic diameter
f	friction factor
\vec{g}	gravitational acceleration
G	mass flux
h	enthalpy
htc	heat transfer coefficient
I	Unit matrix
K	thermal diffusivity
K_{q_w}''	constant in integral approximation method
K_{T_w}	constant in integral approximation method
L	length
L_{th}	thermal development length
L_{thb}	thermal boundary layer development length
\vec{n}	normal vector
p	total pressure
p_{rgh}	$p - \rho \vec{g} \cdot \vec{x}$
q''	heat flux due to conduction
q_w''	wall heat flux
q'''	volumetric heat production
r	radial coordinate
R_i	inner wall radius
R_o	outer wall radius
T	temperature
T_b	bulk temperature
T_{cr}	critical temperature
T_{pc}	pseudo-critical temperature
T_w	wall temperature
T_{wi}	inner wall temperature
\vec{U}	velocity vector
U	axial velocity component
U_{max}	maximum velocity
U_m	mean velocity
U^*	momentum predictor
V	y-component of the velocity
x	axial coordinate
y	coordinate orthogonal to axial coordinate

Table 2: Greek symbols

β	$= \frac{1}{\rho} \left(\frac{\partial \rho}{\partial T} \right)_{ref}$
γ	$= \frac{1}{c_p} \left(\frac{\partial c_p}{\partial T} \right)_{ref}$
δ	boundary layer thickness
ϵ	$= \frac{1}{\lambda} \left(\frac{\partial \lambda}{\partial T} \right)_{ref}$
ϕ	help variable in OpenFOAM
Φ	viscous dissipation
μ	dynamic viscosity
ρ	density
ψ	representation of property or temperature in spline function
$\vec{\tau}$	stress tensor

Table 3: Dimensionless numbers

Gr	Grashof number, $\frac{\rho^2 g \beta q_w d^4}{\lambda \mu^2}$ or $\frac{\rho^2 g \beta \Delta T d^3}{\lambda \mu^2}$
Nu	Nusselt number, $\frac{h t c d}{\lambda}$
Nu_∞	Nusselt number in the fully developed region
Pe	Peclet number, $\frac{U_m d}{K}$
Pr	Prandtl number, $\frac{\mu c_p}{\lambda}$
Ra	Raleigh number, $Gr Pr$
Re	Reynolds number, $\frac{\rho U_m d}{\mu}$

Contents

1	Introduction	6
1.1	Fluids at supercritical pressures	7
1.1.1	Heat transfer phenomena	9
1.2	Project Goals	10
2	Literature Survey	12
2.1	Laminar constant property flows	12
2.1.1	Heat transfer in annuli	12
2.1.2	Momentum development length in annuli	13
2.2	Laminar mixed convection (sub-critical)	13
2.2.1	M-shaped velocity profile and flow reversal	13
2.2.2	Criteria for flow reversal	14
2.2.3	Non-Boussinesq approximation and flow reversal	15
2.2.4	Heat transfer in laminar mixed convection	16
2.2.5	Development length in laminar mixed convection	16
2.3	Buoyancy induced turbulence	17
2.3.1	Laminar to turbulent transition in annuli	18
2.4	Turbulent mixed convection (sub-critical)	19
2.4.1	Laminarization	19
2.4.2	Thermal development length	20
2.5	Supercritical fluids	21
2.5.1	Supercritical fluids in annuli	21
2.5.2	Low Reynolds number supercritical fluid flows	21
2.6	Summary	22
3	Theory	24
3.1	Navier Stokes equations	24
3.2	Thermal boundary layer thickness	25
3.3	Integral approximation method	26
3.3.1	Constant temperature at the wall	26
3.3.2	constant heat flux at the wall	29
4	Numerical methods	31
4.1	OpenFOAM	31
4.1.1	meshes	31
4.1.2	pressure-velocity coupling with buoyancy effects	32
4.2	Code implementations	34
4.2.1	Equations	34

4.2.2	Implemented boundary conditions	34
4.2.3	supercritical fluid properties	36
4.2.4	post-processing	38
4.3	Code overview	38
4.3.1	boundary conditions overview	38
4.3.2	discretization schemes	38
4.3.3	solvers and preconditioners	39
4.3.4	Relaxation factors	39
4.3.5	code schematic	40
4.3.6	convergence criteria	40
5	Numerical Assessment	42
5.1	Constant property cases	42
5.1.1	Graetz-Nusselt problem in a channel geometry	42
5.1.2	Graetz-Nusselt problem in an annular geometry	44
5.2	Mixed convection of air	47
5.2.1	Mixed convection of air in a flat-plate channel geometry	47
5.3	Fluids at supercritical pressures	51
5.3.1	supercritical carbon dioxide in a pipe geometry at 9.52 MPa	51
5.3.2	supercritical water in a pipe geometry at 23 MPa	59
5.3.3	supercritical water in an annular geometry at 25 MPa	62
5.3.4	supercritical water in a pipe geometry at 25 MPa	64
5.4	Code Performance	65
6	Investigation of the thermal boundary layer thickness in upward heated annular supercritical flows	68
6.1	Analytical considerations	68
6.1.1	Derivation of the thermal boundary layer thickness with variable properties	68
6.1.2	semi-analytical results	71
6.2	Numerical results for supercritical CO ₂	72
6.2.1	Geometry and mesh	73
6.2.2	Numerical results for supercritical CO ₂	73
6.3	Numerical results for supercritical water	81
6.4	Summary and discussion	83
7	Conclusions and Recommendations	85
7.1	Thermal boundary layer development	85
7.1.1	Conclusions	85
7.1.2	Recommendations	86
7.2	OpenFOAM	86
7.2.1	Conclusions	86
7.2.2	Recommendations	87
A	Code excerpts	93

Chapter 1

Introduction

Supercritical fluids are fluids at conditions above the thermodynamic critical point. Such fluids experience sharp property variations and they experience no phase change during a heating process. Supercritical fluids are used in many industrial applications. Some examples include supercritical CO₂ extraction, supercritical boilers (Jiang et al.[22]) and it has even been suggested to use supercritical CO₂ in air-conditioning systems (Lorentzen and Pettersen[31]).

A technological challenge which is very relevant for the future is to meet the growing energy demand due to a growing population, while reducing the exhaust of green-house gases. To help meet that challenge, six new nuclear reactor concepts have been proposed within the Generation IV International Forum. One of these concepts uses supercritical water as a coolant and is therefore called the supercritical water reactor (SCWR). A few of its advantages are: a higher thermal efficiency (44%) due to higher temperatures¹, relatively simple design, much of the technology required is already known (from fossil fuel power plants) and a passive safety system (NERAC and GIF[7]).

In Europe, research on the SCWR has culminated into one design, which is called the High Performance Light Water Reactor. This reactor design operates at a pressure of 25 MPa and at a temperature between 280 °C to 500 °C. Fischer et al.[14] recently proposed a reactor vessel design for the HPLWR. This design is displayed in figure 1.1.

Within the reactor vessel, there are multiple fuel assembly (FA) clusters, which consist each of 9 assembly boxes (shown in figure 1.2). Within each assembly box, there are 40 fuel rods, in which fission takes place. In each fission reaction energy is released, which causes the fuel rod to heat up. In order to utilize the energy released in each fission reaction, the heat of fuel rod is (partially) removed by supercritical water. The supercritical water in turn is heated, which is directly used to drive a turbine after it has left the reactor vessel.

One of the challenges in the design of the HPLWR is to know the exact heat transfer characteristics from the fuel rod to the supercritical water. This is necessary to ensure safe reactor operation (to prevent fuel cladding failure). Because the properties of supercritical fluids vary sharply with temperature,

¹A SCWR typically operates at temperatures 280-500 °C, whereas for example a boiling water reactor operates at temperatures of 269-286 °C Duderstadt[11].

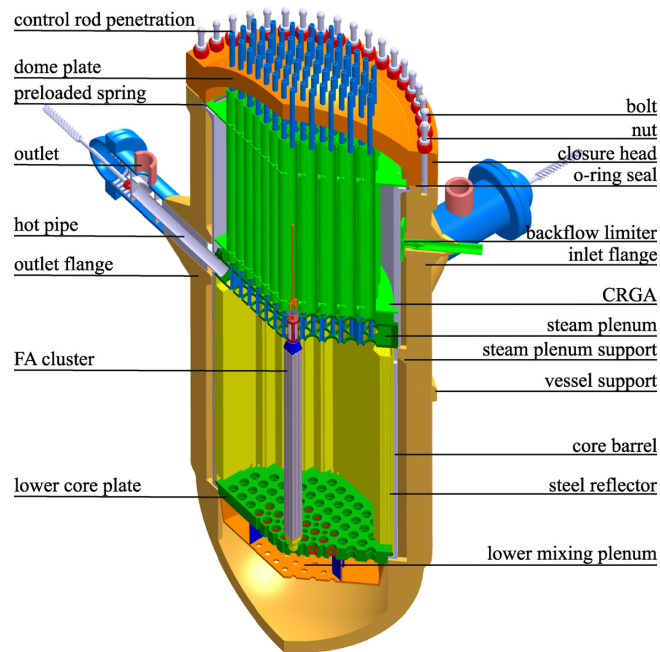


Figure 1.1: Proposed reactor vessel design. Figure adapted from Fischer et al.[14].

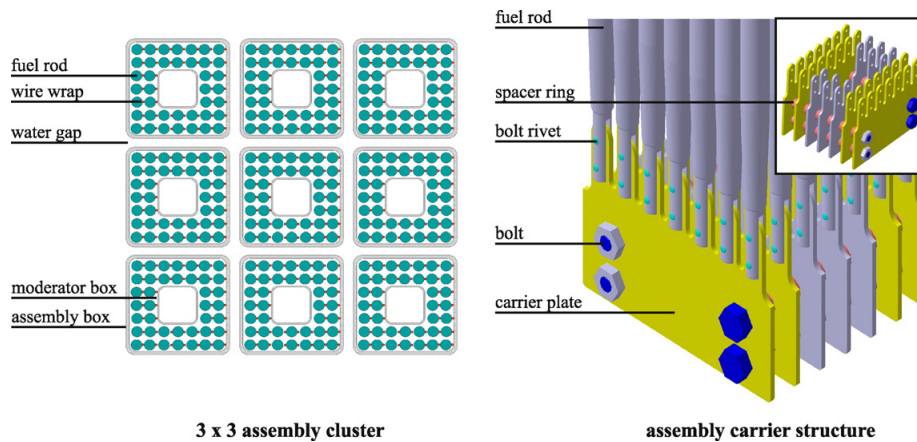


Figure 1.2: Left: cluster consisting of nine assemblies. Right: fuel rod bundle. Figure adapter from Fischer et al.[14].

heat transfer to supercritical fluids is not easily captured with well-established relations and it is, in fact, an area of on-going research.

1.1 Fluids at supercritical pressures

All fluids (and gases) have a point in T,p-coordinates above which the boundary between the gaseous phase and liquid phase no longer exists. This point is called the critical point. Table 1.1 lists the critical points for water and CO₂.

Table 1.1: Critical pressures and temperatures for water and carbondioxide.

Fluid	p_{cr} (MPa)	T_{cr} ($^{\circ}\text{C}$)
Water	22.1	374.0
CO ₂	7.38	31.0

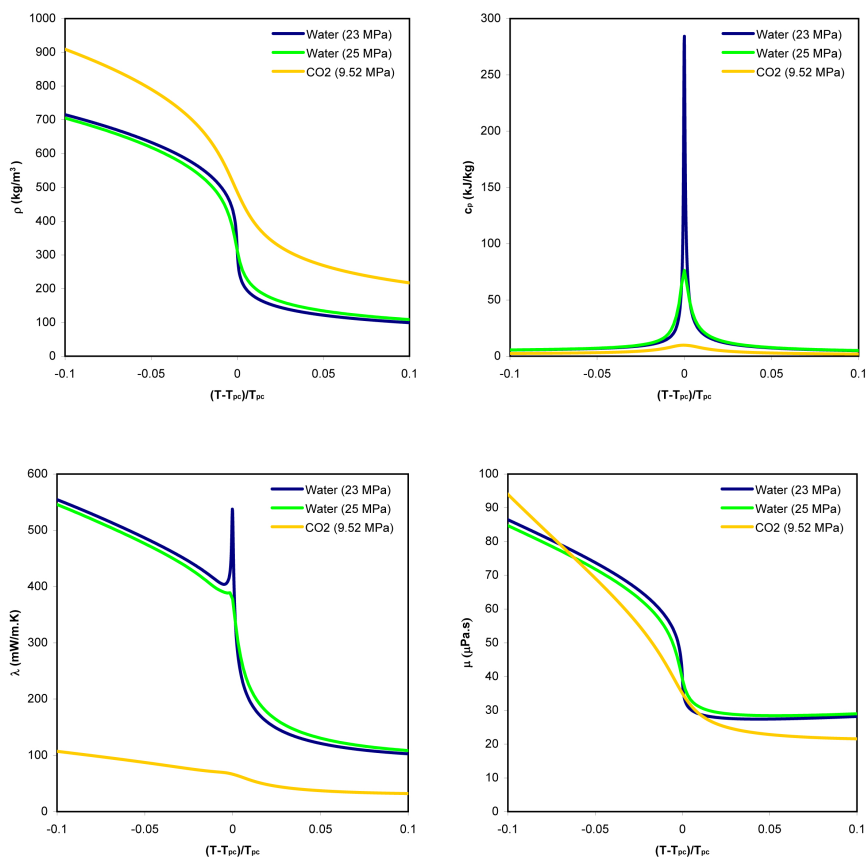


Figure 1.3: Fluid properties of water and CO₂ at supercritical pressures plotted against $(T - T_{pc})/T_{pc}$. Data taken from NIST-Database[51].

A fluid in the thermodynamic supercritical regime is called a supercritical fluid. Although there is no phase change in supercritical fluids, it's properties (ρ , c_p , λ and μ) vary sharply with temperature (or enthalpy). The specific heat capacity shows a peak at the critical point. For pressures higher than p_{cr} , this peak defines the pseudocritical temperature T_{pc} , which is higher than T_{cr} . Around T_{pc} , the properties of the supercritical fluid still vary sharply with temperature, but less so than around T_{cr} . This can be seen in figure 1.3.

The thermal conductivity of water shows a peak value as well. The location of this peak however, is not the same as for specific heat capacity.

1.1.1 Heat transfer phenomena

Fluids with density variations exhibit different flow and heat transfer phenomena compared to constant property fluids. Such flows experience a combination of forced and natural convection, which is called mixed convection (this is discussed in the next chapter). Examples of this are heated gases. Due to the sharp density variation in supercritical fluids, especially near the pseudocritical point, heated supercritical flows share similar flow and heat transfer phenomena with mixed convection. However, because the other properties vary sharply in supercritical flows as well, unique heat transfer phenomena are seen in supercritical fluids.

Comprehensive reviews of heat transfer phenomena in supercritical flows were made by Pioro and Duffey[43], Duffey and Pioro[12] and Pioro et al.[44]. From these surveys, it can readily be seen that most experiments with heat transfer to supercritical fluids (water and carbondioxide) were done at turbulent conditions and within tubes.

In almost all experiments with supercritical fluids, the heat transfer coefficient shows a peak at a certain point along the axial length of the test tube. This peak decreases with an increase in pressure, and occurs when the film temperature, defined as $(T_w + T_b)/2$ is near the pseudo-critical temperature, according to Swenson[49]. Similar results were obtained by Yamagata et al.[56]. They found that the peak occurred when the bulk temperature was near the pseudocritical temperature. This is shown in figure 1.4.

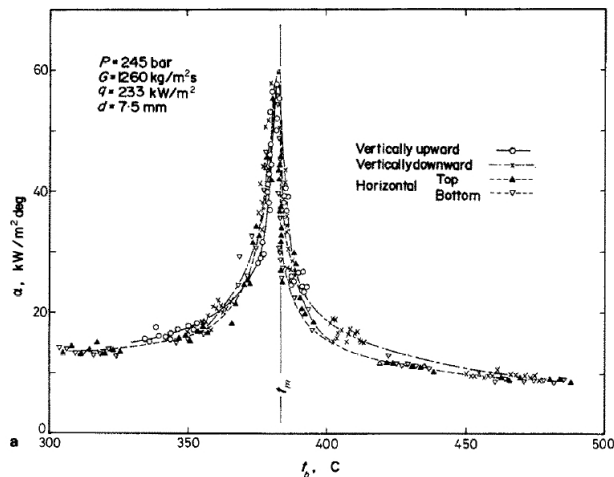


Figure 1.4: Heat transfer to supercritical water flowing through a tube. Figure adapted from Yamagata et al.[56].

Various authors found that if the wall temperature exceeded the pseudocritical temperature, the heat transfer became deteriorated. An example of heat transfer deterioration is shown in figure 1.5; it can be clearly seen that the heat transfer is in the deteriorated regime.

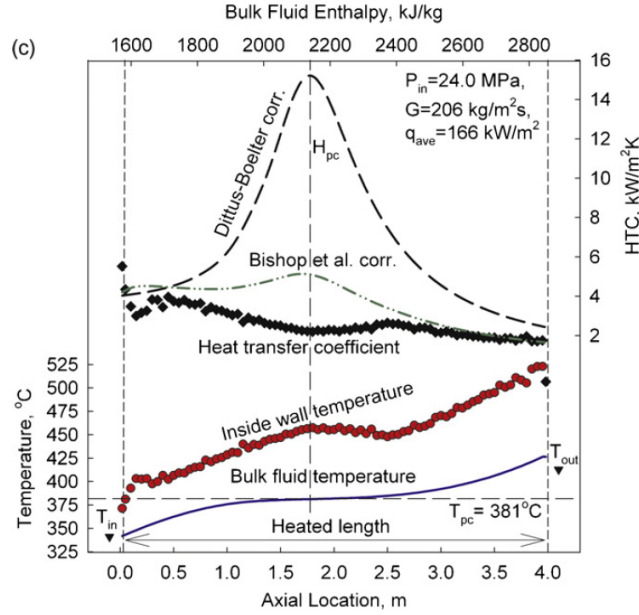


Figure 1.5: Heat transfer to supercritical water flowing through a tube. Figure adapted from Mokry et al.[35].

Various authors proposed criteria for deteriorated² heat transfer. These are summarized in table 1.2:

Table 1.2: Deterioration criteria as found by various authors. ^a Information taken from [12].

Authors	Criterion	Fluid
Vikhrev et al. [52]	$q_w^r/G > 0.49$	Water
Shiralkar and Griffith,[48] ^a	$q_w^r/G > 0.1161$	CO ₂
Ornatsky et al.[40]	$q_w^r/G > 0.95 - 1.05$	Water
Yamagata et al.[56]	$q_w^r = 0.2G^{1/2}$	Water

The table shows that heat transfer deterioration depends on the wall heat flux q_w^r (kJ/kg) and the mass flux G (kg/m²s).

1.2 Project Goals

An often used parameter for the design of heat transfer equipment is the thermal development length (also called the thermal entry length). This is the length it takes for the heat transfer coefficient to become constant (see chapter 3 for more

²Deterioration of heat transfer is not always defined the same manner. Here, the definition given by Piro and Duffey[43] is adopted. There are three modes of heat transfer: normal, deteriorated and enhanced. Normal heat transfer is associated with convection of sub-critical fluids. For these situations, the Dittus-Boelter relations hold. Deteriorated heat transfer (in supercritical fluids) means that the heat transfer coefficient is lower than that of the Dittus-Boelter relation, whereas enhanced means the opposite.

details). The thermal development length marks the region with highest average heat transfer in sub-critical fluid flows. Little has been published regarding the thermal development length in supercritical fluids. Annular geometries are often encountered in heat transfer equipment. Such geometries also bear close resemblance to a single fuel rod in a HPLWR, which is cooled by supercritical water flowing around it. Therefore, the first two objectives of this study are:

1) *to investigate the thermal boundary layer thickness in laminar upward supercritical flows in an annulus*

and

2) *to find a relation between the thermal development length and the system parameters mass flux and wall heat flux.*

Laminar flow conditions were chosen in this study to fully focus on the effects that variable properties (in supercritical fluids) have on the thermal development length and to exclude any effect turbulence might have. To model heat transfer phenomena to supercritical fluids, the (free) open source CFD package OpenFOAM is used, because the source code is completely accessible and modifiable. Because the research group Physics of Nuclear Reactors was unfamiliar with this CFD-package, a third objective of this study is:

3) *to investigate the performance of OpenFOAM, with respect to modelling heat transfer to supercritical fluids.*

In chapter 2, a literature survey is presented. The basic theory underlying the present study is presented in chapter 3. The third goal will be treated in chapter 4 and 5. The first and second goals will be treated in chapter 6. Following chapter 6, the main conclusions are drawn and recommendations for future work are given.

Chapter 2

Literature Survey

In order to understand the heat transfer and flow phenomena associated with annular flow and fluid flows at supercritical conditions, a literature survey was made. The survey starts with fluids in annuli at regular pressures with constant fluid properties. Then, the effect of buoyancy due to changes in density in mixed convection (combined forced and natural convection) is discussed. Finally, a review with respect to fluid flows at supercritical pressures is given.

2.1 Laminar constant property flows

Shah and London[47] provide a comprehensive study on the development length of the thermal and momentum boundary layers in various geometries (including annuli), as well as heat transfer relations valid in the entry region. More recent contributions to the entry length of the thermal and momentum boundary layers were made by Weigand et al.[54] and Poole[45].

2.1.1 Heat transfer in annuli

Weigand et al.[54] derived analytical solutions for the temperature profile in the thermal entrance region of concentric annuli for two sets of boundary conditions. The solutions take the form of summations of eigenvectors with corresponding eigenvalues. No approximations with regard to axial conduction or velocity profile are made¹. Fluid properties are considered to be constant. The Nusselt numbers as a function of the axial length for different Peclet numbers are presented, as well as radial temperature profiles. It is observed that local Nusselt numbers for small Peclet numbers are higher than for cases with high Peclet numbers (negligible axial conduction). Thus, the thermal entrance length is longer for non-negligible axial conduction. In the conclusion, Weigand et al.[54] state that axial heat conduction effects can be ignored for Peclet numbers greater than 80.

¹Axial conduction is usually neglected and the L ev eque approximation is often used. See chapter 3

2.1.2 Momentum development length in annuli

Poole[45] describes a method to calculate the development length of a momentum boundary layer for fully developed laminar flow in concentric annuli. By using a characteristic length h^* , a single relation can be used for annuli with different inner/outer radius ratios $N = R_i/R_o$. The modified characteristic length h^* is defined as:

$$h^*/h = -0.119 \ln(N) + 1 \quad (2.1)$$

in which h is the width of the annular gap. In conjunction with a relation by Durst et al.[13] valid for two-dimensional channels, the development length X_D for annular channels is accurately described by:

$$X_D/h^* = ((0.631)^{1.6} + (0.0442Re)^{1.6})^{1/1.6} \quad (2.2)$$

Poole's results are interesting because he shows that the development of the momentum boundary layer for $N > 0.5$ is the same as in parallel flat-plate channels, which makes equation 2.1 redundant for annuli for which $N > 0.5$ holds. The same is noted for heat transfer in Weigand et al.[54].

2.2 Laminar mixed convection (sub-critical)

Mixed convection is a combination of forced convection and natural convection. It occurs in forced convection flows which are heated and for which density differences are not negligible. Mixed convection has been investigated by various authors.

2.2.1 M-shaped velocity profile and flow reversal

Hanratty et al.[18] studied heat transfer in mixed convection numerically and experimentally at low Reynolds numbers. They derived the steady-state velocity and temperature profiles at a distance far from the entry of the tube analytically by using the Boussinesq approximation. In these derivations, it is shown that for different Gr/Re numbers, the velocity near the wall is increased, while the velocity in the center is decreased, compared to a constant properties fully developed profile. For a certain value of Gr/Re (ratio of buoyancy over inertia forces), the velocity in the center is lower than the velocity of the fluid near the wall. This is called a M-shaped velocity profile. For $Gr/Re > 121.6$ in upward flow with a constant wall heat flux, the velocity in the center becomes even negative. This is called flow reversal. The M-shaped velocity profile and flow reversal analytical results by Hanratty et al.[18] are shown in figure 2.1

The flow reversal phenomenon was visualized by using a dye-injection method. In their experiments, a downward flow can clearly be seen, as well as flow instability far downstream from the inlet. This instability is discussed in the next section.

The phenomenon of flow-reversal is an on-going research subject: recent analytical solutions for fully developed mixed convection in 3-dimensional ducts with different boundary conditions were derived by Barletta[2]. You et al. [57] reproduced the analytical work of Hanratty et al.[18] using CFD-methods (DNS).

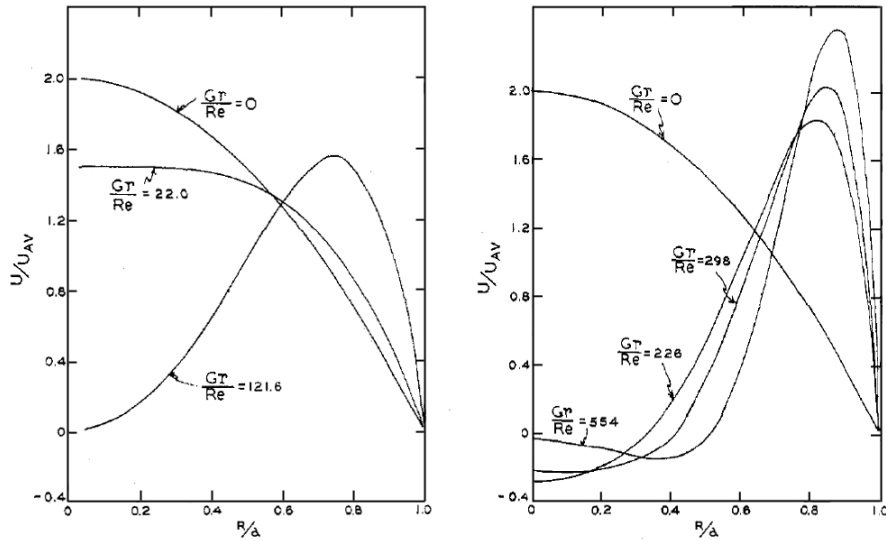


Figure 2.1: Analytical mixed convection velocity profile results. Figure adapted from [18].

2.2.2 Criteria for flow reversal

Wang et al.[53] further investigated the phenomenon of flow reversal in horizontal and vertical pipes at low Peclet numbers in the thermal entrance region with CFD. Density variations are modelled using the Boussinesq approximation. Numerical results are given for velocity and temperature profiles, as well as Nusselt and friction factors. The paper also describes a map in $(Pe-Gr/Re)$ coordinates) in which flow reversal occurs. For relatively low Peclet numbers, larger Grashof numbers are necessary for flow reversal to occur, compared to high Peclet numbers. For relatively high Peclet numbers ($Pe > 50$), the occurrence of flow reversal depends only on Gr/Re . The conditions for which flow reversal occurs (in $Pe-Gr/Re$ coordinates) are shown in figure 2.2.

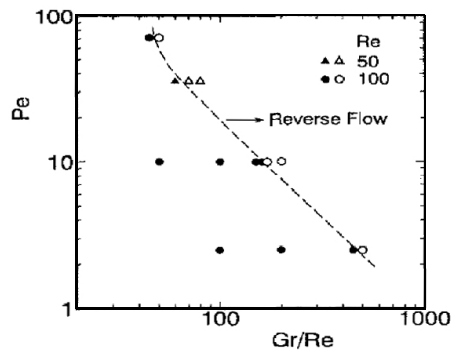


Figure 2.2: Flow reversal map for mixed convection in upward tube flows. Figure adapted from Wang et al.[53].

Desrayaud and Lauriat[10] did a comparable numerical study as Wang et al.[53] for higher Peclet numbers and vertical flat-plate channels. Results are presented for mixed convection of air for various Reynolds and Grashof numbers. The Boussinesq approximation is used here as well. Isothermal boundary conditions are used with $T_w > T_{in}$. It is mentioned that for these boundary conditions, flow reversal can only occur in the thermal developing region. This is very different from cases with a uniform wall heat flux, for which fully developed bi-directional flow can exist.

Desrayaud and Lauriat[10] also identified a flow reversal map in $Pe-Gr/Re$ coordinates. For Peclet numbers higher than 200, the occurrence of flow reversal was found to be independent of the Pe-number. Their criterion for the occurrence of flow reversal is summarized as $Gr/Re \approx 300$. The regime is shown in figure 2.3. The critical location (measured from the inlet) for flow reversal was found to be $x/dRe \approx 0.007$ for vertical flat-plate channels with isothermal boundary conditions, which is substantially lower than what is reported by Moutsoglou and Kwon[36]: $x/dRe \approx 0.016$ for vertical pipes, with a uniform heat flux.

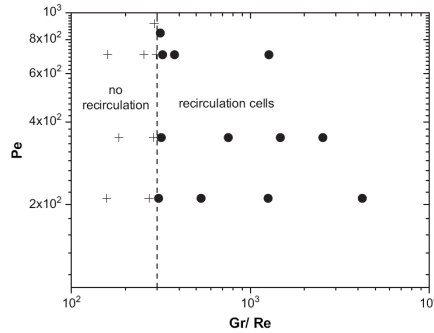


Figure 2.3: Flow reversal map for mixed convection in upward tube flows. Figure adapted from Desrayaud and Lauriat[10].

From the results of Wang et al.[53] and Desrayaud and Lauriat[10], it can be concluded that for high Peclet numbers, the occurrence of flow reversal depends only on Gr/Re .

2.2.3 Non-Boussinesq approximation and flow reversal

Nesreddine et al.[38] numerically investigated mixed convection of air in vertical tubes with both the Boussinesq approximation as well as a variable properties model. Differences between both models can clearly be seen in velocity and temperature profiles, as well as Nusselt numbers and friction factors for $Gr > 10^5$. The phenomenon of flow reversal is more apparent using the Boussinesq approximation. From this paper, it can be concluded that, in order to properly model flow reversal due to high Gr -numbers, variations in properties other than density must be taken into account as well. The investigation of Nesreddine et al.[38] shows that the previously mentioned criteria for the occurrence of flow reversal, or the location of flow reversal are only valid if the Boussinesq approximation is valid.

2.2.4 Heat transfer in laminar mixed convection

Hanratty et al.[18] state that an increase in heat transfer is seen for $Gr/Re > 22$, or when the velocity profile has a ‘dimple’ in the center, for fully developed flow and thermal profiles and a uniform wall heat flux. Nesreddine et al.[38] showed that for a higher wall heat flux, the Nusselt number is increased along the entire axis of a tube (not just far away from the inlet, where the flow is fully-developed). In Wang et al.[53], it is observed that for upward flow through pipes with $T_w > T_{in}$, the radially averaged Nusselt numbers are increased for larger numbers of Gr/Re , due to buoyancy, especially in the region where flow reversal occurs. Similar results were found by Desrayaud and Lauriat[10]. These results are shown in figure 2.4.

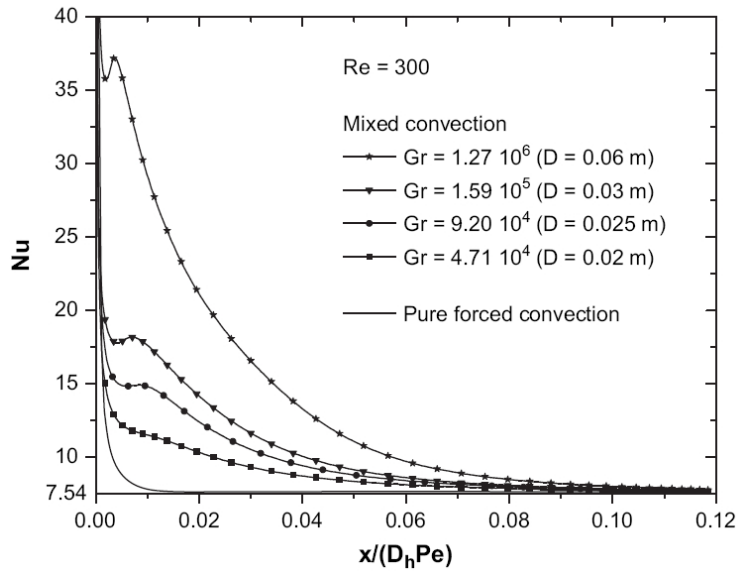


Figure 2.4: Radially averaged Nusselt number as a function of the axial coordinate in a parallel plate-channel. Shown are the mixed convection case as well as a forced convection (constant properties) case. Figure adapted from Desrayaud and Lauriat[10].

2.2.5 Development length in laminar mixed convection

From the Nusselt numbers presented by Desrayaud and Lauriat[10], it can be concluded that the development length in mixed convection is much longer than for constant property cases if the development length is defined as the axial coordinate at which the Nusselt number has become constant. The results of Nesreddine et al.[38] suggest the same, but for cases with a uniform wall heat flux.

Cheng et al.[6] numerically investigated the thermal development length in horizontal rectangular channels with a uniform wall heat flux. Buoyancy is accounted for by means of the Boussinesq approximation. They found a minimum Nusselt number along the axial length of the channel, after which Nu converged to a constant value. The local minima they found are due to secondary flow. For

larger Raleigh numbers ($Ra = GrPr$), the thermal development length becomes smaller. Buoyancy effects have a negligible effect on the thermal development length for $Ra < 10^3$. These effects can be seen in figure 2.5.

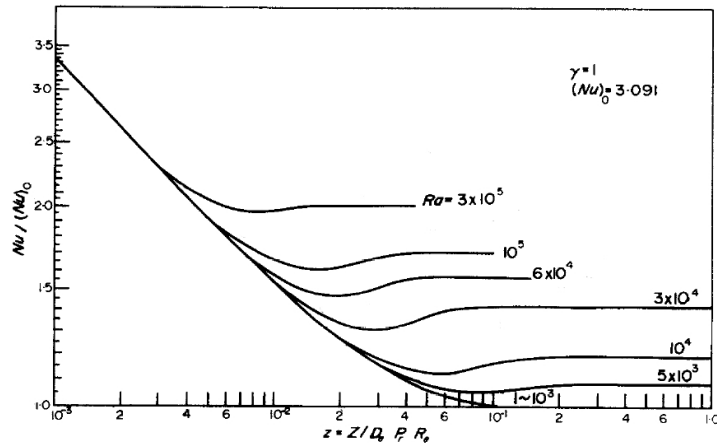


Figure 2.5: Nusselt number as a function of the axial coordinate in a square channel with a ratio $\gamma = 1$. Figure adapted from Cheng et al.[6].

The results of Cheng et al.[6], Desrayaud and Lauriat[10] and Nesreddine et al.[38] show that the thermal development length is a function of both the mass flux as well as the wall heat flux. It can be concluded here that the thermal development length is longer for upward heated mixed convection flows, compared to constant property flows and that it is shorter for horizontal mixed convection flows.

2.3 Buoyancy induced turbulence

Hanratty et al.[18] found in their experiments that far downstream from the point at which flow reversal occurred, the flow became unstable. Bernier and Baliga[4] did similar experiments as Hanratty et al.[18]. They successfully visualized recirculation cells in upward mixed convection in a pipe with a uniform wall heat flux. Bernier and Baliga[4] discuss the same phenomena as Hanratty et al.[18], but produced a better visualization. An example of flow reversal and associated instability far downstream is shown in figure 2.6.

Both Hanratty et al.[18] and Bernier and Baliga[4] found a transition from laminar to turbulent flows due to buoyancy in low Reynolds number flows. Holman[19]² reports that the critical Reynolds number Re_{cr} for the transition from laminar to turbulent flows becomes smaller with increasing buoyancy. Holman[19] states that this can be as low as $Re_{cr}=200$. Hanratty et al.[18] and Bernier and Baliga[4] visualized turbulence³ due to buoyancy for $Gr = 5 \cdot 10^5$, $Gr = 7 \cdot 10^4$ and $Gr = 9.5 \cdot 10^4$ for $Re=125$, 72 and 48, respectively. These

²Information taken from Jiang et al.[22]

³Hanratty et al.[18] speak of flow instability, whereas Bernier and Baliga[4] speak of turbulence. It is assumed here that they are the same.

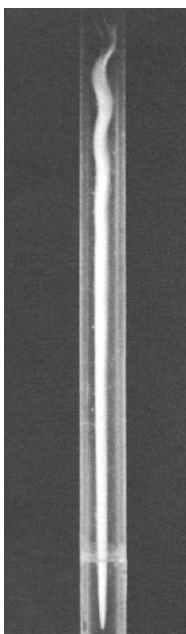


Figure 2.6: Visualization of flow reversal and laminar-turbulent transition in upward heated pipe flow. $Pr = 6$, $Re = 48$, $Gr = 95000$.

results show that Re_{cr} can be lower than 200. Petukhov et al.[42]⁴ also reports that the occurrence of flow reversal will result in the transition from laminar to turbulent flow conditions.

Behzadmehr et al.[3] investigated the onset of turbulence in heated upward flows of air in a tube. They found that the flow becomes unstable for $Gr = 8 \cdot 10^6$ and $Gr = 2 \cdot 10^6$ for $Re=1000$ and 1500 respectively.

2.3.1 Laminar to turbulent transition in annuli

Lu and Wang[32] carried out experiments in order to study the transition from laminar to turbulent flow in narrow annuli in mixed convection. The test section consists of a tube-in-tube heat exchanger. Single-phase water flows in both the tube and the annulus in opposite directions (counter-current configuration). The annulus is concentric. The hot water enters the inner tube at $60^\circ C$ or $80^\circ C$, whereas the cold water enters the annulus at $20^\circ C$. The flow direction is either upward, horizontal or downward. Nusselt numbers based on the hot wall of the annulus are compared for different Reynolds numbers with literature. It is found that for $Re < 150$, the Nusselt numbers are smaller than data from literature. This is called heat-transfer deterioration in Lu and Wang[32]. For $Re=800-1200$, transition from laminar to turbulent heat transfer occurs. This is shown in figure 2.7.

Lu and Wang[33] investigated the transition of laminar to turbulent flow as well, by looking at the friction factor for various Reynolds numbers (using the

⁴Information taken from Jiang et al.[21]

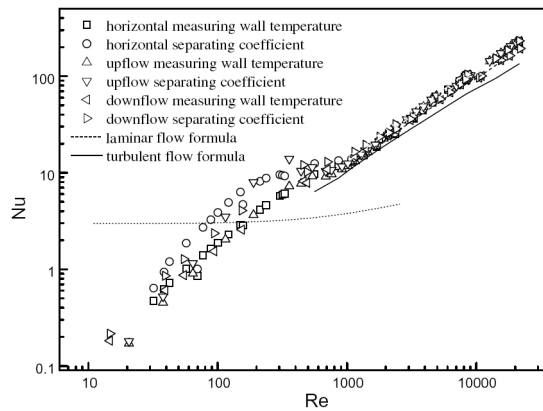


Figure 2.7: Calculated Nusselt numbers for three flow directions. Figure adapted from Lu and Wang[32].

same methods as in Lu and Wang[32]). It is found that for isothermal flows, the critical Reynolds number for the transition from laminar to transitional turbulent flows is around 2000, which is consistent with literature[5]. However, with heat exchange the transition takes place at $Re=1100-1500$ for horizontal and downward flow directions. Unfortunately, upward flow data is not presented. Also, no Gr numbers are presented in Lu and Wang[33]

2.4 Turbulent mixed convection (sub-critical)

2.4.1 Laminarization

Tanaka et al.[50] investigated the laminar and turbulent regimes in mixed convection of nitrogen gas at a pressure of 5 MPa. They predicted a boundary between laminar and turbulent flows in $Re-Gr$ coordinates. Their semi-theoretical predictions and numerical results are substantiated by experiments. Their results are shown in figure 2.8. Boundaries between forced convection and mixed convection were defined at a measured or calculated Nusselt number of 80% of the Nusselt number for forced convection with the same Reynolds number. Their results show that buoyancy in turbulent or transitional flows can cause the flow to laminarize.

Behzadmehr et al.[3] found in their investigations that (re-) laminarization occurred for $Gr = 5 \cdot 10^7$ and $Gr = 10^8$. The results for the occurrence of turbulence of Behzadmehr et al.[3], as well as those of Hanratty et al.[18] and Bernier and Baliga[4] are not included in the results by Tanaka et al.[50]. They do, however, suggest that a turbulent mixed convection regime roughly exists for $Re < 1500$ and $Gr > 5 \cdot 10^5$. These results are plotted in figure 2.8 as well. Hall and Jackson[16] proposed a criterion for the onset of buoyancy effects in fully developed turbulent pipe flow, based on analytical and experimental work:⁵:

⁵Information taken from Mikielwicz[34].

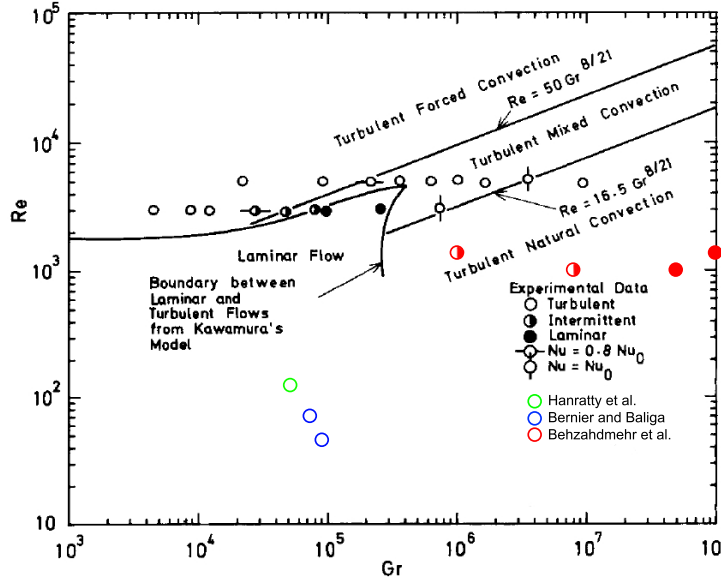


Figure 2.8: Experimental data plotted on semi-theoretically derived regime map for forced, mixed and natural convection. Figure adapted from Tanaka et al.[50]. Results from Behzadmehr et al.[3], Bernier and Baliga[4] and Hanratty et al.[18] are plotted as well. Re is calculated with properties evaluated at the film-temperature. This is not the case for Behzadmehr et al.[3], Bernier and Baliga[4] and Hanratty et al.[18].

$$Bo = \frac{Gr}{Re_b^{3.5} Pr^{0.8}} < 5.6 \cdot 10^{-7} \quad (2.3)$$

This number is also known as the buoyancy number. This shows that buoyancy effects are a function of the wall heat flux.

To further discuss the phenomenon of laminarization goes beyond the scope of this work. For more information, the reader is encouraged to look up (for example) Hall and Jackson[16] and Jackson et al.[20]. However, it can be concluded here that buoyancy has different effects on the velocity profile in laminar and turbulent cases. A clear criterion for buoyancy induced turbulence has not been found, in contrast to a criterion for laminarization.

2.4.2 Thermal development length

Keshmiri[25] investigated the heat transfer at transitional Reynolds numbers (> 2300) with buoyancy effects. Changes in density were modelled with the Boussinesq approximation. Turbulence is modelled according to the $\kappa - \epsilon$ Launder and Sharma model. It was found by Keshmiri[25] that the development length is much longer than for constant property cases, based on the Nusselt number and friction factor.

2.5 Supercritical fluids

2.5.1 Supercritical fluids in annuli

Supercritical fluids heated in annuli were investigated less than supercritical fluids in tubes. Glushchenko et al.[15]⁶ investigated water flowing upward through an annulus, which was heated internally and externally. The results show that the wall temperature profiles of tubes and annuli are similar.

More recent experimental investigations on the heat transfer in supercritical fluids in an annulus were done by Kim et al.[26] The annulus consists of an outer tube with an inner diameter of 10 mm and a heated inner rod with an outside diameter of 8 mm. The inner rod is heated over a length of 1.8 m by means of an alternating current. By measuring the outer wall temperatures, the heat transfer coefficient along the axial length was calculated. It can be seen in their results that there is a peak when the bulk enthalpy is slightly lower than the pseudo-critical enthalpy. This is consistent with the experimental results from Yamagata et al.[56]. Kim et al.[26] state that heat transfer deterioration occurs for $q_w''/G=0.125$ kJ/kg. They report the same value for supercritical CO₂ flowing upward in a heated tube. For $q_w''/G=0.125$, the heat transfer coefficient is slightly higher than for the tube. This is not the case for lower heat fluxes. Bae and Kim[1] report the same q_w''/G value for the deterioration of heat transfer. Licht et al.[28] did experiments with supercritical water at a pressure of 25 MPa flowing upwards through an annulus. Their annulus consists of a tube with an inner diameter of 4.29 cm and a heater rod with a diameter of 1.07 cm. Bulk inlet temperatures were tested from 300 °C up to 400 °C. Licht et al.[28] found that the heat transfer coefficient showed a peak near the pseudo-critical temperature. For higher heat fluxes, the magnitude of the peak decreases. These phenomena are very similar (at a qualitative level) with experiments by Yamagata et al.[56].

2.5.2 Low Reynolds number supercritical fluid flows

Most investigations on low Reynolds number supercritical flows are numerical. Jiang et al.[21] numerically investigated velocity profiles, temperature profiles and Nusselt numbers in the thermal developing region for a pipe with a constant wall temperature or uniform wall heat flux at a Reynolds number of 1000. In the velocity profiles it is seen that the fluid near the hot wall is accelerated, giving the velocity profile an M-shape. It can also be seen that flow reversal can occur. The local heat transfer coefficient is enhanced in upward heated flows.

Jiang et al.[22] did experiments with supercritical CO₂ flowing upwards through a heated pipe with a diameter of 2 mm. They calculated heat transfer coefficients by measuring the outer wall temperature of the pipe in his experimental set-up and together with a diffusion equation for temperature he calculated the inner wall temperatures. The bulk temperature was calculated by solving the 1-dimensional enthalpy equation. Experimental values of the heat transfer coefficients are presented for different wall heat fluxes and mass fluxes. In these experiments the Reynolds number varies from 1900-2360. The results of Jiang et al.[22] show a local increase in heat transfer, which is attributed to a transition from laminar to turbulent flow. This is partially substantiated by

⁶Information taken from Pioro and Duffey[43].

numerical simulation with a $k - \epsilon$ Launder Sharma model, by comparing the wall temperature measured in the experiments and the wall temperature from the numerical simulation. The results of Jiang et al.[22] are further discussed in chapter 5.

Similar results are reported by Jiang et al.[23] with a different experimental set-up (pipe with an inside diameter of 0.27 mm) for $Re=1900-2900$. For upwards flows of supercritical CO_2 , there is also a local increase in heat transfer, which was seen in turbulent supercritical heated flows as well (see section 1.1.1).

Xu et al.[55] numerically considered developing laminar mixed convection of supercritical water at 23 MPa. The paper describes a relatively simple case, suited to use as validation for the OpenFOAM code. This is discussed further in chapter 5.

Zaim et al.[58] provide a more in depth study of supercritical water (25 MPa) flowing upwards through an annulus. A few of their results are discussed in chapter 5 as well.

Dang and Hihara[8] numerically investigated heat transfer to supercritical CO_2 (8 MPa) and water (23.6 MPa) in a horizontal pipe. Heating and cooling cases (negative wall heat flux) are investigated for different values of the mass flux and the wall heat flux. Nusselt numbers for these cases are compared with the Nusselt number for fully developed pipe flow (Nu_∞). For heating cases, Nu attained a maximum if $T_b < T_{pc}$. A correlation for the prediction of the Nusselt number was proposed. It must be noted here, however, that Dang and Hihara[8] impose a fully developed velocity and thermal profile as a boundary condition at the outlet. They do not justify these choices of boundary conditions.

2.6 Summary

In laminar upward heated flows with non-negligible density variations, an M-shaped velocity profile is seen. This causes an increase in heat transfer. For strong heating, flow reversal might occur, which in turn can induce a transition to turbulent flow. For these kinds of flows, the thermal development length is longer than for constant property flows. For horizontal channels, the development length becomes shorter. Heat transfer phenomena in mixed convection is function of both mass flux and wall heat flux or wall temperature.

Because the density decreases with temperature in such fluids, laminar upward heated supercritical flows can also have an M-shaped profile. Local heat transfer coefficients are enhanced in laminar supercritical flows compared to constant property flows. A local maximum in heat transfer coefficients occurs if T_b is close to T_{pc} . This is very different from turbulent supercritical upward heated flows: due to laminarization of the fluid, the heat transfer coefficient can be lower compared to heat transfer coefficients to sub-critical fluid flows.

The literature survey has also been summarized in table 2.1.

Table 2.1: Literature survey schematic. 1) experimental, 2) numerical, 3) analytical, 4) comprehensive survey a) M-shape, b) Flow Reversal, c) Development Length, d) CO₂, e) water, f) Annulus.

	Constant		Mixed Convection			Supercritical fluids	
	Laminar	Laminar	Turbulent	Transitional	Low Re	High Re	
Momentum	[45] ^c , [47] ^{4c} , [9] ^{34c} , [37] ^{34c}	[18] ^{123ab} , [36] ^{2b} , [53] ^{2b} , [10] ^{2b} , [57] ^{2a}	[50] ¹³ , [16] ³ , [3] ² , [57] ^{2a}	[3] ² , [33] ^{1f} , [4] ^{1b}	[22] ^{12d} , [55] ^{2ae} , [23] ^{1d} , [21] ^{abe} , [58] ^{ef}		
Heat transfer	[54] ^{3f} , [47] ^{4c} , [9] ^{34c} , [37] ^{34c}	[18] ^{123ab} , [53] ^{2b} , [10] ^{2bc} , [38] ^{2c}	[25] ^{2c}	[50] ¹³ , [32] ^{1f} , [3] ²	[22] ^{12d} , [55] ^{2ae} , [23] ^{1d} , [21] ^{abe} , [58] ^{ef} , [8] ²	[44] ^{4de} , [12] ^{4d} , [43] ^{4e} , [56] ^{1e} , [52] ^{1e} , [48] ^{1d} , [40] ^{1e} , [35] ^{1e} , [15] ^{1ef} , [26] ^{1df} , [1] ^{1df} , [28] ^{1ef}	

Chapter 3

Theory

3.1 Navier Stokes equations

The motion of fluids in general and associated heat transfer phenomena are governed by the Navier-Stokes equations. These equations are conservation balances for mass, momentum and enthalpy. For steady state flow, these equations for the conservation of mass, momentum and enthalpy read:

$$\nabla \cdot \rho \vec{U} = 0 \quad (3.1)$$

$$\nabla \cdot \rho \vec{U} \vec{U} = \nabla \cdot \vec{\tau} - \nabla p + \rho \vec{g} \quad (3.2)$$

where $\vec{\tau}$ is defined as:

$$\vec{\tau} = \mu \left((\nabla \vec{U}) + (\nabla \vec{U})^T - \frac{2}{3} (\nabla \cdot \vec{U}) I \right) \quad (3.3)$$

$$\nabla \cdot (\rho U h) = -\nabla \cdot \vec{q} + q''' + p(\nabla \cdot \vec{U}) + \Phi \quad (3.4)$$

In these equations is ρ the density (kg/m³), \vec{U} the velocity (m/s), p the pressure, g the gravitational acceleration, μ the viscosity (kg/m.s), I the unit matrix, h the enthalpy (J/kg), λ the thermal conductivity (W/m.K), c_p the specific heat capacity (J/kg.K), \vec{q} the heat flux due to conduction, Φ the viscous dissipation in (W/m³) and q''' the heat production in (W/m³). These equations can not be solved analytically, unless approximations are used. Without approximations, numerical methods are needed.

If the fluid has variable properties, equation 3.4 can be rewritten using $dh = c_p dT + (1 - \beta T) \frac{dp}{\rho}$ (see Todreas[37] for a derivation¹) and using $\vec{q} = -\lambda \nabla T$:

$$\nabla \cdot (\rho U h) = \nabla \cdot \left(\frac{\lambda}{c_p} \nabla h \right) - \nabla \cdot \left(\left(\frac{\lambda(1 - \beta T)}{\rho c_p} \right) \nabla p \right) + p(\nabla \cdot \vec{U}) + \Phi + q''' \quad (3.5)$$

This equation will be used in chapter 4. If the properties of the fluid are constant, however, $dh = c_p dT$, and equation 3.4 becomes:

¹ $\beta = \frac{1}{\rho} \left(\frac{\partial \rho}{\partial T} \right)_p$

$$\nabla \cdot \rho c_p \mathbf{U} T = \nabla \cdot \lambda \nabla T + p(\nabla \cdot \vec{U}) + \Phi + q''' \quad (3.6)$$

An approximation method for the solution of equation 3.6 is presented in section 3.3. Before that, however, an introduction in to the thermal boundary layer is given:

3.2 Thermal boundary layer thickness

One of the goals of this project is to investigate the thermal boundary layer thickness in supercritical fluids. The thermal boundary layer is first defined here, to avoid any confusion later on. Consider a fluid entering a channel with a fully developed profile and a uniform temperature T_{in} . The fluid near the wall is heated; either by a uniform temperature T_w or a uniform heat flux q_w'' (see figure 3.1).

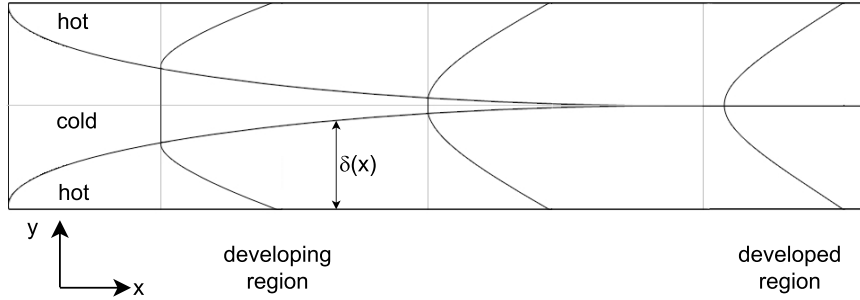


Figure 3.1: graphic representation of a developing temperature profile in a horizontal channel.

In this figure, the boundary between the hot and cold fluid is shown. Superimposed on the channel are three temperature profiles. Very near the inlet, it can be seen that only fluid very near the wall is raised in temperature. Moving along the axial coordinate x , the heat penetrates deeper and deeper into the fluid, up to the point where the temperature at the centerline starts to increase. Some distance away from this point, the temperature profile does not change any more (or very little); the temperature profile is considered to be fully developed here. The distance from the inlet up to this point is called the thermal developing length, or the thermal entry length. The distance from the heated wall up to a point in the fluid where the temperature equals that of the inlet is called the boundary layer thickness $\delta(x)$. The thermal development length is related to the heat transfer coefficient:

$$htc = \frac{q_w''}{T_w - T_b} \quad (3.7)$$

in which T_b is defined as:

$$Tb(x) = \frac{\int_0^d U(y)T(x,y)dy}{\int_0^d U(y)dy} \quad (3.8)$$

The htc shows a sharp decrease in the developing region and it is constant in the developed region. It can be regarded as a measure of how well the heat transfer actually is. It contains information of the heat transfer through convection and conduction (in this case).

3.3 Integral approximation method

For steady-state laminar Newtonian flow without viscous dissipation and no internal heat production, the Navier-Stokes equations are:

$$\nabla \cdot \mu \nabla \mathbf{U} = \nabla p \quad (3.9)$$

$$\nabla \cdot \rho c_p \mathbf{U} T = -\nabla \cdot \lambda \nabla T \quad (3.10)$$

For two dimensional laminar channel flow with an inlet temperature T_{in} that is different from the wall temperature T_w , the temperature equation reduces to:

$$\frac{\partial}{\partial x} \rho c_p U T = \frac{\partial}{\partial y} \lambda \frac{\partial T}{\partial y} \quad (3.11)$$

In this equation, U [m/s] is the axial velocity component. This approximation holds if $Pe = \frac{\rho c_p u d}{\lambda} \gg 1$ (Deen[9]). There are various ways of solving this equation. The integral approximation method is used here as it an intuitive method² for determining the thermal development length, as well as the profile of the Nusselt number as a function of the axial position. The first step is to assume a general function for the temperature, dependent on both the axial and channel height coordinates, x and y respectively. This is done below for two cases: constant wall temperature and constant wall heat flux. The cases are graphically represented in figure 3.2.

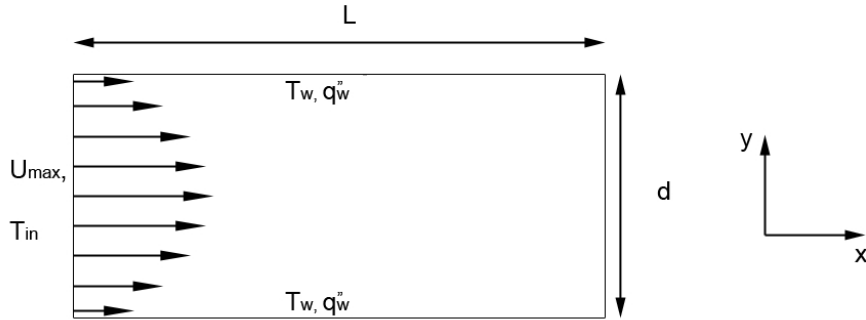


Figure 3.2: graphic representation of the case studied.

3.3.1 Constant temperature at the wall

The following function is proposed for a case with a constant wall temperature:

²It is called intuitive here, because the boundary layer thickness $\delta(x)$ is directly solved.

$$\frac{T - T_{in}}{T_w - T_{in}} = A + B \left(\frac{y}{\delta(x)} \right) + C \left(\frac{y}{\delta(x)} \right)^2 + D \left(\frac{y}{\delta(x)} \right)^3 + E \left(\frac{y}{\delta(x)} \right)^4 \quad (3.12)$$

In which T_{in} is the inlet temperature, T_w the wall temperature and $\delta(x)$ the thermal boundary layer thickness. This equation has five unknowns. Thus, 5 boundary conditions are needed. To find these, a graphic representation of the temperature profile within the developing region is shown in figure 3.3.

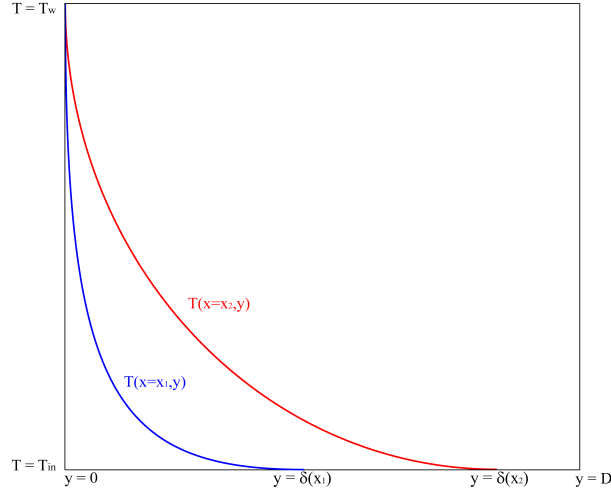


Figure 3.3: graphic representation of the temperature profile at a certain axial position $x = x_1$ and $x = x_2$ with $x_2 > x_1$ within the developing region with a constant wall temperature T_w

From this figure, the first three boundary conditions are easily seen:

$$T(x, y = 0) - T_w = 0 \quad (3.13)$$

$$T(\delta(x)) - T_{in} = 0 \quad (3.14)$$

$$\frac{\partial}{\partial y} T(\delta(x)) = 0 \quad (3.15)$$

The fourth boundary condition can be deduced from the fact that the velocity at the wall is zero. And lastly, at $y = \delta(x)$, the right side of equation (3.11) must be zero, because the temperature gradient with respect to the axial direction equals zero:

$$\frac{\partial^2}{\partial y^2} T(\delta(x)) = 0 \quad (3.16)$$

$$\frac{\partial^2}{\partial y^2} T(0) = 0 \quad (3.17)$$

Using these boundary conditions in conjunction with equation (3.12) gives $A = 1$, $B = -2$, $C = 0$, $D = 2$, $E = -1$. Assuming the flow through the channel is fully developed, the velocity of the fluid can be written as:

$$U = 4U_{max} \left(\frac{y}{d} - \frac{y^2}{d^2} \right) \quad (3.18)$$

In this equation, U_{max} [m/s] is the maximum velocity, which is located at $y = d/2$. Equations (3.18) and (3.12) make the energy equation quite cumbersome and difficult to solve. By assuming that the velocity can be written as a first order Taylor approximation, the differential equation becomes less cumbersome. The result is:

$$U \approx \left(\frac{\partial U}{\partial y} \right)_{y=0} y \quad (3.19)$$

Using equations (3.12) and (3.19) together with (3.11) and assuming that the properties of the fluid are not a function of temperature, results in a differential equation for the boundary layer thickness $\delta(x)$:

$$4\rho U_{max} y \left(\frac{2y}{\delta(x)^2} - \frac{6y^3}{\delta(x)^4} + \frac{4y^4}{\delta(x)^5} \right) \frac{d\delta(x)}{dx} - \lambda d \left(\frac{12y}{\delta(x)^3} - \frac{12y^2}{\delta(x)^4} \right) = 0 \quad (3.20)$$

Since the boundary layer thickness is not a function of y , the equation is integrated with respect to y from 0 to $\delta(x)$. This results in a first order differential equation:

$$\frac{8}{15} \rho U_{max} c_p \delta(x)^2 \frac{d\delta(x)}{dx} = 2\lambda d \quad (3.21)$$

Using the boundary condition that $\delta(0) = 0$ and that $Pe = \frac{\rho c_p u d}{\lambda}$ the boundary layer thickness can be solved for:

$$\frac{\delta(x)}{d} = \frac{1}{2} 90^{\frac{1}{3}} \left(\frac{1}{Pe} \right)^{\frac{1}{3}} \left(\frac{x}{d} \right)^{\frac{1}{3}} \quad (3.22)$$

Suppose that the development length L_{th} is at some axial coordinate where the boundary layer thickness equals a constant c times the height of the channel d^3 . It can then be derived that:

$$\frac{L_{th}}{d} = K_{T_w} Pe \quad (3.23)$$

In which $K = 4/45c^3$. Thus, the development length scales linearly with Pe and d . In Shah and London[47], the development length is defined as the axial coordinate where $Nu(x) = 1.05Nu_\infty$, with Nu_∞ being the Nusselt number for a fully developed boundary layer. For this case, $Nu_\infty = 3.77$ (Todreas[37]). The expression for the Nusselt number is:

$$Nu(x) = \frac{htc(x)d}{\lambda} \quad (3.24)$$

The Nusselt number can thus be considered as a ratio of the heat transfer that is actually happening over the heat transfer due to conductivity. Although equation 3.24 can be analytically written using equations 3.12 and 3.22, $Nu(x) = 1.05Nu_\infty$ is evaluated numerically with Maple 13. The results of this will be presented in chapter 5.

³ cd is chosen here to keep the left side of equation 3.22 dimensionless.

3.3.2 constant heat flux at the wall

For a constant heat flux at the walls of the channel, a new guess needs to be made. This is done in the same manner as before:

$$T - T_{in} = A + B \left(\frac{y}{\delta(x)} \right) + C \left(\frac{y}{\delta(x)} \right)^2 + D \left(\frac{y}{\delta(x)} \right)^3 + E \left(\frac{y}{\delta(x)} \right)^4 \quad (3.25)$$

To solve for the coefficients, again 5 boundary conditions are needed, three of which can be derived from figure 3.4:

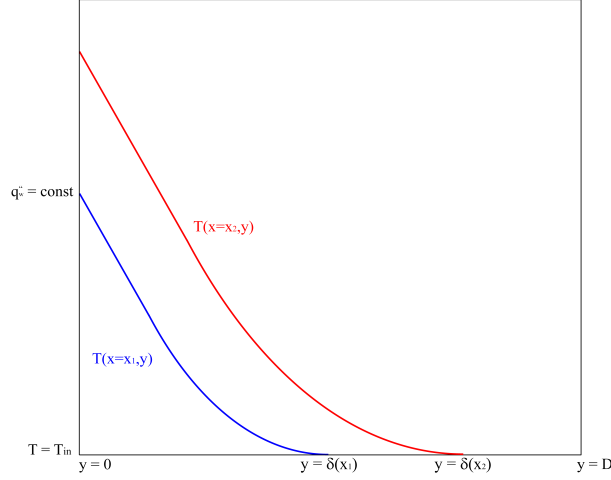


Figure 3.4: graphic representation of the temperature profile at a certain axial position $x = x_1$ and $x = x_2$ with $x_2 > x_1$ within the developing region with a constant heat flux q_w at the wall

$$\frac{\partial}{\partial y} T(0) = -\frac{q_w}{\lambda} \quad (3.26)$$

$$T(\delta(x)) - T_{in} = 0 \quad (3.27)$$

$$\frac{\partial}{\partial y} T(\delta(x)) = 0 \quad (3.28)$$

$$\frac{\partial^2}{\partial y^2} T(\delta(x)) = 0 \quad (3.29)$$

$$\frac{\partial^2}{\partial y^2} T(0) = 0 \quad (3.30)$$

The first boundary condition is derived from Fourier's law. The others are found with the same reasoning as before. This gives for the coefficients that $A = \frac{q_w}{2\lambda} \delta(x)$, $B = -\frac{q_w}{\lambda} \delta(x)$, $C = 0$, $D = \frac{q_w}{\lambda} \delta(x)$, $E = -\frac{q_w}{2\lambda} \delta(x)$, where q_w is the heat flux at the wall. Using the same approximations as before (equations (3.11) (3.19)) and integrating the temperature equation over the boundary layer thickness $\delta(x)$ yields:

$$\frac{2}{5}\rho U_{max} c_p \delta(x)^2 \frac{d\delta(x)}{dx} - d\lambda = 0 \quad (3.31)$$

This results in the following expression for the boundary layer thickness:

$$\frac{\delta(x)}{d} = \frac{1}{2} 60^{\frac{1}{3}} \left(\frac{1}{Pe} \right)^{\frac{1}{3}} \left(\frac{x}{d} \right)^{\frac{1}{3}} \quad (3.32)$$

and for the thermal development length using the same premise as in the previous section:

$$\frac{L_{th}}{d} = K_{q_w} Pe \quad (3.33)$$

In which $K_{q_w} = 2/15c^3$. Thus, the development length scales linearly with Pe and d . For this case, $Nu_\infty = 4.118$.

Chapter 4

Numerical methods

This chapter consists of three main sections. OpenFOAM utilizes a few unique features for solving problems in fluid dynamics, which deviate from other CFD-codes. Two of these are discussed in the first section: the meshes and the pressure-velocity coupling. Secondly the modifications that were made and the implementations that were done in order to solve supercritical fluid flows are discussed. Thirdly, the selected discretization schemes, used boundary conditions, solver methods, a schematic of the whole code and the criteria for convergence are discussed.

4.1 OpenFOAM

4.1.1 meshes

OpenFOAM is a finite-volume solver and thus, it uses the collocated grid arrangement for meshes. However, the code is designed for 3-dimensional problems. As a result, all meshes are 3-dimensional in OpenFOAM. Also, OpenFOAM uses only the cartesian coordinate system. In order to solve 2-dimensional problems, like channel flow, or axisymmetric flow in a cylindrical geometry, OpenFOAM uses special mesh-related boundary conditions and wedge geometries. A 3d mesh is made with only 1 cell in the direction that should not be solved for. An example is shown in figure 4.1.

In this example, there is only 1 cell in the z -direction. For an OpenFOAM case to run, boundary conditions need to be specified on all patches (mesh boundaries) for each variable. OpenFOAM recognizes the case as 2-dimensional if, for each variable, the boundary condition at the front and back planes is set to 'empty'. In the example, the two planes lying in the x,y plane are the front and back. As a result, OpenFOAM will only solve in the x and y direction. For axisymmetric cylindrical or annular based problems, a similar method is used. In this case, a wedge geometry is used, with only 1 cell in the direction of the angular coordinate θ . This is displayed in figure 4.2.

In the examples displayed in figure 4.2, the OpenFOAM meshes have one cell in the x -direction. Because of this, the walls are not curved. This means, in order to properly simulate a cylinder or annulus, the angle θ has to be chosen to be

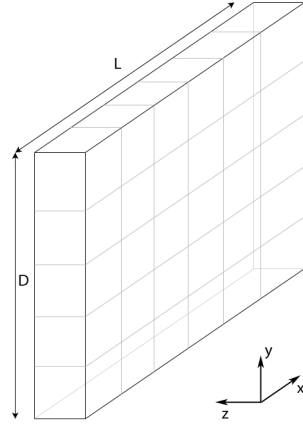


Figure 4.1: Channel geometry in OpenFOAM. The channel height and length in the y and x direction respectively are shown.

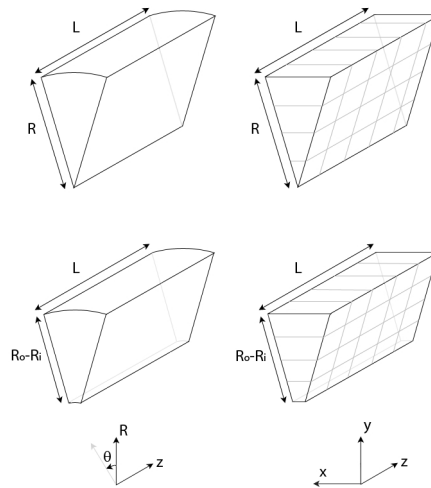


Figure 4.2: Axisymmetric cylindrical and annular geometries. On the left side, a wedge from a cylinder and an annulus is displayed. On the right, the corresponding meshes in OpenFOAM are displayed.

very small¹. For the planes which have a normal pointing in the θ direction, a special boundary condition called ‘wedge’ is used. This acts basically as a zero-gradient boundary condition². [30]

4.1.2 pressure-velocity coupling with buoyancy effects

The OpenFOAM standard buoyancy solvers do not solve for the total pressure p , but for $p_{rgh} = p - \rho g \cdot \vec{x}$ instead. This means that the pressure equation

¹The OpenFOAM user guide suggests that the angle should be less than 5° .

²OpenFOAM will solve for the velocity component in the x-direction. However, the calculated values are very small (typically of order $1 \cdot 10^{-20}$).

that is solved in OpenFOAM, is different from well known formulations (see for example [17], [27]). The momentum equation can be written in discretized form³ as follows:

$$A\vec{U} = H - \nabla p + \rho\vec{g} \quad (4.1)$$

where A and H are discretization operators, of which the elements depend on convection and diffusive terms and their respective discretization scheme. Using the following identity: $\nabla p - \rho\vec{g} = \nabla(p - \rho\vec{g} \cdot \vec{x}) + \vec{g} \cdot \vec{x}\nabla\rho$, the expression for \vec{U} becomes:

$$\vec{U} = \frac{H}{A} - \frac{\nabla p_{rgh}}{A} - \frac{\vec{g} \cdot \vec{x}\nabla\rho}{A} \quad (4.2)$$

Equation 4.1 can be solved implicitly for \vec{U} while using the values for p of the previous iteration. The resulting vector \vec{U} is called the momentum predictor U^* . However, this does not satisfy the continuity equation. Multiplying equation 4.2 by ρ and taking the divergence of the result gives:

$$\nabla \cdot \underbrace{\left(\frac{\rho}{A}H\right)}_{\vec{\phi}} - \nabla \cdot \underbrace{\left(\frac{\rho}{A}\vec{g} \cdot \vec{x}\nabla\rho\right)}_{\vec{\phi}_{buoyancy}} = \nabla \cdot \left(\frac{\rho}{A}\nabla p_{rgh}\right) \quad (4.3)$$

The terms on the left side of the equation (called $\vec{\phi}$ and $\vec{\phi}_{buoyancy}$ respectively in OpenFOAM⁴.) are evaluated explicitly on the cell faces, whereas the term on the right-hand side is evaluated implicitly (in other words p_{rgh} is solved for). With these last definitions, the total equation for p_{rgh} becomes:

$$\nabla \cdot \left(\frac{\rho}{A}\nabla p_{rgh}\right) = \nabla \cdot (\vec{\phi} - \vec{\phi}_{buoyancy}) \quad (4.4)$$

After solving the pressure equation, the velocities are updated as follows:

$$U = U^* - \frac{1}{A}(\nabla p_{rgh} + \vec{g} \cdot \vec{x}\nabla\rho) \quad (4.5)$$

Because the continuity equation was used in the derivation for the pressure equation, the updated velocities obey continuity. Finally, the total pressure is explicitly calculated as:

$$p = p_{rgh} + \rho\vec{g} \cdot \vec{x} \quad (4.6)$$

The total pressure-velocity coupling can be summarized as follows:

- at each iteration step,
- 1) the momentum equation is solved, based on the old pressure field,
 - 2) ϕ and $\phi_{buoyancy}$ are explicitly calculated,
 - 3) the pressure equation 4.4 is implicitly solved,
 - 4) velocities at all cells and boundaries are updated with equation 4.5
 - 5) and the total pressure is explicitly calculated using equation 4.6.

³The discretized system has been written as a matrix system. This way, it is easily recognized in the OpenFOAM code

⁴ $\vec{\phi}$ and $\vec{\phi}_{buoyancy}$ are help variables.

Because p_{rgh} is solved for and not p , a special boundary condition is used, which is called buoyantPressure in OpenFOAM. It is calculated as follows:

$$\vec{n} \cdot \nabla p_{rgh} = -\vec{n} \cdot \nabla \rho(\vec{g} \cdot \vec{x}) \quad (4.7)$$

For a wall, which has a normal vector \vec{n} perpendicular to the gravity vector \vec{g} and with the definition of p_{rgh} , 4.7 is equivalent to:

$$\vec{n} \cdot \nabla p = 0 \quad (4.8)$$

This boundary condition is due to the zero-velocity boundary condition at the walls. For an inlet or outlet which has a normal vector opposite to the gravity vector, 4.7 is equivalent to:

$$\vec{n} \cdot \nabla p = \vec{n} \cdot \rho \vec{g} \quad (4.9)$$

This equation is known as the hydrostatic equation. [29], [24]

4.2 Code implementations

4.2.1 Equations

In order to solve supercritical fluid flows, three variables must be solved for: velocity \vec{U} , specific enthalpy h and pressure p_{rgh} . The momentum and energy equation were slightly altered to this end; in OpenFOAM, the equations contain effective viscosity and diffusivity terms, which are not needed in laminar simulations. Also, the equations in OpenFOAM are not suited for variable specific heat capacity and heat conductivity. The corresponding equations in the code are the momentum equation,

$$\nabla \cdot \rho \vec{U} \vec{U} = \nabla \cdot \vec{\tau} - \nabla p + \rho \vec{g} \quad (4.10)$$

where $\vec{\tau}$ is defined as:

$$\vec{\tau} = \mu \left((\nabla \vec{U}) + (\nabla \vec{U})^T - \frac{2}{3} (\nabla \cdot \vec{U}) I \right) \quad (4.11)$$

and the heat equation,

$$\nabla \cdot (\rho U h) = \nabla \cdot \left(\frac{\lambda}{c_p} \nabla h \right) \quad (4.12)$$

The work terms in equation 3.5 have been neglected here (see chapter 3), because the order of magnitude is much smaller than the convective and diffusive term. This was verified with preliminary simulations.

4.2.2 Implemented boundary conditions

The OpenFOAM package does not come standard with boundary conditions for fully developed flow. In order to simulate fully developed flow, the following boundary conditions were added for 2d-channels, pipes and concentric annuli respectively:

$$U(y) = 6U_m \left(\frac{y}{d} - \frac{y^2}{d^2} \right) \quad (4.13)$$

$$U(y) = 2U_m \left(1 - \frac{y^2}{d^2} \right) \quad (4.14)$$

$$U(y) = 2U_m \left(\frac{1 - \left((1 - \chi) \left(\frac{y - R_i}{R_o - R_i} \right) + \chi \right)^2 + \frac{\chi^2 - 1}{\ln(\chi)} \ln \left((1 - \chi) \left(\frac{y - R_i}{R_o - R_i} \right) + \chi \right)}{1 + \chi^2 - \frac{\chi^2 - 1}{\ln(\chi)}} \right) \quad (4.15)$$

In these equations U_m is the mean entrance velocity (m/s), d the hydraulic diameter (m), R_i and R_o the inner and outer radius of a concentric annulus (m) and χ is defined as $\chi = R_i/R_o$. The coordinate system shown in figures 4.1 and 4.2 was used. In the last two equations, the radial coordinate r was replaced by y (Weigand[54], Deen[9]). This is correct, if the inlet of the tube or annulus is located at $x=0$. Equations 4.13, 4.14 and 4.15 are imposed at the inlet.

In Todreas[37] a relation between enthalpy and pressure is given: $dh = c_p dT + (1 - \beta T) \frac{dp}{\rho}$. This leads to:

$$\nabla h = c_p \nabla T + \frac{1 - \beta T}{\rho} \nabla p \quad (4.16)$$

At the wall $\vec{n} \cdot \nabla p = 0$. For a heat flux q_w'' at the wall, Fourier's law of conduction reads:

$$q_w'' = -\lambda \vec{n} \cdot \nabla T. \quad (4.17)$$

This leads to:

$$\vec{n} \cdot \left(\frac{\lambda}{c_p} \right) \nabla h = q_w'' \quad (4.18)$$

In order to properly calculate this boundary condition, the face-values of c_p and λ at the boundary are used.

Another boundary condition for the energy equation was implemented. At the outlet, the enthalpy profile is unknown before starting the simulation. If fluid properties are a function of enthalpy, the same applies for the gradient at the outlet⁵. Therefore, a new boundary condition is used; the gradient-value (in the direction of the main flow direction) of the before last cell to the outlet is used as a boundary value.

$$\vec{n} \cdot \nabla h|_{(f_{outlet,j})} = \vec{n} \cdot \nabla h|_{(V_{n-1,j})} \quad (4.19)$$

In this equation, \vec{n} is the normal vector of the outlet, f represents a face value at the outlet, j represents the coordinate orthogonal to the normal of the outlet, n is the last cell with respect to the axial direction and $V_{n-1,j}$ is the volumetric value of the enthalpy gradient of the before last cell to the outlet⁶. Equation 4.19 is graphically represented in figure 4.3.

⁵with constant properties, the gradient can be calculated using analytical methods if the length of the geometry is greater than the development length

⁶There is no real physical meaning to this equation. It is merely a numerical approximation.

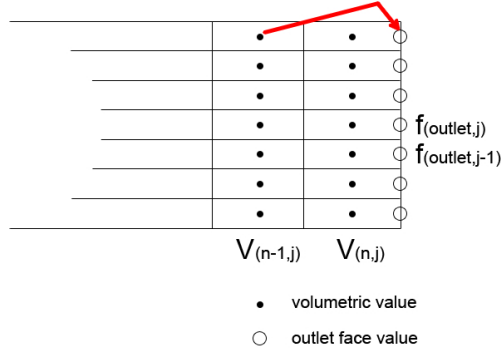


Figure 4.3: Graphic representation of equation 4.19.

4.2.3 supercritical fluid properties

As was mentioned in chapter 3, supercritical fluid properties change sharply as the enthalpy increases, especially near the pseudo-critical point. This behaviour is modelled with splines (set of algebraic functions $f_i(x)$, each of which is valid for a certain range of variable x):

$$\psi_i(h) = \psi_{a,i}(h - h_i)^3 + \psi_{b,i}(h - h_i)^2 + \psi_{c,i}(h - h_i) + \psi_{d,i} \quad \text{if } h_i < h < h_{i+1} \quad (4.20)$$

In this equation ψ stands for a fluid property (ρ , c_p , λ , μ) or temperature T . ψ_i is a function of enthalpy h and it is valid for $h_i < h < h_{i+1}$. $\psi_{(abcd),i}$ are constants unique for each property and particular enthalpy range. The splines were made with no less than forty data points from the NIST-database [51], over a temperature range of 10-150 °C for CO₂, 1-1550 °C for water at 23 MPa and 1-500 °C for water at 25 MPa. More data points were chosen around the pseudo-critical point than elsewhere. This is shown in figure 4.4 for c_p . The splines were tested over the same temperature range on intervals of 0.1 K. The results are summarized in tables 4.1, 4.2 and 4.3.

Table 4.1: CO₂ spline test results. The maximum, minimum and average error (equation 4.21) for all fluid properties (in percentages), as well as the difference in temperature (K) are given.

	ρ	μ	c_p	λ	$\Delta T(K)$
max(e)	0.021	0.34	0.17	0.00092	0.013
min(e)	$2.3 \cdot 10^{-8}$	$5.9 \cdot 10^{-9}$	$8.2 \cdot 10^{-8}$	$5.0 \cdot 10^{-11}$	$5.6 \cdot 10^{-8}$
\bar{e}	0.0019	0.0067	0.0084	$4.1 \cdot 10^{-5}$	0.00036

The error in the tables is defined as:

$$e = \frac{\psi_{spline} - \psi_{NIST}}{\psi_{NIST}} * 100 \quad (4.21)$$

in which ψ_{NIST} is a property from the NIST-database (see [51]) and ψ_{spline} the same property calculated according to equation 4.20. It can be clearly seen

Table 4.2: Spline test results for water at 23 MPa. The maximum, minimum and average error (equation 4.21) for all fluid properties (in percentages), as well as the difference in temperature (K) are given.

	ρ (%)	μ (%)	c_p (%)	λ (%)	$\Delta T(K)$
$\max(e)$	0.034	0.022	0.24	0.059	0.046
$\min(e)$	$6.5 \cdot 10^{-8}$	$3.1 \cdot 10^{-9}$	$1.2 \cdot 10^{-8}$	$1.1 \cdot 10^{-11}$	$3.3 \cdot 10^{-8}$
\bar{e}	0.0083	0.0054	0.056	0.017	0.0040

Table 4.3: Spline test results for water at 25 MPa. The maximum, minimum and average error (equation 4.21) for all fluid properties (in percentages), as well as the difference in temperature (K) are given.

	ρ (%)	μ (%)	c_p (%)	λ (%)	$\Delta T(K)$
$\max(e)$	0.011	0.74	1.4	0.43	1
$\min(e)$	$4.0 \cdot 10^{-8}$	0	$4.2 \cdot 10^{-6}$	$2.2 \cdot 10^{-7}$	0
\bar{e}	0.0019	0.040	0.039	0.0054	0.38

that the maximum error in a property is lower than 1% for CO_2 and water at 23 MPa. The differences in water at 25 MPa are slightly larger. Only c_p has a maximum error of over 1%. On average, the error in fluid properties is lower than 0.1% in all supercritical fluids and the temperature difference is less than 0.4 K. The splines were implemented in OpenFOAM as a single function with the help of boolean functions.

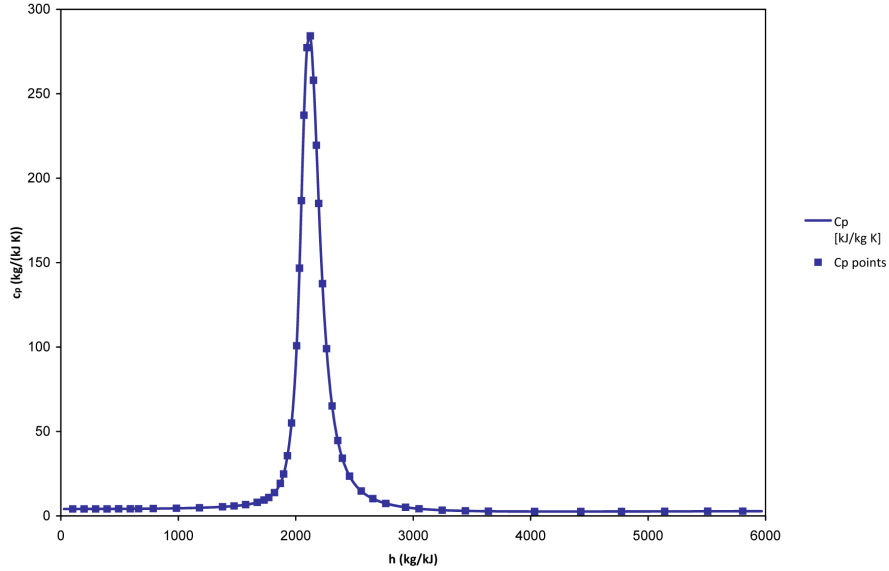


Figure 4.4: c_p as a function of enthalpy. Shown are the spline, as well as the chosen points used to create the spline.

4.2.4 post-processing

Two typical non-dimensional numbers that are often encountered in fluid dynamics and heat transfer depend on calculated field data: the Nusselt-number Nu and the friction factor f . Because of this, they are best calculated within the OpenFOAM code. This was implemented in the code after the main iteration loop (see section 4.3.5). The Nusselt number is defined as:

$$Nu = \frac{q_w^* D}{\lambda(T_w - T_b)} \quad (4.22)$$

in which T_b is defined as

$$T_b = \frac{\int \rho U c_p T dA}{\int \rho U c_p dA} \quad (4.23)$$

and the friction factor is defined as:

$$f = \frac{\tau_w}{\frac{1}{2}\rho\overline{U^2}} \quad (4.24)$$

where

$$\overline{\rho U^2} = \frac{\int \rho U^2 dA}{\int dA} \quad (4.25)$$

In these equations, U_{axial} is the main flow direction, T_w the wall temperature and τ_w the shear stress at the wall. The integrals were evaluated as a sum.

4.3 Code overview

4.3.1 boundary conditions overview

All geometries considered in this work are either 2d-channels, pipes or annuli. Each geometry has a wall (or walls), an inlet and an outlet. The boundary conditions for \vec{U} , h , and p are displayed in table 4.4.

Table 4.4: Boundary conditions used. h_{in} , h_w and U_{in} represent constants.

	walls	inlet	outlet
\vec{U}	$\vec{0}$	U_{in} or Eq. 4.13 4.14 or 4.15	$\vec{n} \cdot \nabla \vec{U} = 0$
h	h_w , Eq. 4.18 or $\vec{n} \cdot \nabla h = 0$	h_{in}	Eq. 4.19
p	$\vec{n} \cdot \nabla p = 0$	$\vec{n} \cdot \nabla p = \vec{n} \cdot \rho \vec{g}$	$\vec{n} \cdot \nabla p = \vec{n} \cdot \rho \vec{g}$

4.3.2 discretization schemes

Each term in the equations is discretized with either a central differencing (CD) or first order upwind differencing (UD) scheme. This is summarized in table 4.5.

For all terms except the convective terms, the central differencing scheme is used. The main advantage of central differencing is that fewer cells are needed for a good solution, compared to the upwind differencing scheme. However

Table 4.5: Differencing schemes used in the momentum, enthalpy and pressure equation.

term	scheme	implicit/explicit
$\nabla \cdot (\rho \vec{U} \vec{U})$	UD	implicit
$\nabla \cdot (\rho \vec{U} h)$	UD	implicit
$\nabla \cdot \mu \nabla \vec{U}$	CD	implicit
$\nabla \cdot \left(\frac{\lambda}{c_p} \nabla h \right)$	CD	implicit
$\nabla \cdot \left(\frac{\rho}{A} \nabla p_{rgh} \right)$	CD	implicit
all other terms	CD	explicit

for problems in which the convective part is dominant, the central differencing scheme shows peaking behaviour. This means that a cell value of a variable is interpolated to be higher or lower than the face values of the same cell. It was found in preliminary simulations that this leads to unphysical results. To avoid this behaviour, the upwind differencing scheme is used for the convective part of the equations. The disadvantage of this scheme is numerical diffusion. This effect diminishes for large number of cells. Therefore, it is imperative to investigate the sensitivity of a solution with respect to the number of cells⁷.

4.3.3 solvers and preconditioners

The total system of (linear) equations is solved using various methods and preconditioners as is shown in table 4.6:

Table 4.6: Selected solvers and preconditioners. The abbreviations stand for bi-conjugate gradient (BiCG), conjugate gradient (CG), geometric algebraic mult-grid (GAMG), diagonal incomplete LU and diagonal incomplete Cholesky (DIC).

variable	solver	preconditioner
U	BiCG	DILU
h	BiCG	DILU
p_{rgh}	CG/GAMG	DIC/GAMG

All of the selected solvers and preconditioners (with the exception of GAMG) are used as a standard within OpenFOAM tutorial cases: BiCG (DILU) for asymmetric matrices (for variables U and h) and PCG (DIC) for symmetric matrices (variable p_{rgh}). It was found that for cases with variable density selecting GAMG for p_{rgh} lead to faster convergence.

4.3.4 Relaxation factors

In order to ensure numerical stability, relaxation factors are used for the variables U , h and p_{rgh} . For constant property and mixed convection cases, these were 0.7, 0.9 and 0.3 respectively. For supercritical fluid cases, these were set to 0.4, 0.5 and 0.3 respectively.

⁷Results of mesh sensitivity analysis are described in the next chapter.

4.3.5 code schematic

A schematic of the code is displayed in figure 4.5. It is divided in three parts: initialization, processing and finalization. Before the code is run, schemes, solvers, most boundary conditions, fields and the number of iterations are set in various dictionaries (this is called pre-processing). After the code is started, time controls (number of iterations, step size), the mesh, variable fields and boundary conditions are read. The result is that specified variables, like velocity and temperature are ‘tied’ to a certain position on the mesh. Because the boundary conditions described in section 4.2.2 cannot be defined easily in the pre-processing stage, the following parameters were put into a dictionary: D , R_o , R_i , U_m and q_w^v . These are used to set any of the boundary conditions in the afore-mentioned section (equations 4.13, 4.14, 4.15, 4.18 and 4.19). All fluid properties, as well as temperature are then calculated at each mesh cell and cell-face. The main processing part consists of a *for loop*, in which the momentum, enthalpy and pressure equation are solved. After the enthalpy equation is solved, the outlet boundary condition for enthalpy is updated according to equation 4.19. The fluid properties, as well as the temperature are then calculated with equation 4.20. The pressure equation is solved within a second loop for n -times. These extra evaluations of the pressure solution are known as non-orthogonal correctors. n was set to 2 or 3 in all pipe or annulus cases. This way, the continuity equation is better satisfied. After the corrector loop has finished, the total pressure is calculated by 4.6. If the current iteration number of the primary loop has reached a pre-defined value, the loop ends and the Nusselt number and the friction factor are calculated.

4.3.6 convergence criteria

At each iteration step, OpenFOAM lists the initial residual and final residual of each variable (the residual of course being a result of the chosen solver algorithms described earlier). A solver algorithm stops if the current residual falls below 0.1% of the initial one. If the initial residual of each variable drops with each iteration step, the solution converges. Because it is difficult to tell what a good threshold is for the initial residual in order to call the solution fully converged, so called monitors are used. A monitor is simply a certain value of a variable at a point in the field. The following monitors and criteria have been used in order to call the solution fully converged:

- 1) the average of $\nabla \cdot (\rho \vec{U})$ is of order 10^{-6}
- 2) change in temperature values at the outlet for 1000 iterations < 0.01 K
- 3) $\vec{n} \cdot \nabla h$ at the outlet is constant.

The first criterion certifies that the continuity equations is satisfied. The second criterion is used, because T -values are often presented in the results. $\vec{n} \cdot \nabla h$ was chosen as a criterion to see if equation 4.19 works. The second and third criterion show that the solution with respect to specific enthalpy has converged to a satisfactory solution.

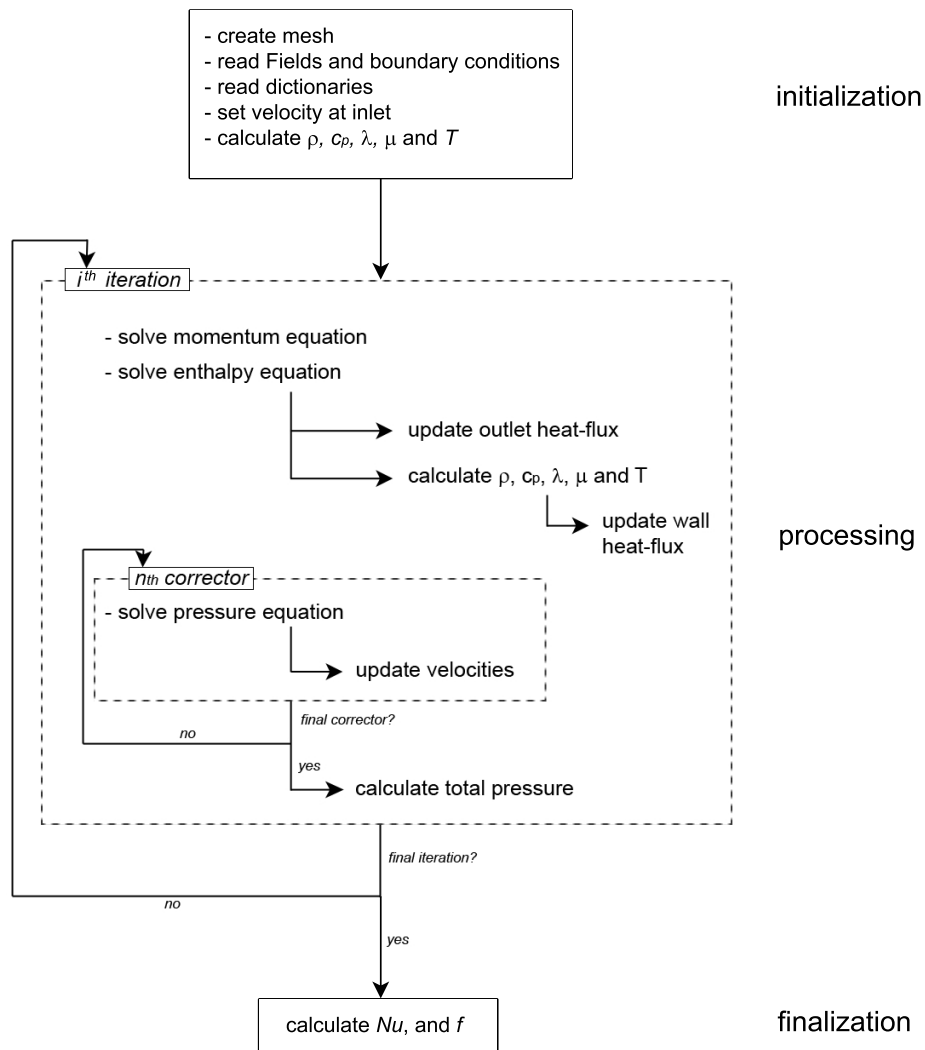


Figure 4.5: Schematic overview of the code. The code is divided into three parts: initialization, processing and finalization.

Chapter 5

Numerical Assessment

The code developed using OpenFoam as a base code (as described in chapter 4) has been validated in three different stages: a) constant property cases, b) a simple mixed convection case and c) supercritical fluid cases. Numerical, experimental as well as analytical results from other authors have been used for validation. Any deviations are reported (in percentages) to give a quantitative view on the validation. Each section starts with a description of the case used for validation. Mesh grading analyses are presented for the non-constant property cases. The results are presented thereafter. At the end of the chapter, the performance of the OpenFOAM code is discussed.

5.1 Constant property cases

5.1.1 Graetz-Nusselt problem in a channel geometry

In chapter 3, it was derived that $L_{th}/(Pe.d) = K$. L_{th} is located at the axial coordinate where $Nu=1.05Nu_{\infty}$ (Shah and London[47]). To check the theory that was derived there and to check the OpenFoam code, a channel with $d = 0.01$ m and $L = 0.2$ m is considered. A fluid enters the channel at $T_{in}=293$ K. The walls have a constant temperature of $T_w = 303K$. The properties of the fluid were chosen to be: $\rho = 1000$ kg/m³, $c_p = 4183$ kJ/kg, $\lambda = 0.68$ w/mK and $\mu = 0.001$ kg/m.s. The case is graphically represented in figure 3.2.

The Nusselt number, as defined by equation 3.24 in chapter 3 and the numerical results from the OpenFOAM code are plotted in figure 5.1, together with a relation from Shah[47]¹:

$$Nu = \begin{cases} \frac{1}{2}((1.233(x^*)^{(-1/3)} + 0.4) & x^* \leq 0.001 \\ \frac{1}{2}((7.541 + 6.874(10^3 x^*)^{(-0.488x^*)})e^{-245x^*}) & x^* > 0.001 \end{cases} \quad (5.1)$$

K_{T_w} was evaluated by Maple 13 and was calculated to be 0.035706. Shah [47] has calculated this to be 0.031894. The error is 12%, which is significant. In

¹The relations from Shah are divided by 2, because the relations given there are valid for flate-plate channels. A 2d-channel is considered here. The hydraulic diameter for those geometries are $2d$ and d , respectively. The constants K_{T_w} and K_{q_w} were recalculated because of this as well.

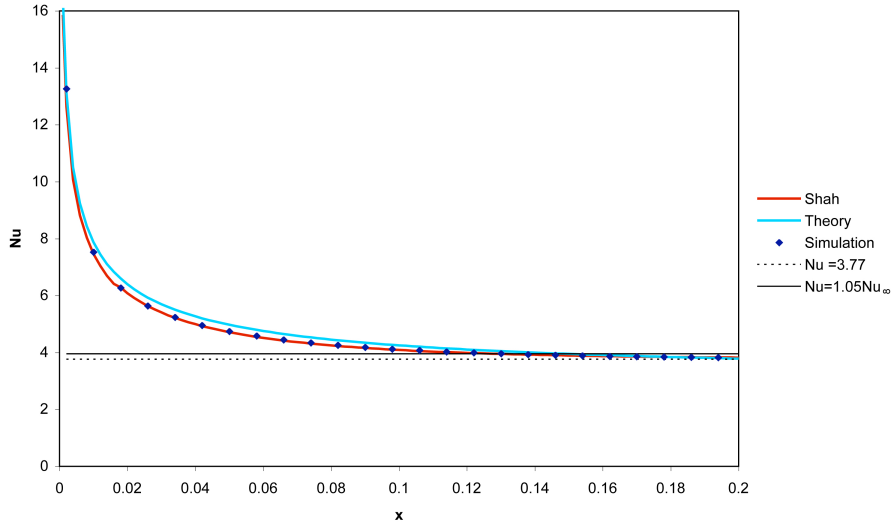


Figure 5.1: Nusselt number as a function of axial position with constant wall temperature. Shown are the relations from Shah, integral approximation method and the results of the simulation.

figure 5.1, it can be seen that the Nusselt number, calculated with the integral approximation method (see chapter 3), is overpredicted compared to those of Shah. After $x > 0.16$, the error between the two theories is less than 1%. However, after $x > 0.10$, Nu changes very slowly, which causes the large difference in K_{T_w} . The numerical results from the OpenFOAM code are in good agreement with the relation from Shah: for $x > 0.018$ the error is smaller than 1%. The biggest error (first point shown in figure) is 5%.

The same case as before was considered, but with a constant wall heat flux $q_w^* = 10^4$ W/m². The integral approximation method, a relation by Shah (see below) and the numerical results from OpenFOAM are presented in figure 5.2. The relation by Shah[47] reads:

$$Nu = \begin{cases} \frac{1}{2}(1.490(x^*)^{(-1/3)}) & x^* \leq 0.0002 \\ \frac{1}{2}(1.490(x^*)^{(-1/3)} - 0.4) & 0.0002 < x^* \leq 0.001 \\ \frac{1}{2}(8.235 + 8.68(10^3 x^*)^{(-0.506 x^*)} e^{-164 x^*}) & x^* > 0.001 \end{cases} \quad (5.2)$$

$K_{q_w^*}$ was evaluated with Maple 13 to be 0.0452273. According to Shah this is 0.0461756. Thus, $K_{q_w^*}$ is off by 2.1%. Compared to the constant wall temperature case above, the results for Nu from the theory are in much better agreement with equation 5.2. For $x > 0.14$ the error between them is less than 1%. The numerical results are in good agreement with equation 5.2. The biggest error is 3.5%. For $x > 0.014$ the error is smaller than 1%.

From these results, it can be concluded that the integral approximation method, as described in chapter 3, yields moderate to good results, for constant wall temperature and uniform wall heat flux boundary conditions respectively. The OpenFoam code yields excellent results for constant property cases for the Graetz-Nusselt problem in channels.

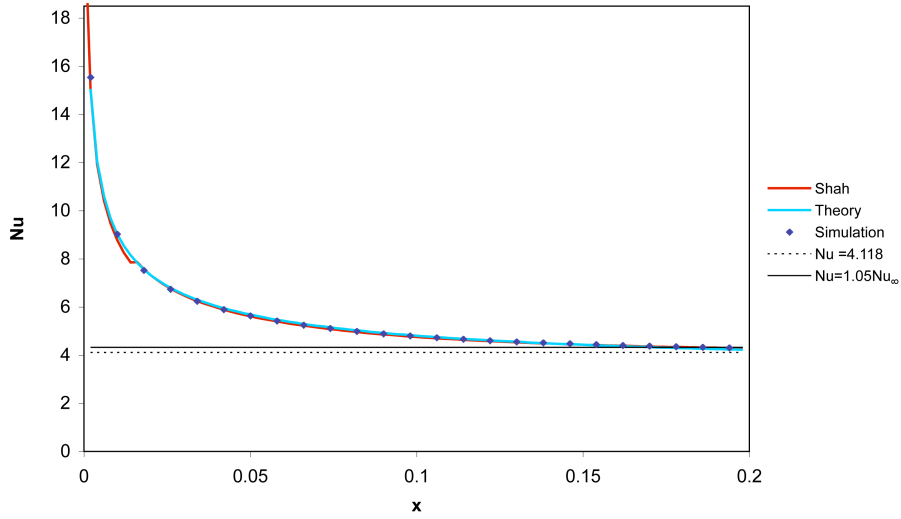


Figure 5.2: Nusselt number as a function of axial position with constant wall heat flux. Shown are the relations from Shah, the integral approximation method and the results of the simulation.

5.1.2 Graetz-Nusselt problem in an annular geometry

As was explained in the previous chapter in section 4.1.1, cylindrical problems are modelled using wedge geometries (see chapter 4). To test this, the OpenFOAM code and a wedge geometry were tested with two cases from Weigand et al.[54]. In this paper, an analytical solution is derived for the Graetz-Nusselt problem in an annular geometry with two different sets of boundary conditions. The eigenvalues and eigenvectors of the solution were numerically evaluated. The outer diameter $2R_o$ of the annulus is twice the size of the inner diameter $2R_i$. The hydraulic diameter $D_h = 2(R_o - R_i)$. Two cases from Weigand et al.[54] were used for validation. These are graphically represented in figure 5.3.

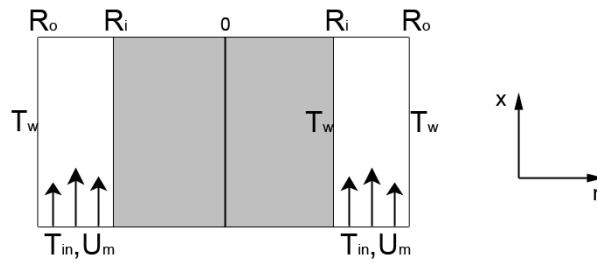


Figure 5.3: Graphical representation of the cases selected from Wiegand et al.[54].

In the first case, both the inner wall and the outer wall are kept at a constant temperature T_w , with an inlet temperature of T_{in} , with $Pe=300$. In figure 5.4, the temperature profiles for different axial coordinates are plotted. The results

from the OpenFOAM code and Weigand et al.[54] are in excellent agreement. Note that the maximum of a temperature profile is not located at $\frac{r-R_i}{R_o-R_i}=0.5$ but at 0.47. In figure 5.5, the Nusselt number is plotted as a function of axial length. The Nusselt number calculated from the OpenFOAM results are in excellent agreement with the results from [54] (error is less than 1% everywhere).

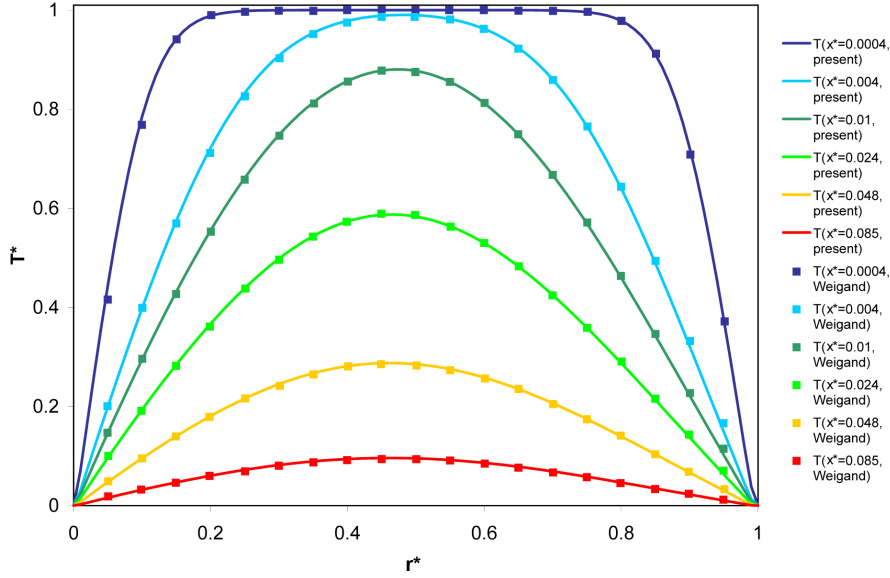


Figure 5.4: Temperature profiles at different axial positions of the annular case. Results are plotted from Weigand et al. [54] and OpenFoam code. $T^* = \frac{T-T_w}{T_i-T_w}$ and $r^* = \frac{r-R_i}{R_o-R_i}$.

In the second case, the inner wall is assumed to be adiabatic, whereas the outer wall is kept at a constant wall temperature, with $Pe=50$. Figure 5.6 shows the comparison of the Nusselt number along the axis between the present study and [54]. The Nusselt numbers are slightly overpredicted (less than 3%). It must be noted here that the data from Weigand et al. [54] was difficult to digitize, because the data was plotted in a log-plot with less than optimal resolution. From the results for the Graetz-Nusselt problem in an annular geometry, it can be concluded that using a wedge geometry with a cartesian coordinate system can be used to solve radial heat transfer problems with excellent results.

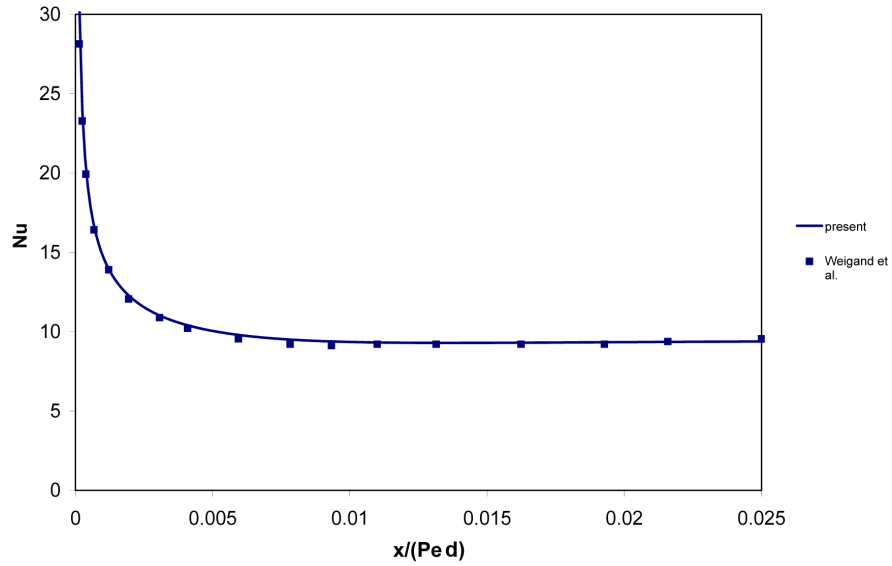


Figure 5.5: Nusselt number as a function of axial position for $Pe = 300$. Results are plotted from Weigand et al. [54] and OpenFoam code. For the calculation of the Nusselt number, the wall temperature at the inner wall is used.

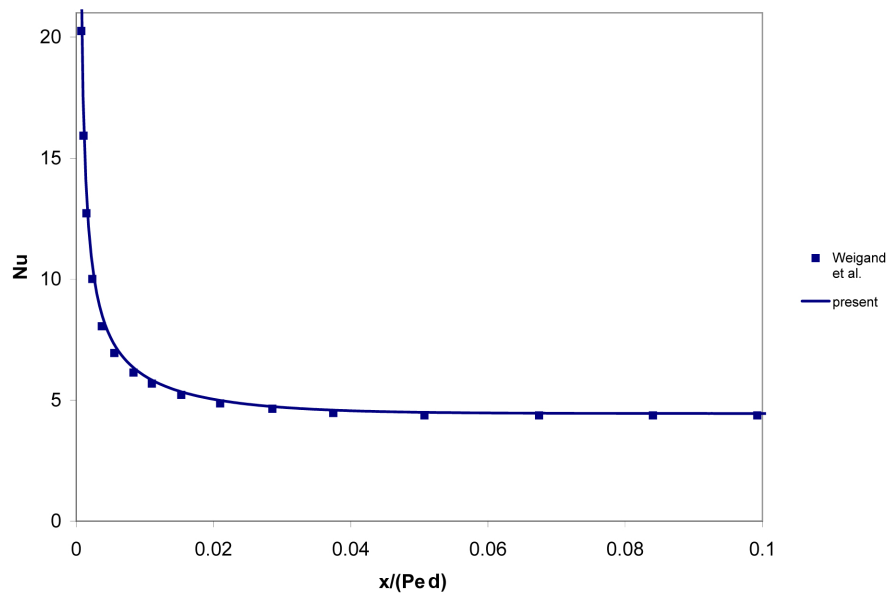


Figure 5.6: Nusselt number as a function of axial position for $Pe = 50$. Results are plotted from Weigand et al. [54] and OpenFoam code. For the calculation of the Nusselt number, the wall temperature at the outer wall is used.

5.2 Mixed convection of air

5.2.1 Mixed convection of air in a flat-plate channel geometry

As was noted in the literature survey, Desrayaud and Lauriat[10] successfully studied the occurrence of flow reversal in buoyancy aided forced convection. To show that the OpenFOAM code simulates mixed convection well, one case from [10] was used for validation. For the model, a vertical flat-plate channel geometry was considered with a diameter of 0.03 m, and an axial length of 1.50 m. The mesh consists of 60 cells and 300 cells in the y and x directions respectively. The working fluid is air, modelled by the Boussinesq approximation. All dimensionless numbers reported in the paper were evaluated at 35 °C. The wall temperature T_w is 60 °C and that of the inlet T_{in} is 10 °C. The average inlet velocity (fully developed profile, see equation 4.13) is 0.0822 m/s. The outlet boundary conditions for U and T are set to zerogradient². Results of the mesh grading study can be found in table 5.1. The case is graphically represented in figure 5.7.

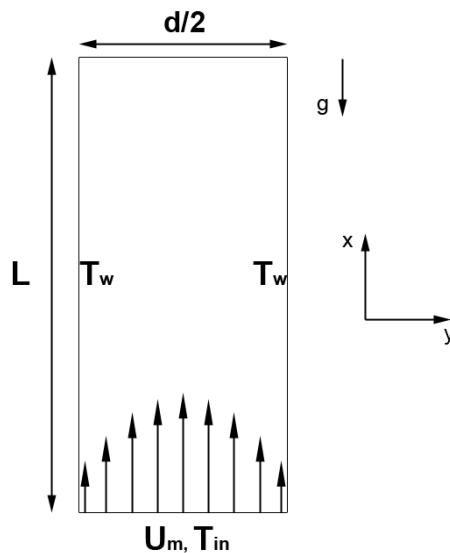


Figure 5.7: Graphical representation of the case selected from Desrayaud and Lauriat.[10].

Plots of velocity, temperature and the Nusselt number can be found in figures 5.8, 5.9 and 5.10.

Figure 5.8 shows the velocity profile at different locations along the dimensionless axial coordinate (defined here as $x^* = x/d$) of the channel. The figure shows that there is excellent agreement between the results from Desrayaud and Lauriat and the present study.

²This is strictly speaking not true. However, zerogradient at the outlet for the temperature equation is a good approximation, because $Pe = 212$. For $Pe \gg 1$, axial conduction can be neglected (Deen[9]). Secondly, for $L \gg D$, the temperature differences are very small.

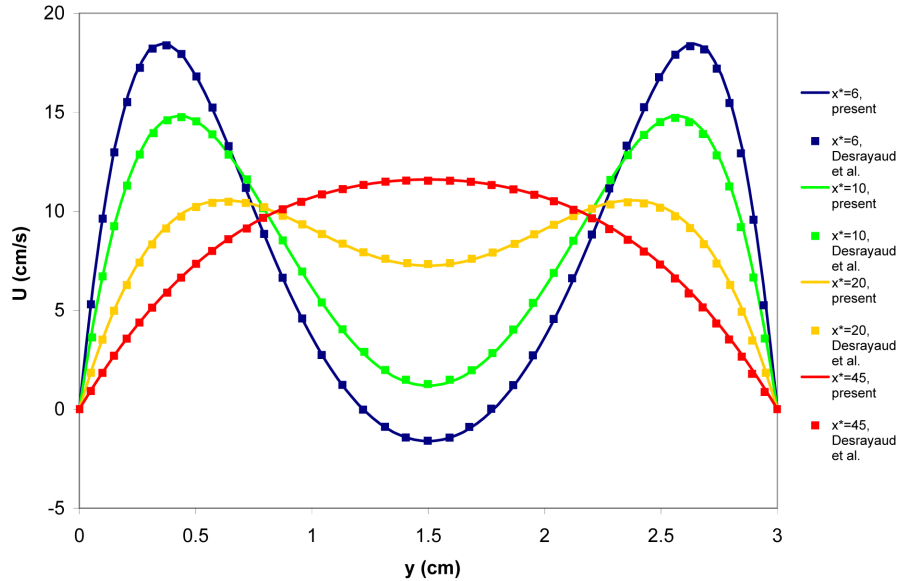


Figure 5.8: Velocity profiles at different locations along the axis of the mixed convection case. Results are plotted from Desrayaud and Lauriat[10] and OpenFoam code.

Figure 5.9 shows the temperature profile at the same axial positions as in figure 5.8. The figure shows that there is good agreement between the present simulation and that of Desrayaud and Lauriat[10] for $x^* > 6$. At $x^* = 6$ the temperature profile of the present study is underpredicted by 0.5 K. This might be due to differences between the two studies in choice of discretization schemes. In Desrayaud and Lauriat[10], no information was given with respect to the discretization schemes. No notable differences in the temperature at $x^* = 6$ with respect to the mesh sensitivity analysis (table 5.1) are seen. Thus, numerical diffusion and spiking due to 1st order upwind and central differencing respectively cannot be the cause. Although the temperature is slightly different at $x^* = 6$, the velocity profiles from Desrayaud and Lauriat[10] and the present study match very well. This is because the density difference caused by a temperature difference of 0.6K (using the Boussinesq approximation for air) is only 0.2%.

Table 5.1: Mesh sensitivity results for the mixed convection case. Displayed are the number of cells in the y and x directions as well as the temperature and the velocity at the center line at $x^* = 6$ ($T(x_6^*, 0.5D)$, $U_{max}(x_6, y)$), and the pressure drop (Δp).

N_y, N_x	$T(x_6^*, 0.5D)$	$U_{max}(x_6, y)$	Δp
300,60	33.419	0.1853	-12.742
600,120	33.415	0.1859	-12.751

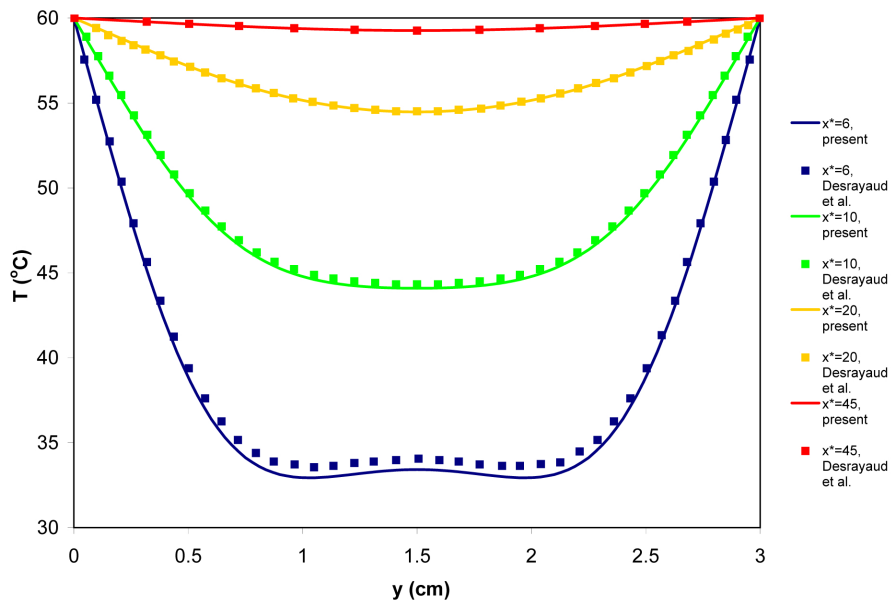


Figure 5.9: Temperature profiles at different locations along the axis of the mixed convection case. Results are plotted from Desrayaud and Lauriat and OpenFoam code.

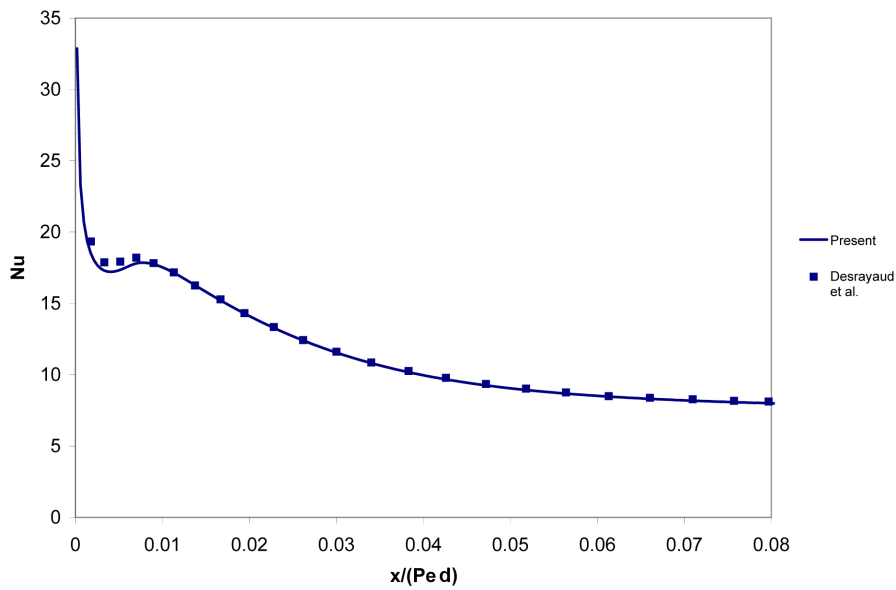


Figure 5.10: Nusselt number along the axial coordinate. Results are plotted from Desrayaud and Lauriat and OpenFoam code.

The Nusselt number is plotted in figure 5.10 as a function of axial length. The local increase in the Nusselt number is a direct result of the flow reversal occurring in the channel. This increase is somewhat underpredicted in this study

compared to Desrayaud and Lauriat[10] The maximum difference is 3.6%. This is due to the underpredicted temperature near the inlet, which was discussed above.

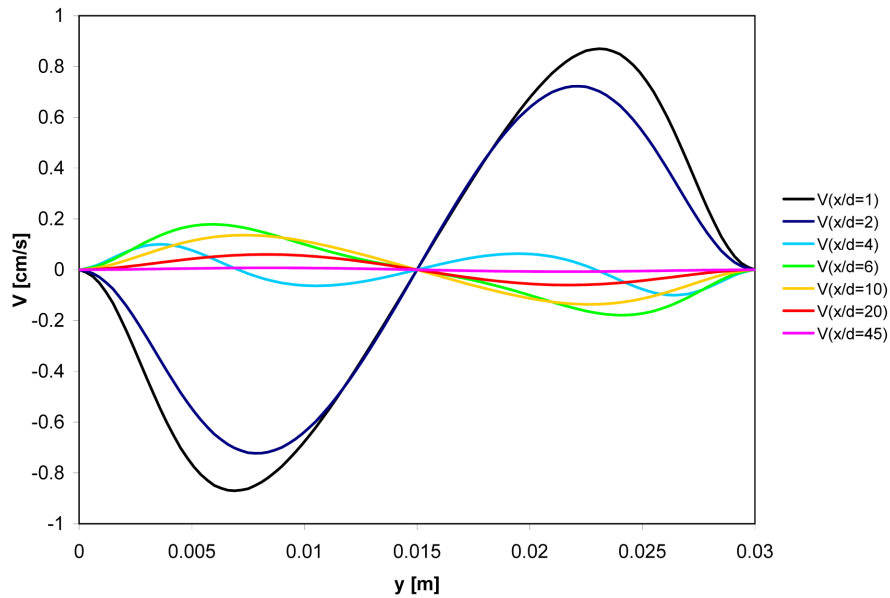


Figure 5.11: y-component of the velocity at different locations with respect to the axial coordinates.

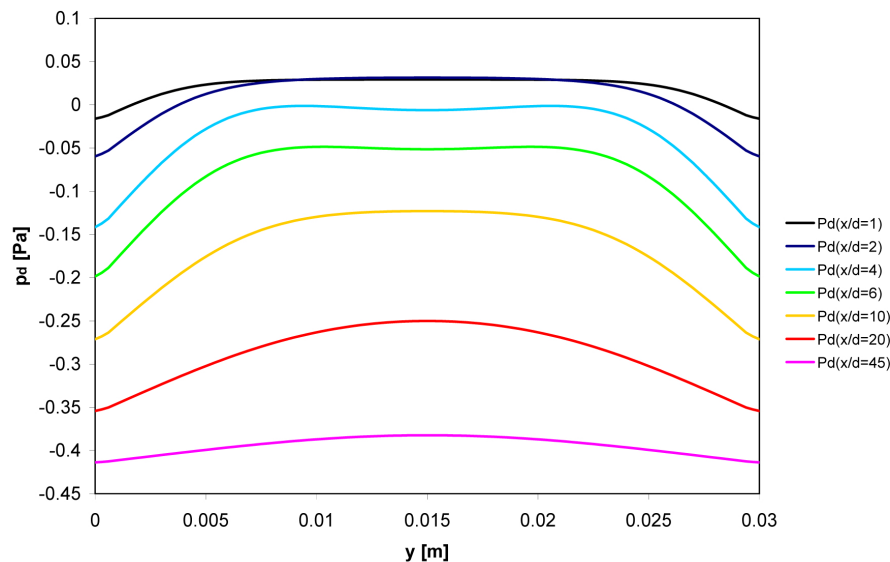


Figure 5.12: Dynamic pressure profiles at different locations with respect to the axial coordinate.

In figures 5.12 and 5.11 the dynamic pressure and the velocity component V (with respect to the y-coordinate) are plotted respectively. As the fluid near the wall becomes hotter, the axial velocity component U increases. This causes a local drop in the dynamic pressure p_d , as can be seen in figure 5.12. Because of this local pressure drop, fluid in the center of the channel is ‘sucked’ towards the wall, which can be seen in figure 5.11 at axial locations $x^*=1$ and $x^*=2$. Further downstream for $x^* > 6$, the temperature gradients in the direction of the channel height are smaller. Therefore, the density gradients are smaller as well. This causes the fluid near the wall to decelerate, which in turn decreases the dynamic pressure gradients. Thus, fluid near wall is pushed near the center. Near the end of the channel, the temperature gradient is very small and the dynamic pressure gradient has almost completely disappeared. The velocity profile here is almost parabolic again.

The results presented for the mixed convection case show that buoyancy forces are properly taken into account by the OpenFOAM code.

5.3 Fluids at supercritical pressures

5.3.1 supercritical carbon dioxide in a pipe geometry at 9.52 MPa

So far, only constant property cases and one case with small density variations have been used for the validation of the OpenFoam code. In order to show that the code handles cases with strong fluid property variations well, various cases from Jiang et al.[22] have been simulated. In this paper, numerical simulations, as well as experimental results are presented for supercritical CO₂ flowing through a vertical pipe geometry with $d=2$ mm and $L=40$ mm, at relatively low Reynolds numbers. Although Jiang et al.[22] describe results for supercritical CO₂ for two different pressures, only cases at a pressure of 9.52 MPa have been considered. At this pressure, the pseudocritical point is at $T=42.66^\circ$ C. In all cases considered, a fully developed supercritical CO₂ flow enters the pipe with a uniform enthalpy profile of h_{in} , which corresponds to an inlet temperature T_{in} and with a mass flux of G_{in} . At the wall the fluid is heated by means of a constant heat flux of q_w^* . The boundary conditions for all cases have been summarized in table 5.2.

Table 5.2: Description of the cases from Jiang et al.[22]. For each case, inlet enthalpy h_{in} , temperature T_{in} and mass flux G_{in} are shown, as well as the wall heat flux q_w^* .

Case	h_{in} (kJ/kg)	T_{in} ($^\circ$ C)	q_w^* (kW/m ²)	G_{in} (kg/m ² s)
I	293.283	35.00	13.0	64.954
II	256.471	24.60	4.49	66.081
III	256.471	24.60	13.70	66.585
IV	256.471	24.60	26.30	70.024
V	256.471	24.60	36.80	72.764
VI	256.471	24.60	12.30	86.115
VII	256.471	24.60	12.30	43.057

The cases are graphically represented in figure 5.13.

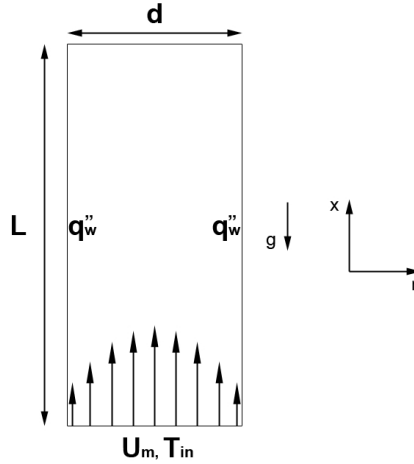


Figure 5.13: Graphical representation of the case selected from Jiang et al.[22].

For cases I-V, mesh sensitivity analyses were carried out. The results of which can be found in tables 5.3 - 5.7. It was found, that 120 cells in the radial direction and 800 cells in the axial direction were sufficient (change in values $<0.5\%$ for finer mesh). Extra cells in the radial direction did not improve the solution much (the change in the represented values is less than 0.5%) in cases I and V (tables 5.3 and 5.7). The biggest improvement is seen in the minimum density. In cases III, IV and V, the same number of cells as described in [22] was used: 150 cells in the radial direction and 2000 cells in the axial direction. In all of these cases, the represented values do not deviate much (less than 0.5%) from the coarser mesh (with only 800 cells in the axial direction), with the exception of the minimum density in case IV. Both in case IV and V, relatively large changes in density are seen for different meshes. This may be related to convergence issues. It was seen in these cases that convergence was difficult to achieve, especially for the largest meshes. It is a known issue in computational fluid dynamics, that simulating (near) turbulent flows as steady state flows causes problems for convergence (private communication[41]). In all of the cases from [22], the Reynolds number is very close to or greater than the critical Reynolds number for tube flows of 2300. This claim is further investigated at the end of this section.

Table 5.3: Mesh sensitivity results for case I. Displayed are the number of cells in the r and x directions as well as the velocity and enthalpy at the coordinate $x/d = 13$, $r/d=0.45$, $U_{monitor}$ and $h_{monitor}$, the total pressure drop at the wall and the minimum and maximum value of the density.

N_r, N_x	$U_{monitor}$	$\Delta p _{wall}$	$h_{monitor}$	$\max(\rho)$	$\min(\rho)$
60,400	0.1464	-265.4	$3.087 \cdot 10^5$	692.5	266.5
120,800	0.1501	-265.6	$3.107 \cdot 10^5$	692.5	263.4
180,800	0.1508	-265.6	$3.106 \cdot 10^5$	692.5	262.7

Table 5.4: Mesh sensitivity results for case II. Displayed are the number of cells in the r and x directions as well as the velocity and enthalpy at the coordinate $x/d = 10$, $r/d=0.45$ (close to the wall), $U_{monitor}$ and $h_{monitor}$, the total pressure drop at the wall and the minimum and maximum value of the density.

N_r, N_x	$U_{monitor}$	$\Delta p _{wall}$	$h_{monitor}$	$\max(\rho)$	$\min(\rho)$
60,400	0.05760	-316.3	$2.690 \cdot 10^5$	813.0	683.5
120,800	0.05780	-316.3	$2.690 \cdot 10^5$	813.0	682.2

Table 5.5: Mesh sensitivity results for case III. Displayed are the number of cells in the r and x directions as well as the velocity and enthalpy at the coordinate $x/d = 10$, $r/d=0.45$ (close to the wall), $U_{monitor}$ and $h_{monitor}$, the total pressure drop at the wall and the minimum and maximum value of the density.

N_r, N_x	$U_{monitor}$	$\Delta p _{wall}$	$h_{monitor}$	$\max(\rho)$	$\min(\rho)$
60,400	0.09048	-316.3	$2.764 \cdot 10^5$	813.0	338.3
120,800	0.09160	-316.1	$2.767 \cdot 10^5$	813.0	334.70
150,2000	0.09155	-313.0	$2.767 \cdot 10^5$	813.0	334.50

Table 5.6: Mesh sensitivity results for case IV. Displayed are the number of cells in the r and x directions as well as the velocity and enthalpy at the coordinate $x/d = 10$, $r/D=0.45$ (close to the wall), $U_{monitor}$ and $h_{monitor}$, the total pressure drop at the wall and the minimum and maximum value of the density.

N_r, N_x	$U_{monitor}$	$\Delta p _{wall}$	$h_{monitor}$	$\max(\rho)$	$\min(\rho)$
60,400	0.1227	-310.9	$2.802 \cdot 10^5$	813.0	204.2
120,800	0.1243	-311.0	$2.798 \cdot 10^5$	813.0	202.1
150,2000	0.1245	-311.0	$2.797 \cdot 10^5$	813.0	198.4

Table 5.7: Mesh sensitivity results for case V. Displayed are the number of cells in the r and x directions as well as the velocity and enthalpy at the coordinate $x/d = 10$, $r/d=0.45$ (close to the wall), $U_{monitor}$ and $h_{monitor}$, the total pressure drop at the wall and the minimum and maximum value of the density. *) For this mesh, the cells were smaller near the wall than they were at the centerline. The cell width ratio between them is 10.

N_r, N_x	$U_{monitor}$	$\Delta p _{wall}$	$h_{monitor}$	$\max(\rho)$	$\min(\rho)$
60,400	0.1487	-309.3	$2.846 \cdot 10^5$	813.0	159.8
120,800	0.1508	-309.8	$2.839 \cdot 10^5$	813.0	157.3
225*,800	0.1516	-310.0	$2.836 \cdot 10^5$	813.0	158.4
150,2000	0.1510	-309.8	$2.838 \cdot 10^5$	813.0	157.0

In figure 5.14, velocity profiles from case I are displayed at different axial locations in the pipe. Like the mixed convection of air case (see above), the fluid is accelerating near the heated wall due to buoyancy and is decelerating in the center of the pipe. It can be seen that the velocity near the wall at $r/d=0.5$ is slightly underpredicted compared to the numerical results of Jiang et al.[22] In

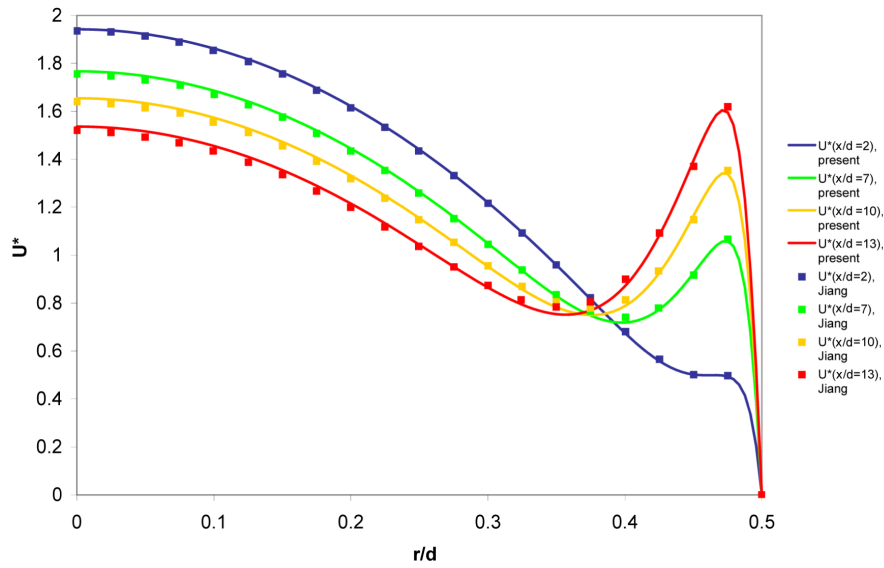


Figure 5.14: CASE I: velocity profiles at plotted at different axial locations. Results from [22] and present study.

the middle of the pipe, the results from the present study are slightly overpredicted, compared to Jiang et al.[22]. For $x/d=13$ this is a maximum difference of 1.5%.

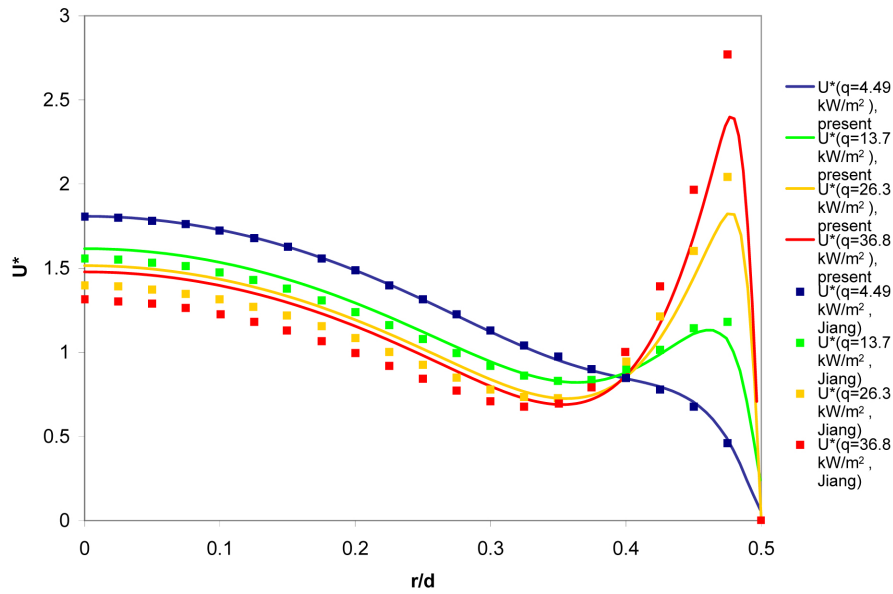


Figure 5.15: CASE II: velocity profiles at $\frac{x}{d} = 10$ for different wall heat fluxes. Results from [22] and present study.

In figure 5.15, the velocity profiles at $x/d=10$ are plotted for different wall heat fluxes. It can be seen that for the lowest wall heat flux there is excellent agreement between [22] and the present study. For higher heat fluxes, the present study is underpredicting the velocity near the wall, and overpredicting near the center of the pipe, compared to [22]. For $q_w''=13.7 \text{ kW/m}^2$, the biggest difference is 8.2%. For higher heat fluxes, the error is over 10%. A notable difference between Jiang's simulations and the present ones is that Jiang stopped the calculations if flow reversal occurred. The reason for this is not clear in Jiang et al.[22]. It is doubtful that, by using this criterion, a fully converged solution will be achieved. It was found in the present study that flow reversal for cases II-V can occur, *without a fully converged solution*. Even when stopping the simulation based on this criterion, the velocity profiles obtained were not really different from those already presented in figure 5.15.

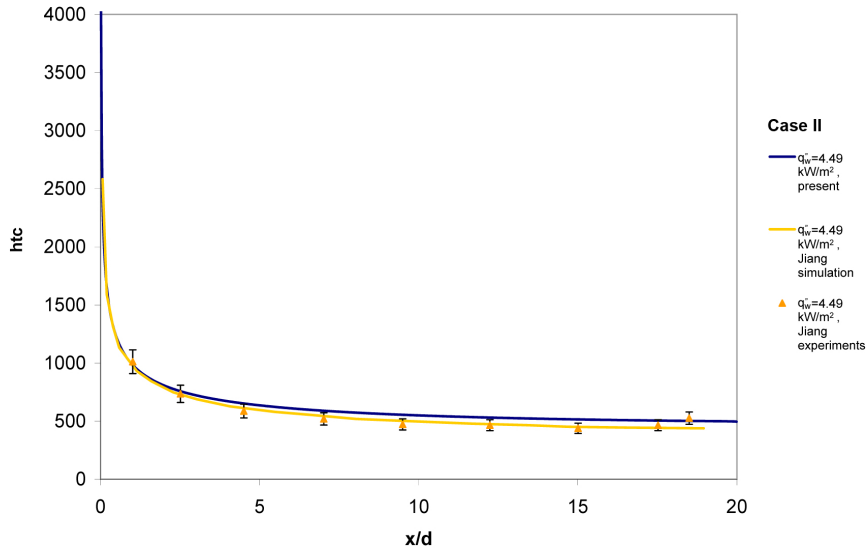


Figure 5.16: Case II with $q_w''=4.49 \text{ kW/m}^2$. Numerical and experimental results from [22] as well as the numerical results from the present study are shown.

For cases II-V, the heat transfer coefficient was calculated and compared with the experimental values from Jiang. The results are displayed in figures 5.16 to 5.19. Jiang et al.[22] calculated the heat transfer coefficients differently than was done in the present study (see sections 2.5.1 and 4.2.4). It was found that both methods give results that differ by less than 1%. The root mean square experimental uncertainty reported in Jiang et al.[22] is 10.1%.

For the lowest heat flux (figure 5.16), it is seen that the results of the present study are overpredicted (13% at most) and that Jiang's numerically predicted values are in better agreement with his experimental values/trends. The overprediction of the heat transfer coefficient is not within the experimental uncertainty reported by Jiang et al.[22].

For a wall heat flux of $q_w''=13.7 \text{ kW/m}^2$ (figure 5.17), the results for $x/d < 15$

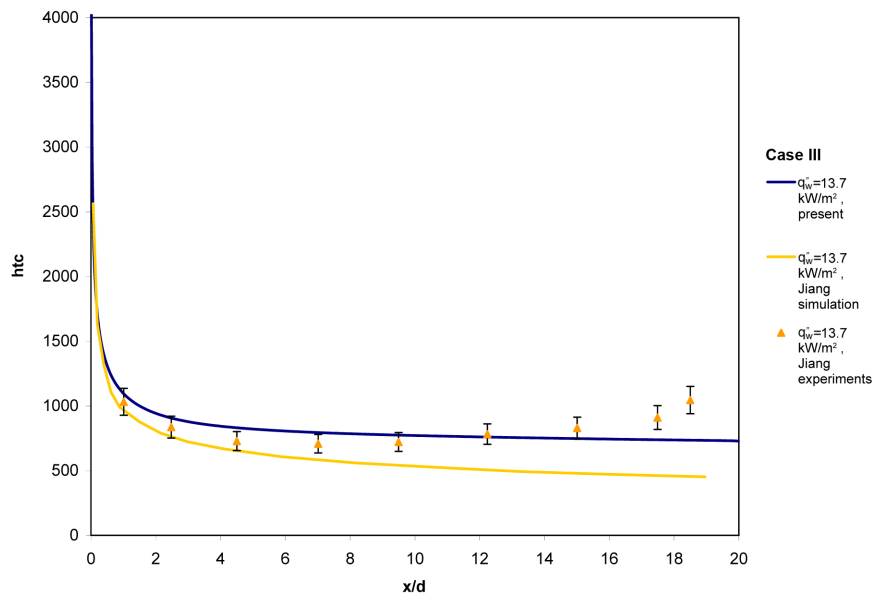


Figure 5.17: Case II with $q_w = 13.7 \text{ kW/m}^2$. Numerical and experimental results from [22] as well as the numerical results from the present study are shown.

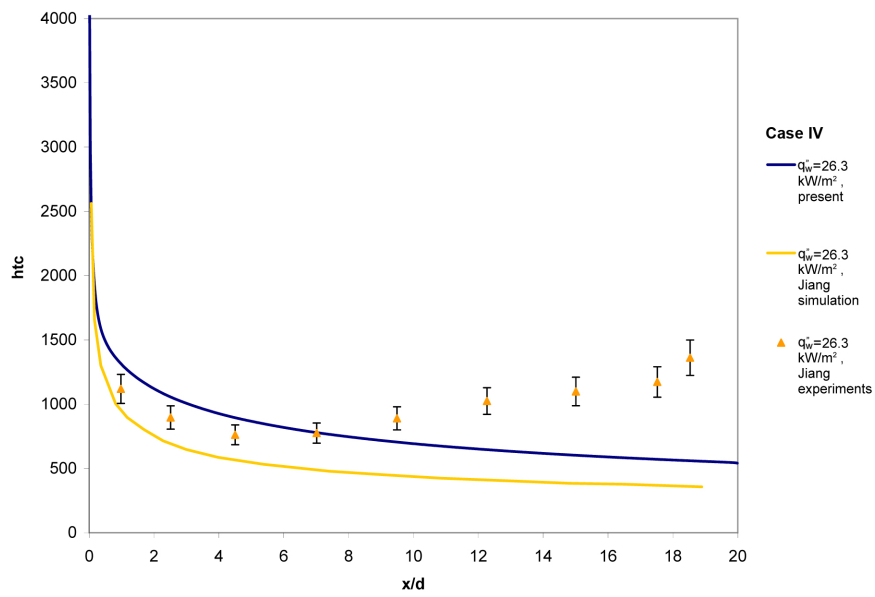


Figure 5.18: Case II with $q_w = 26.3 \text{ kW/m}^2$. Numerical and experimental results from [22] as well as the numerical results from the present study are shown.

are within 15% of the experimental values. Jiang's numerically calculated values are off by more than 20% for $x/d > 7$.

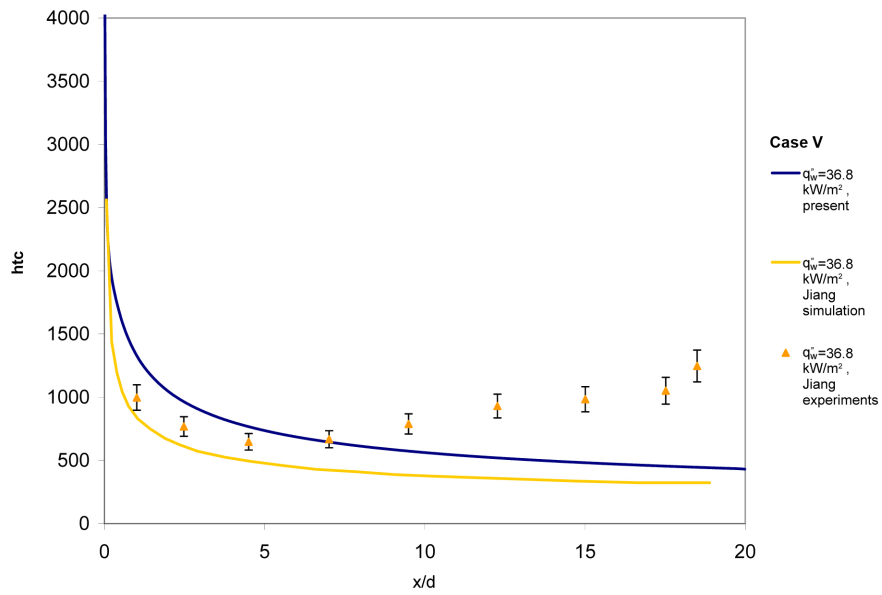


Figure 5.19: Case II with $q_w''=36.89 \text{ kW/m}^2$. Numerical and experimental results from [22] as well as the numerical results from the present study are shown.

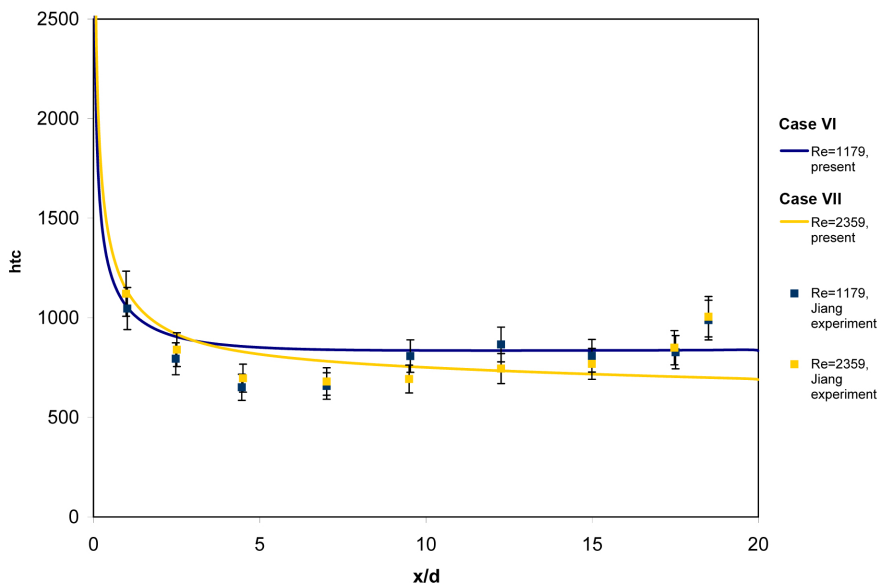


Figure 5.20: Case VI and VII with for $q_w''=12.3 \text{ kW/m}^2$. Experimental results from [22] as well as the numerical results from the present study are shown.

For higher heat fluxes, displayed in figures 5.18 and 5.19, both the numerical results from Jiang as well as those from the present study do not match well with the experimental values.

In figure 5.20, the heat transfer coefficients for two different inlet mass fluxes with the same heat flux ($q_w^r=12.3 \text{ kW/m}^2$) at the wall are shown. The difference in heat transfer is clearly visible. For a lower mass flux (case VII), the heat transfer coefficient is larger compared to the higher mass flux (case VI). However, the simulations of the present study do not capture the profile of the heat transfer coefficient correctly. The maximum percentile error is off by 17% for the low mass flux and 24% for the high mass flux.

In Jiang et al.[22] the effect of increased heat transfer, which is visible in all cases, except case II, is attributed to turbulence. However, this claim is only partially substantiated in the paper by using a $k - \epsilon$ model. The shear stress at the wall does increase dramatically due to buoyancy. So near the wall, the occurrence of eddies seems possible. The definition of Re_τ gives better insight [39],[46] :

$$Re_\tau = \frac{\rho u^+ D}{\mu} \quad (5.3)$$

in which $u^+ = (\tau_w/\rho)^{1/2}$, where τ_w is the shear stress at the wall. It can be calculated that $Re_\tau=149$ and 616 correspond to a regular Reynolds number in pipe flow of 2300 and 10000 respectively. For cases II-V, Re_τ has been calculated and is plotted in figure 5.21. According to this figure, cases IV and V enter a fully turbulent region for $x/d > 10.5$ and 14 (respectively). Case III is almost fully turbulent at the end of the pipe, whereas case II is in the transitional region at the end.

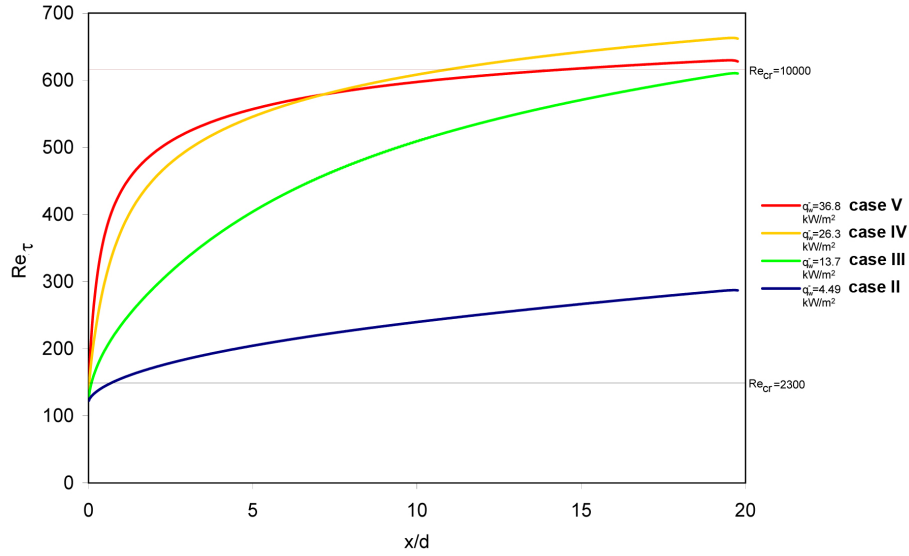


Figure 5.21: Re_τ as a function of axial length for cases II-V.

The above substantiates Jiang's claim that turbulence is the cause of the increased heat transfer. With the code used in the present study, it is impossible to capture increased heat transfer due to turbulence, due to the steady-state laminar formulation of the equation described in chapter 4 and (or) the lack of

turbulence modelling.

The results from the cases with supercritical CO₂ flowing vertically upward through a pipe show that the OpenFOAM code gives satisfactory results for cases with large variations in fluid properties for $q_w'' < 13.7 \text{ kW/m}^2$ and a mass flux of 66 to 73 kg/m²s (the deviation of the numerical results of the present study is less than 15% compared to the experimental values of Jiang et al.[22].)

5.3.2 supercritical water in a pipe geometry at 23 MPa

Because not all results described in the previous section were satisfactory, another case was investigated. A case by Xu et al. [55] describes water at 23 MPa flowing upwards through a pipe with $d=0.001 \text{ m}$ and $L=0.02 \text{ m}$. The water enters at 647 K and is heated at the wall by a constant heat flux $q_w'' = 50 \text{ W/m}^2$. The flow enters with a uniform velocity profile and a Reynolds number of $Re_{in}=1000$. The cases are graphically represented in figure 5.22.

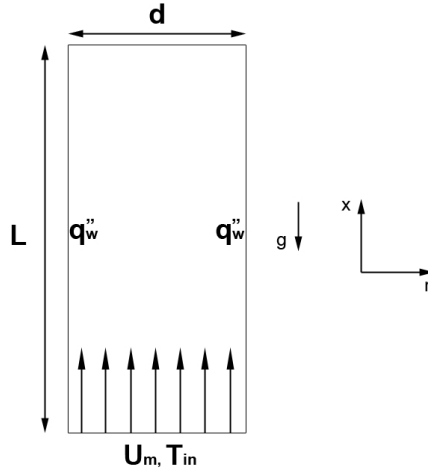


Figure 5.22: Graphical representation of the case selected from Xu et al.[55].

Mesh sensitivity analysis results are shown in table 5.8. For this particular case, almost no differences were seen for the two meshes that were investigated.

Table 5.8: Mesh grading results for validation of [55]. Displayed are the number of cells in the r and x directions as well as the velocity and enthalpy at the coordinate $x/d = 15$, $r/D=0.4$, $U_{monitor}$ and $h_{monitor}$, the total pressure drop at the wall and the minimum and maximum value of the density.

N_r, N_x	$U_{monitor}$	$\Delta p _{wall}$	$h_{monitor}$	$\max(\rho)$	$\min(\rho)$
80,600	0.01927	-923.9	$1.885 \cdot 10^6$	470.9	469.3
120,800	0.01926	-923.9	$1.885 \cdot 10^6$	470.9	469.3

In figure 5.23, radial velocity profiles are plotted at different axial coordinates. It can be seen that the results are in good agreement for $x/d < 15$ (the error

is smaller than 2.5% at $r/R = 0.5$, $x/d = 13$). However, at $x/d=15$, the velocity profiles from the present study and Xu et al.[55] differ significantly at the centerline (44% at $r/R=0$). At the maximum velocity near the wall, the error is 2.3%. In Xu et al.[55], no convergence criteria or discretization schemes are given, which makes it difficult to explain the differences. It was found that for not fully converged solutions, that the velocity profile at $r/R = 0$, $x/d = 15$, was higher than what is shown in figure 5.23. This could mean that the solution from Xu et al.[55] was not fully converged.

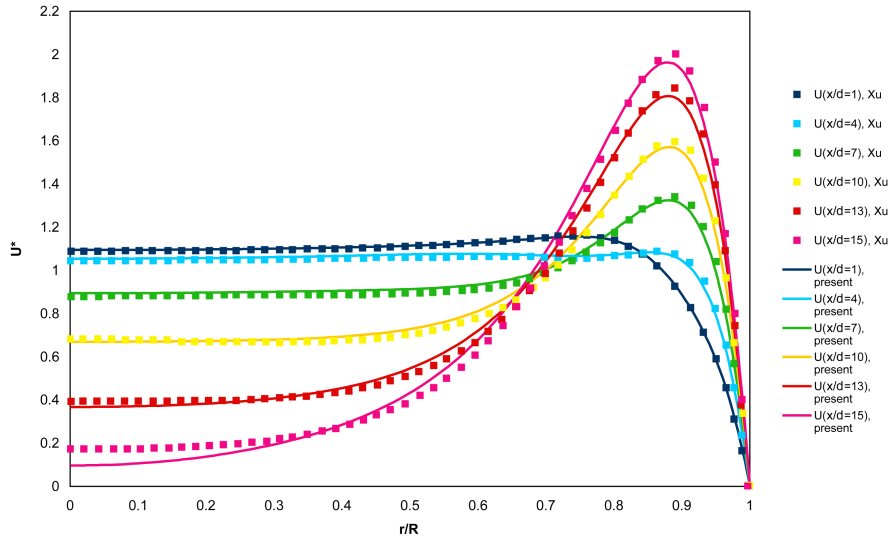


Figure 5.23: Dimensionless velocity profiles $\frac{U}{U_{in}}$ at different positions along the axial length. Results plotted are from [55] and present study

In figure 5.24, different dimensionless temperature profiles are plotted at different axial coordinates. The results are in good agreement. The largest deviation in dimensionless temperature is less than 2%.

The Nusselt number and the friction factor (presented in Xu et al.[55] as $4fRe$) were calculated along the axial length of the pipe and compared with results from Xu et al.[55]. The results are shown in figures 5.25 and 5.26. It can be seen that the overall shape of both dimensionless numbers agree well with the numerical results from Xu et al. The error for the Nusselt number at $x/d=1.4$ is 5.6%. At $x/d = 15$, the error is 1.8%. The error of the friction factor at $x/d=6.5$ is 4%.

Although the temperatures of the present study are slightly lower than those of Xu et al.[55] (for $x/d < 10$), this is not likely to be the cause of the lower predicted Nusselt numbers. In Xu et al.[55], the Nusselt number is not explicitly defined. The higher Nusselt numbers from Xu et al.[55] could also be the result of a not fully converged solution.

The near wall velocities at $x/d > 10$ are slightly lower in the present study than those of Xu et al.[55], which implies that the shear stress at the wall in the present study must be smaller as well. The lower shear stress accounts for the smaller friction factor. The steep decrease of the friction factor in the inlet

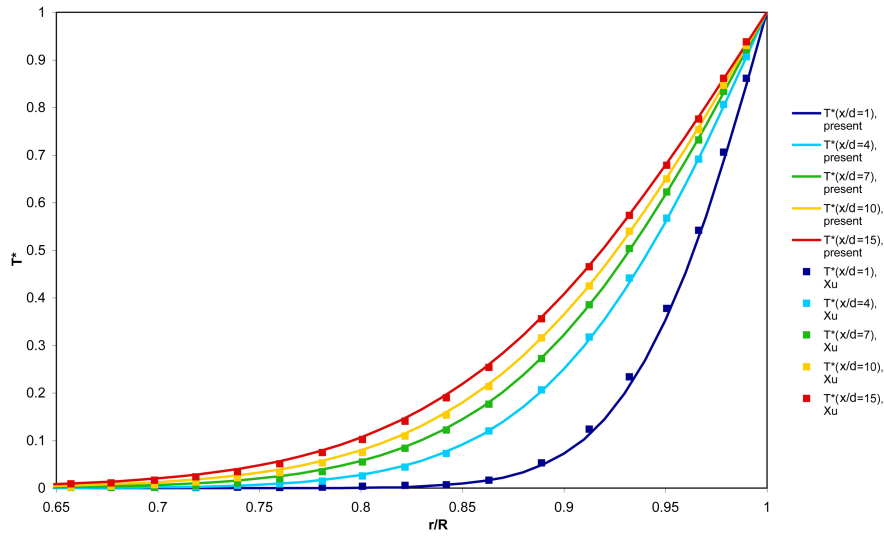


Figure 5.24: Dimensionless temperature profiles $\frac{T - T_{in}}{T_w - T_{in}}$ at different positions along the axial length. Results plotted are from [55] and present study

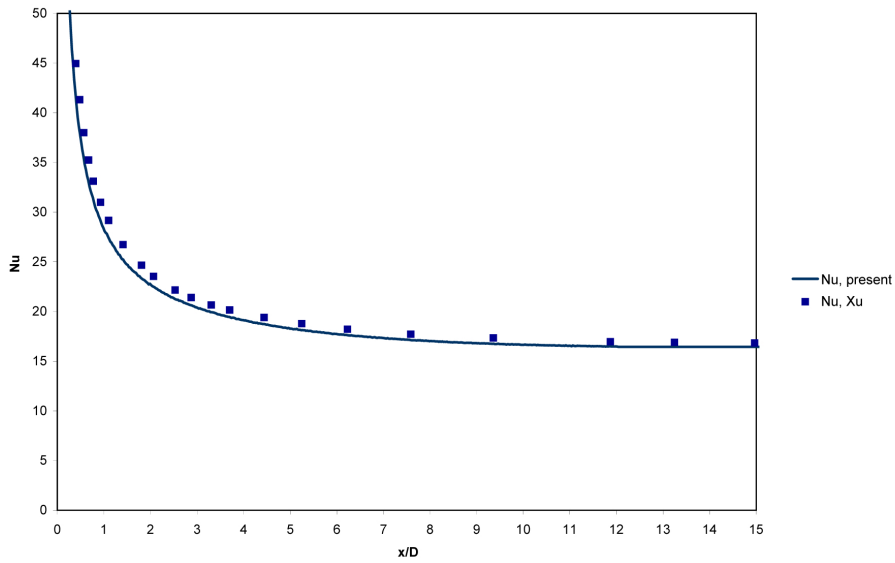


Figure 5.25: Nusselt number as a function of axial length. Results plotted are from Xu et al.[55] and present study

region is due to the uniform velocity profile at the inlet. The increase after that can be explained by the acceleration of the fluid near the wall, which causes the shear stress to increase. The decrease at the end is a bit more difficult to explain. In this region ($x/d > 11$), the shear stress at the wall is still increasing, which means, based on the definition of the friction factor, that $\rho \overline{U}^2$ must be

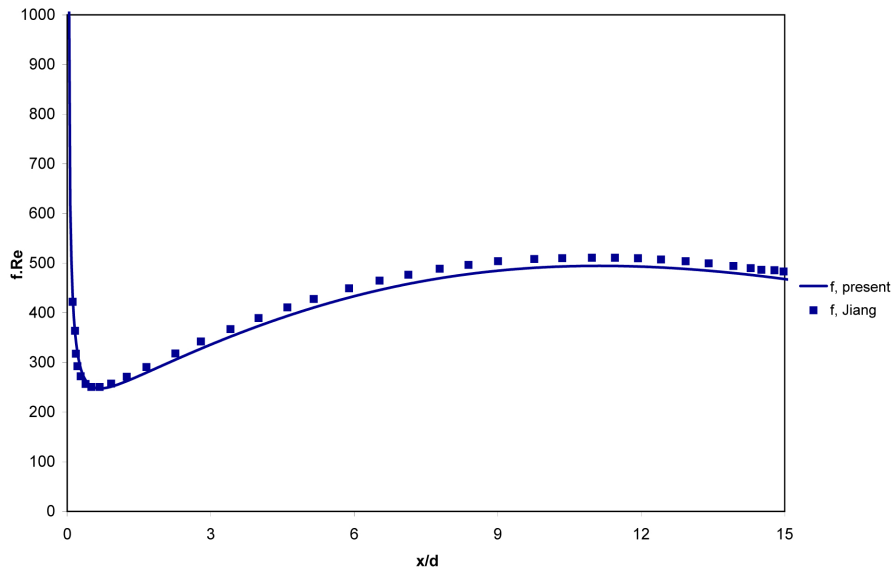


Figure 5.26: Friction factor as a function of axial length. Results plotted are from Xu et al.[55] and present study. The friction factor is presented here as $4fRe$. f is defined by equation 4.24

increasing more rapidly than before. In this region, the density must decrease more rapidly than before, causing the average velocity to increase and thus increase ρU^2 .

It is interesting to note here, that at $x/d > 15.5$ (not shown in figures), flow reversal occurs. In [55], nothing of this is mentioned. However, in [36], a criterion for flow reversal is given:

$$\frac{x_{reversal}}{d} = 0.016Re \quad (5.4)$$

This means that flow reversal for this case should occur at $x/d=16$, which is very close to where it happens in the current simulation.

The case with water at 23 MPa showed that there are notable differences between Xu et al.[55] and the present study. These differences are difficult to explain, because of the lack of information (especially regarding the convergence criteria and no. of cells used in the mesh).

5.3.3 supercritical water in an annular geometry at 25 MPa

Because one of the goals of this study is to simulate supercritical fluids flowing upwards in an annulus, another case was investigated. A recent paper by Zaim et al.[58], describes the numerical investigation of supercritical water flowing upwards through an annulus with temperatures near the pseudo-critical point. The ratio of the inner and outer radius, denoted as χ , equals 0.5. Water enters

the annulus, with $d = 2(R_o - R_i) = 0.001$ m and $L = 30d$ at 380°C and is heated by a constant heat flux at the inner wall. The outer wall is assumed to be adiabatic. The geometry dimensions given here are chosen in the present study, because the actual geometry size is not described in [58]; only non-dimensional numbers are given. The inlet conditions given are: $Re_{in} = 250, 500, 1000$ and 1500 , while the Grashof number equals $6.4 \cdot 10^5$. Based on these numbers, the inlet velocity and wall heat flux were calculated. The mesh used here contained 100 cells in the radial direction and 300 cells in the axial direction. The cases are graphically represented in figure 5.27.

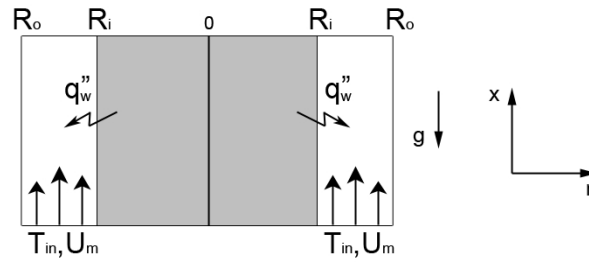


Figure 5.27: Graphical representation of the case selected from Zaim et al.[58].

The calculated velocity profiles at the outlet of the annulus by Zaim et al.[58] and the present study are shown in figure 5.28.

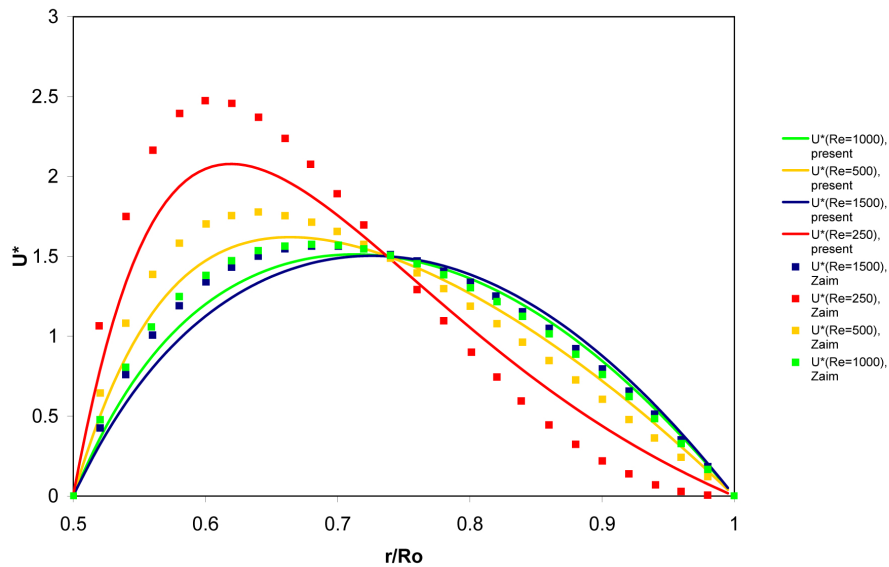


Figure 5.28: Velocity profiles at outlet for different inlet Reynolds numbers and $Gr = 6.4 \cdot 10^5$.

The results from the present study match poorly with those of Zaim et al.[58]. This results is rather unexpected, because there is reasonable to excellent agree-

ment with Jiang et al.[22] and Xu et al.[55]. This finding was further investigated by changing the geometry's dimensions while keeping the non-dimensional numbers (Gr and Re) the same. This investigation lead to the same conclusion. In the case with $Re_{in}=250$, the mesh was refined with 200 cells in the radial direction. The differences in results were negligible. A big difference between Zaim's study and the present is that in their case, the hybrid discretization scheme is used for the convective terms in Zaim et al.[58]. Changing the discretization scheme from upwind to hybrid in the present study did not change the results. Finally, in order to try to reproduce Zaim's results, the Grashof number was changed to $Gr=1 \cdot 10^6$, simply because it is mentioned elsewhere in the paper. These results are presented in figure 5.29.

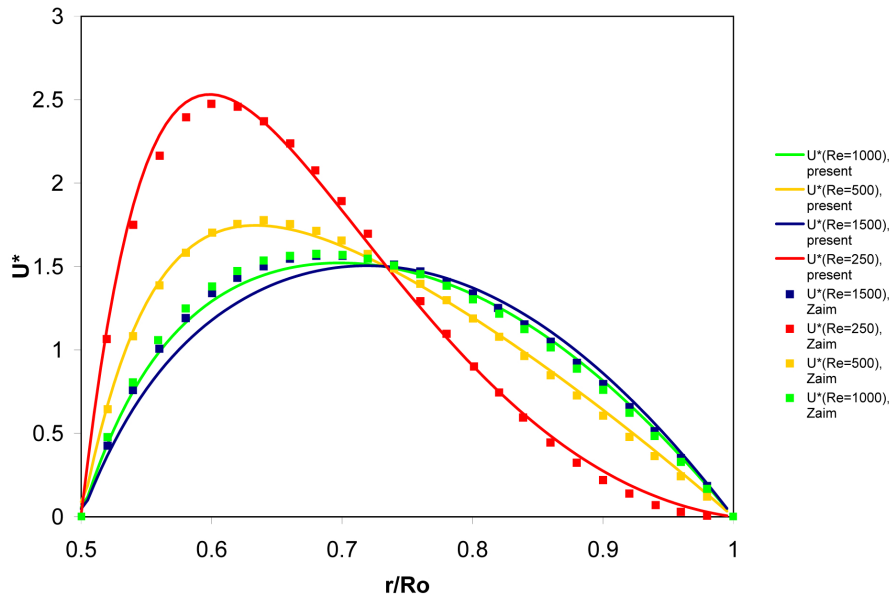


Figure 5.29: Velocity profiles at outlet for different inlet Reynolds numbers and $Gr = 1 \cdot 10^6$

With $Gr=1 \cdot 10^6$, the results from the present study match much better with the results from Zaim et al.[58] for $Re_{in}=250$ and 500. There is still a significant difference for $Re_{in} = 1000$ and 1500 (the error is of order 10%).

In summary, the results of the present study match poorly with Zaim et al.[58]. Possible explanations were investigated, but the exact reason has not been found.

5.3.4 supercritical water in a pipe geometry at 25 MPa

Because the validation of Zaim et al.[58] did not yield satisfactory results, a case from Jiang et al.[21] was considered. In this case, fully developed water flows upwards through a pipe with a constant temperature T_{in} of 657.2 K. The wall temperature of the pipe is kept at 659.2 K. The pipe has a diameter of 2 mm and a length of 200 mm. The mass flux G_{in} at the inlet is 35 kg/m²s. Results

of the mesh grading study can be found in table 5.9. The case is graphically represented in figure 5.30.

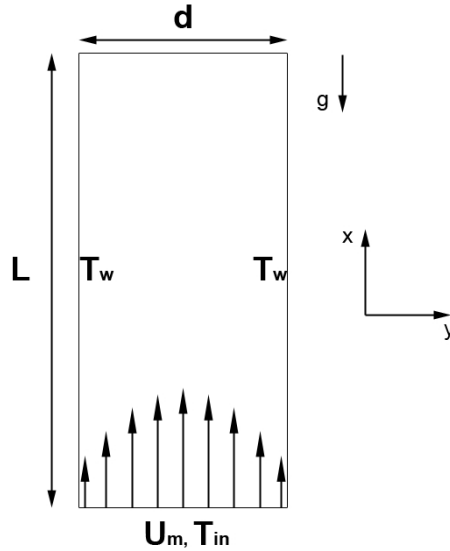


Figure 5.30: Graphical representation of the case selected from Jiang et al.[21].

Table 5.9: Mesh grading results for supercritical water at 25 MPa in a pipe geometry. Displayed are the number of cells in the r and x directions as well as the maximum velocity and the enthalpy at the centreline of the pipe at the outlet, the total pressure drop and the minimum and maximum value of the density.

N_x, N_r	U_{outlet}^{max}	Δp	h_{outlet}^{max}	$\max(\rho)$	$\min(\rho)$
700,80	0.171919	-679.885	$2.233 \cdot 10^6$	350.3	276.3
1000,120	0.172178	-680.010	$2.337 \cdot 10^6$	350.3	276.3
2000,200	0.172256	-680.020	$2.344 \cdot 10^6$	350.3	276.3

It can be seen that there are no significant changes in the results beyond a mesh of $N_r = 120$ cells, $N_x = 1000$ cells. The change for all parameters displayed in table 5.9 between the last two mesh-sizes are smaller than 0.5%.

In figure 5.31, the velocity profiles as calculated by Jiang et al.[21] and in the present study are shown for four axial locations x/d . There is very good agreement between the results. The largest difference can be seen at $r/d=0.3$, $x/d=100$; the difference is 2.6%, which is acceptable.

These last results for code validation presented here show that the OpenFOAM code is well suited for simulating supercritical flows.

5.4 Code Performance

Based on the results presented in section 5.1 it can be concluded that OpenFoam handles cases with constant properties very well, both for a channel and

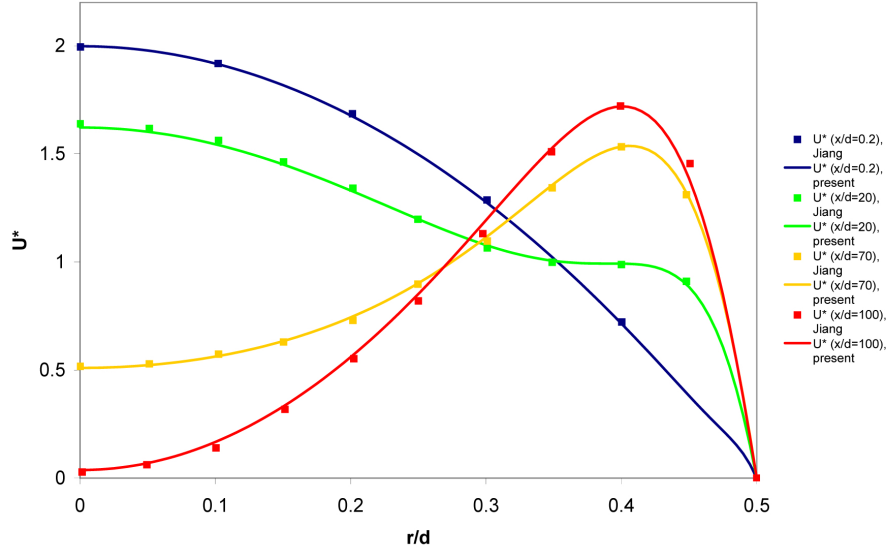


Figure 5.31: Velocity profiles at different axial location. Results plotted are from [21] and present study.

an annular geometry and for $Pe \geq 50$. The results for the mixed convection case show that buoyancy is properly taken into account in OpenFOAM. Because not all results of the supercritical cases were satisfactory, these cases were investigated further by calculating typical dimensionless numbers for those cases in order to find a range in which the OpenFOAM results are acceptable. The results of this study are presented in table 5.10:

Table 5.10: Code performance study. Displayed are the various supercritical cases and three dimensionless parameters. $q^+ = q_w^+ / (\rho U h_{in})$. ++ denotes good or excellent agreement, + moderate to good agreement and - unsatisfactory agreement.

<i>Case</i>		Re	Gr	q^+	Performance
Jiang et al.[22]	Case I	2360	$1.48 \cdot 10^6$	0.00068	++
	Case II	1810	$2.55 \cdot 10^5$	0.00027	++
	Case III	1824	$7.77 \cdot 10^5$	0.00077	+
	Case IV	1918	$1.49 \cdot 10^6$	0.0014	-
	Case V	1993	$2.09 \cdot 10^6$	0.0018	-
Xu et al.[55]		1000	$2.9 \cdot 10^7$	$4.9 \cdot 10^{-6}$	+
Zaim et al.[58]		250	10^6	0.000616	+
		500	10^6	$0.000308 \cdot 10^{-6}$	+
		1000	10^6	$0.000154 \cdot 10^{-6}$	+
		1500	10^6	$0.000103 \cdot 10^{-6}$	+
Jiang et al.[21]		1647	$1.2 \cdot 10^6$	NA	++

The cases taken from Zaim et al.[58] were considered here to be in moderate agreement, even though the exact case was not reproduced. However, the results were in good agreement with a slight alteration to the wall heat flux for the low

Reynolds numbers. The performance given in the table here is based on the discussion that was given for each case (see above). Based on the results of the performance study, it is seen that the OpenFOAM code gives good results if $q^+ < 0.001$.

Chapter 6

Investigation of the thermal boundary layer thickness in upward heated annular supercritical flows

This chapter is concerned with the investigation of the development of the thermal boundary layer in upward annular supercritical flows. To this end, an analytical study was made and a number of CFD- simulations were run. Different values for the mass flux and the uniform wall heat flux are chosen and the effects of these choices with respect to heat transfer phenomena are investigated. This chapter starts with the analytical derivations, which will give more insight into the problem of variable property flows: specific heat capacity c_p , density ρ and thermal conductivity λ . Subsequently, the CFD results are discussed. The chapter ends with a summary and a discussion.

6.1 Analytical considerations

6.1.1 Derivation of the thermal boundary layer thickness with variable properties

In chapter 3, an approximation for the temperature field in a channel has been derived. It has also been shown that the development length for the Graetz-Nusselt problem is a function of the Pe -number. In chapter 5, it was shown that using the integral approximation method for a case with a uniform wall heat flux results in good agreement with literature. The integral approximation method used there can also be used for the Graetz-Nusselt problem with variable density $\rho(T)$, variable specific heat capacity $c_p(T)$ or thermal conductivity $\lambda(T)$.

The use of a full equation of state to determine supercritical fluid properties, would result in very complex differential equations. Therefore, the effect of variable properties on the thermal development is studied here by varying one property at a time, while keeping the other properties constant. Also, simple

property relationships are used. A channel geometry is considered here; it was shown by Poole[45] and Weigand et al.[54] that heat and momentum transfer in annuli are almost the same as in channel flow for $R_i/R_o > 0.5$. The channel width amounts to $d=0.5$ mm and the wall at $y = d$ is adiabatic, while the wall at $y=0$ is heated.

Considering c_p and λ to be constant and using the following relationship for the density¹

$$\rho(x, y) - \rho_{in} = \rho_{in}\beta(T(x, y) - T_{in}) \quad (6.1)$$

the energy equation becomes:

$$\frac{\partial}{\partial x} \rho_{in}(1 + \beta(T - T_{in}))c_p UT = \frac{\partial}{\partial y} \lambda \frac{\partial T}{\partial y} \quad (6.2)$$

where

$$\beta = \frac{1}{\rho_{in}} \left(\frac{\partial \rho}{\partial T} \right)_{T_{in}} \quad (6.3)$$

Together with equations 3.25, 3.19 and 3.11 and by repeating the same steps as was done in section 3.3.2, a differential equation for $\delta(x)$ is obtained:

$$34Pe\beta \frac{q_w''}{\lambda} \frac{\delta^3(x)}{d^2} \frac{\partial \delta(x)}{\partial x} + 126Pe \frac{\delta^2(x)}{d^2} \frac{\partial \delta(x)}{\partial x} + 126Pe\beta T_{in} \frac{\delta^2(x)}{d^2} \frac{\partial \delta(x)}{\partial x} - 315 \quad (6.4)$$

which has the solution:

$$\frac{17}{84} \beta \frac{q_w''}{\lambda} Pe(\delta(x))^4 + (1 + \beta T_0) Pe(\delta(x))^3 - \frac{630}{84} x d^2 = 0 \quad (6.5)$$

A similar approach can be used c_p to find the thermal boundary layer thickness $\delta(x)$. Assuming a simple relationship for c_p :

$$c_p(x, y) - c_{pin} = c_{pin}\gamma(T(x, y) - T_{in}) \quad (6.6)$$

in which γ is defined as:

$$\gamma = \frac{1}{c_{pin}} \left(\frac{\partial c_p}{\partial T} \right)_{T_{in}} \quad (6.7)$$

and taking the same steps as before, the differential equation for $\delta(x)$ is given by:

$$34Pe\gamma \frac{q_w''}{\lambda} \frac{\delta^3(x)}{d^2} \frac{\partial \delta(x)}{\partial x} + 126Pe \frac{\delta^2(x)}{d^2} \frac{\partial \delta(x)}{\partial x} + 126Pe\gamma T_{in} \frac{\delta^2(x)}{d^2} \frac{\partial \delta(x)}{\partial x} - 315 \quad (6.8)$$

The corresponding solution for $\delta(x)$ is:

$$\frac{17}{84} \gamma \frac{q_w''}{\lambda} Pe(\delta(x))^4 + (1 + \gamma T_0) Pe(\delta(x))^3 - \frac{630}{84} x d^2 = 0 \quad (6.9)$$

¹This is reminiscent of the Boussinesq-approximation.

Using equation 6.5 or 6.9 in conjunction with equation 3.25, the temperature profile in the entry length can be (numerically) evaluated for cases with either variable density or specific heat capacity, respectively.

In order to model thermal conductivity as a function of temperature, a few extra steps are necessary. Consider the initial guess for the temperature profile:

$$T(x, y) = \frac{q_w^*}{\lambda_w(x)} \left(\frac{1}{2} \delta(x) - y + \frac{y^3}{\delta^2(x)} - \frac{1}{2} \frac{y^4}{\delta^3(x)} \right) + T_{in} \quad (6.10)$$

In which $\lambda_w(x)$ is the thermal conductivity at the wall ($y=0$). The thermal conductivity λ is modelled by:

$$\lambda(x, y) - \lambda_{in} = \lambda_{in} \epsilon (T(x, y) - T_{in}) \quad (6.11)$$

in which ϵ is defined as:

$$\epsilon = \frac{1}{\lambda_{in}} \left(\frac{\partial \lambda}{\partial T} \right)_{T_{in}} \quad (6.12)$$

An expression for $\lambda_w(x)$ still needs to be found. This can be done by evaluating equation 6.11 at the wall ($y=0$):

$$\lambda_w(x) = \lambda(x, 0) = \lambda_{in} \left(1 + \frac{1}{2} \frac{\epsilon q_w^* \delta(x)}{\lambda_w} (x) \right) \quad (6.13)$$

This gives for λ_w :

$$\lambda_w = \frac{1}{2} \lambda_{in} \pm \frac{1}{2} (\lambda_{in}^2 + 2 \lambda_{in} \epsilon q_w^* \delta(x))^{1/2} \quad (6.14)$$

The solution with a minus sign is dropped here: if q_w^* is considered to be zero, then $\lambda_w(x)$ should be λ_{in} and not zero. The same steps as before can be taken. The differential equation that describes $\delta(x)$ is given here:

$$\frac{\lambda_{in}^2 P e \frac{\delta^2(x)}{d^2} \left(\frac{\partial \delta(x)}{\partial x} \right)}{f(x)(\lambda_{in} + 2f(x))} - \frac{15 \lambda_{in} f(x)}{f(x)(\lambda_{in} + 2f(x))} - \frac{30 f^2(x)}{f(x)(\lambda_{in} + 2f(x))} + \frac{10 P e \lambda_{in} f(x) \frac{\delta^2(x)}{d^2} \left(\frac{\partial \delta(x)}{\partial x} \right)}{f(x)(\lambda_{in} + 2f(x))} = 0 \quad (6.15)$$

in which $f(x) = \lambda_w - \frac{1}{2} \lambda_{in}$. The solution of equation 6.15 is:

$$\delta(x) = \frac{45^{1/3}}{\lambda_{in} P e} \left(\left(\int_0^x \frac{f(x')}{\lambda_{in} + 10f(x')} dx' \right) \lambda_{in} + 2 \left(\int_0^x \frac{f^2(x')}{\lambda_{in} + 10f(x')} dx' \right) \right) \lambda_{in}^2 P e^2)^{1/3} \quad (6.16)$$

in which x' is a integration variable. It was assumed here that $f(x)$ is always real and that x is zero or positive. Equations 6.5 and 6.9 together with 3.25 form the solution for the temperature field for variable density and variable heat capacity in the entry region, respectively. Equation 6.16 together with equation 6.10 forms the solution for the temperature field with variable thermal conductivity in the entry region.

6.1.2 semi-analytical results

The thermal profiles for four cases (flow with constant properties, variable density, variable specific heat capacity or variable thermal conductivity) were calculated with Maple11. The inlet properties and the uniform wall heat flux ($y=0$) are given in table 6.1.

Table 6.1: Selected conditions for the analytical case. For constant property flow, β , γ and ϵ are zero. The values listed correspond to supercritical CO₂ at 9.52 MPa.

T_{in} (°C)	ρ_{in} (kg/m ³)	λ_{in} (W/mK)	$c_{p_{in}}$ (J/kgK)	β (1/K)	γ (1/K)	ϵ (1/K)	q_w'' (W/m ² K)
25.18	808	0.0898	2990	-0.0114	0.0270	-0.0146	5000

It was assumed here that the density decreases, that the specific heat capacity increases and that the thermal conductivity decreases with temperature. This corresponds qualitatively with a supercritical fluid where $T_{in} < T_{pc}$.

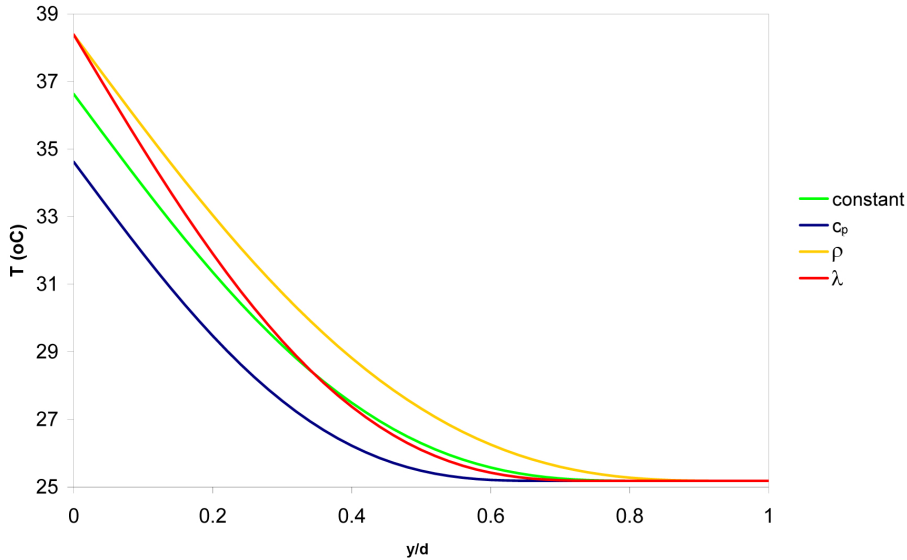


Figure 6.1: Temperature profiles for four different cases: constant properties, variable heat capacity c_p , variable density ρ , variable thermal conductivity λ .

The temperature profiles at $x/d=25$ are plotted as a function of the radial coordinate $r^* = \frac{r-R_i}{R_o-R_i}$ for the four cases in figure 6.1. It can be seen that a variable density leads to higher temperatures at the wall and that a variable specific heat capacity leads to lower temperatures at the wall compared to the constant property case. This effect can also be explained as follows: consider the convective term in the energy equation $\rho c_p U T$ as a radial average. If ρ becomes smaller, T must become higher² and if c_p becomes higher, T must become lower, because the same amount of heat is added to the system as in the constant property case. As a consequence, the Nusselt number, plotted in figure 6.2, is higher for

²compared to the constant property case.

the case with variable specific heat capacity and is lower with variable density. This last result is true, only if the velocity field does not change much due to differences in density, which is not likely to be the case in a real life situation. The approximation shows however that due to lower density, the fluid transports less heat per unit volume. To implement temperature-velocity coupling in the integral approximation method would be challenging. From literature, it is known that a fluid accelerated by buoyancy forces in upward laminar flows causes an increase in heat transfer (see chapter 2).

It can be seen in figure 6.1 that a variable thermal conductivity that decreases as the temperature becomes higher, leads to a higher temperatures near the wall and to lower temperatures far away from the wall. Considering Fourier's law of conduction at the wall, $q_w'' = -\lambda_w(x) \frac{\partial T}{\partial y}$, it is easily deduced that as λ decreases, $|\frac{\partial T}{\partial y}|$ must increase, for a constant wall heat flux.

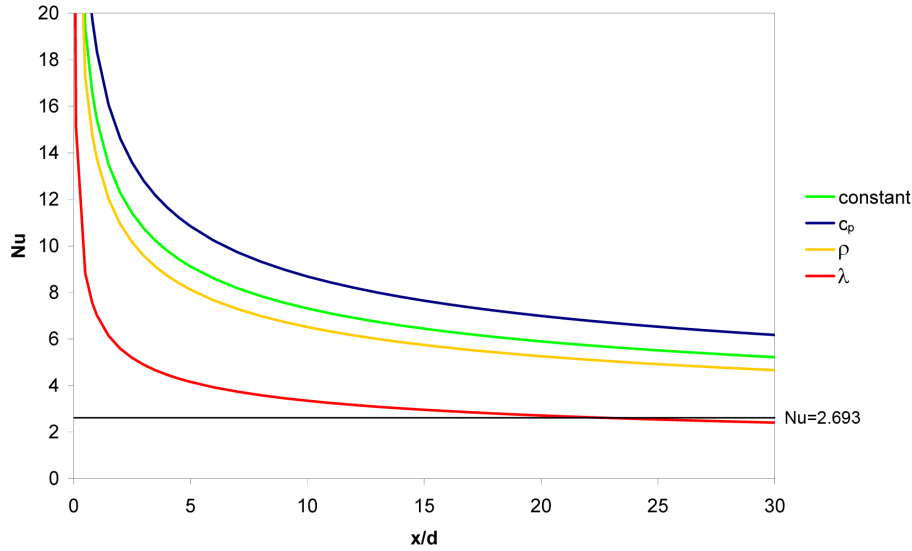


Figure 6.2: Nusselt number as a function of the axial length for four cases.

From the semi-analytical derivations and results above, it can be seen that the thermal boundary layer is increased for decreasing density (not considering acceleration effects) and decreased for increasing specific heat capacity. These changing properties lead to lower and higher Nusselt numbers, respectively. Decreasing thermal conductivity causes the thermal boundary layer and the Nusselt number to become smaller.

6.2 Numerical results for supercritical CO₂

Supercritical CO₂ at a pressure of 9.52 MPa and supercritical water at 25 MPa were simulated for different system parameters (inlet mass flux, wall heat flux) in an annular geometry. For all cases, the value of $q^+ = q_w'' / (\rho U h_{in})$ was kept below 0.001 in order to ensure the validity of the code (see section 5.4.). The

highest inlet Reynolds number (based on the hydraulic diameter) used in the simulations is 785, which is well below $Re_{cr}=2000$ for annuli; this likely ensures that the flow is laminar, even with acceleration effects.³

6.2.1 Geometry and mesh

The geometry considered (see figure 6.3) is an annulus with an outer radius $R_o=1.77$ mm and an inner radius of $R_i=1.27$ mm. The hydraulic diameter for this geometry $d = 2(R_o - R_i)=1$ mm. Fluid enters the annulus with a fully developed profile (equation 4.15) and a uniform enthalpy value h_{in} (which corresponds to a temperature of T_{in}). The length of the annulus is $L = 200D_h$. The outer wall is considered to be adiabatic and there is a uniform wall heat flux q_w'' at the inner wall. The mesh was set to $2000 * 100$ cells (axial \times radial)

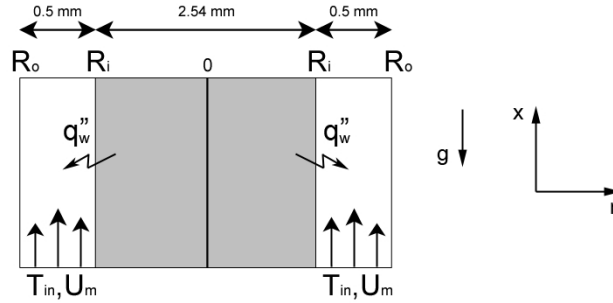


Figure 6.3: Graphic representation of the investigated case.

6.2.2 Numerical results for supercritical CO₂

In the numerical investigation with supercritical CO₂ (9.52 MPa), the effect of inlet velocity and wall heat transfer were studied; inlet velocities U_m were varied from 0.03 to 0.07 m/s, which correspond to Peclet numbers of 807 to 1883, and uniform wall heat fluxes q_w'' were varied from 2000-10000 W/m²K. The inlet temperature $T_{in} = 25.18^\circ\text{C}$. This temperature is much lower than the pseudo-critical temperature $T_{pc}=42.66^\circ\text{C}$. This means that as the temperature increases, the specific heat capacity increases up until $T = T_{pc}$ and that density and thermal conductivity decrease (for supercritical CO₂ at 9.52 MPa). The heat transfer coefficients are studied for different values of the wall heat flux first, for two Peclet numbers (807 and 1613). Next, the influence of the wall heat flux is studied in depth by looking at the radial profiles of velocity, temperature and the various properties. The effects seen here, explain the heat transfer phenomena (heat transfer coefficients as a function of the length of the annulus) presented before that. Subsequently, the effect that the wall heat flux and the inlet Peclet number have on the boundary layer thickness is studied. Finally, a relationship is proposed for the prediction of the axial coordinate where heat transfer is dominated by the property variations and where the inlet effect is no longer apparent.

³it was shown that in mixed convection flows the transition from laminar to turbulent flows can occur even at low Reynolds numbers, due to flow reversal. See chapter 2.

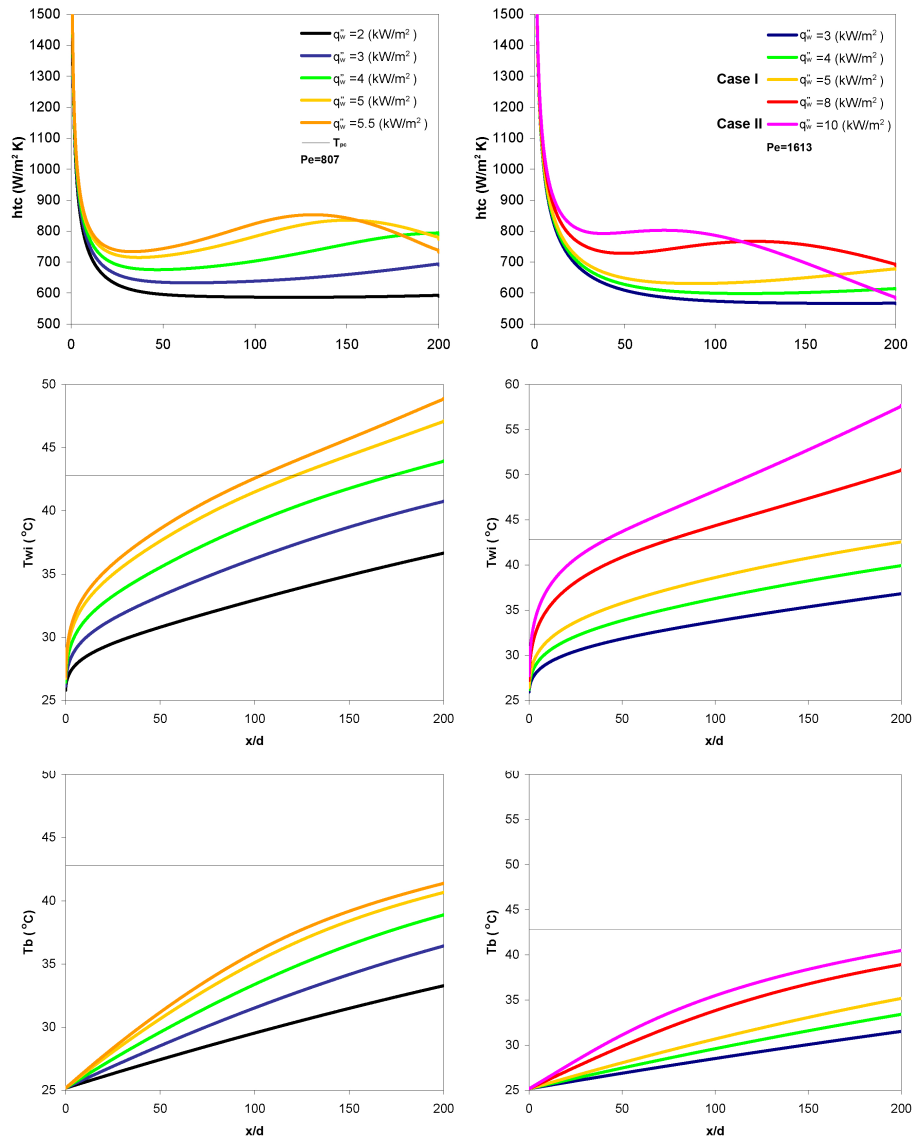


Figure 6.4: Heat transfer coefficient, inner wall temperature and bulk temperature as a function of the axial length for two different Pecllet numbers (807 and 1613 on the left and right respectively).

Heat transfer phenomena

The heat transfer coefficients htc , inner wall temperatures T_{wi} and bulk temperatures T_b are shown as a function of the axial length in figure 6.4. It can be seen that the heat transfer coefficient first sharply decreases, which is a direct result from the uniform temperature profile at the inlet (hereafter called the inlet effect). At some point along the annulus, the heat transfer coefficient starts to increase again. For four cases a maximum in the heat transfer coefficient

cient can be seen ($Pe = 807; q_w^* = 5$ and 5.5 kW/m^2 and $Pe = 1613; q_w^* = 8$ and 10 kW/m^2). This maximum lies between the axial point where $T_{wi} = T_{pc}$ and where $T_b = T_{pc}$. For higher heat fluxes the location of the maximum heat transfer coefficient shifts towards the inlet (This is consistent with, for example, Bae et al.[1]), while its value increases (which is typical in upward mixed convection, as was explained in chapter 2). The positions of the local minima near the inlet also shift toward the inlet for higher heat fluxes and for lower mass fluxes.

Influence of uniform wall heat flux

The phenomena described above can be further investigated by looking at the radial variations of U , T , c_p , λ and ρ . In figure 6.5, the radial velocity and temperature profiles are plotted for different positions of the axial length. In figure 6.6, radial profiles of c_p , λ and ρ are shown. These figures correspond to a case with $Pe=1613$, $q_w^* = 5000 \text{ W/m}^2\text{K}$ and $q_w^* = 10000 \text{ W/m}^2\text{K}$ (denoted as Case I and Case II, respectively). It can be seen that for case II, the velocity is much more accelerated than for case I (for $x/d > 150$, flow reversal occurs) and that the temperature gradients near the wall are larger, compared to case I.

From the analytical model, it followed that the heat transfer coefficient (Number) is increased due to increasing c_p and is decreased due to decreasing λ . From literature, it is known that, flow acceleration in laminar flows increases the heat transfer coefficient. All these effects are present in case I.

Looking at figure 6.6 (left column), it can be seen that the values of c_p increase at the wall up until the outlet, while λ and ρ decrease at the wall for case I. Figure 6.5 (left column) shows that the fluid near the heated wall is accelerated. It can be seen from figure 6.4, that, after the inlet effect, the heat transfer coefficient increases. Thus, the effects that an increase in c_p and acceleration have on heat transfer, outweigh the effects that a decrease in λ and in ρ (not considering the acceleration) have.

In case II, the wall heat flux is twice as large as in case I. In this case, a maximum in heat transfer is seen at $x/d=74$ in figure 6.4. It can be seen in this figure, that T_{wi} increases much faster due to the higher wall heat flux. This means that c_p increases much faster, while ρ and λ decrease much faster. The flow acceleration (figure 6.5 is larger than in case I, due to the larger radial differences in density (figure 6.6). Thus, up to the point where the heat transfer has a maximum, increasing c_p and acceleration outweigh decreasing ρ and λ . It can also be seen for this case that the region with high c_p moves away from the heated wall, while c_p at the wall decreases in figure 6.6 (right column). The dent seen in the λ profiles is due to the steep temperature gradient. After the point where a maximum in heat transfer occurs ($x/d > 74$), the fluid keeps accelerating (figure 6.5). However, c_p , λ and ρ decrease at the wall after $x/d > 74$, which causes the inner wall temperature to rapidly increase again (figure 6.4). The effects of a decrease in c_p , ρ (not considering the acceleration effect) and λ outweigh the effect that acceleration has on heat transfer, causing the heat

transfer coefficient to become smaller.⁴

From figures 6.5 and 6.6, it can be seen that the radial differences in velocity, temperature and in properties become larger for a higher heat flux. Due to the larger increase in T_{wi} for a higher wall heat flux, c_p increases faster and the flow is accelerated more (which may even lead to flow reversal). This causes the minima and maxima in heat transfer coefficients to move towards the inlet. The radial differences also create a region near the wall where the diffusivity (defined as $K = \frac{\lambda}{\rho c_p}$) is lower. This suggests that the thermal boundary layer

⁴These statements are only true for the cases that were investigated. For even higher heat fluxes, the effect of decreasing λ and decreasing ρ (not considering the acceleration effect) might be stronger than increasing c_p and acceleration. This was not investigated. The small difference between local minimum and maximum heat transfer coefficient seems to decrease with increasing heat flux. For a certain critical heat flux, the local maximum could disappear.

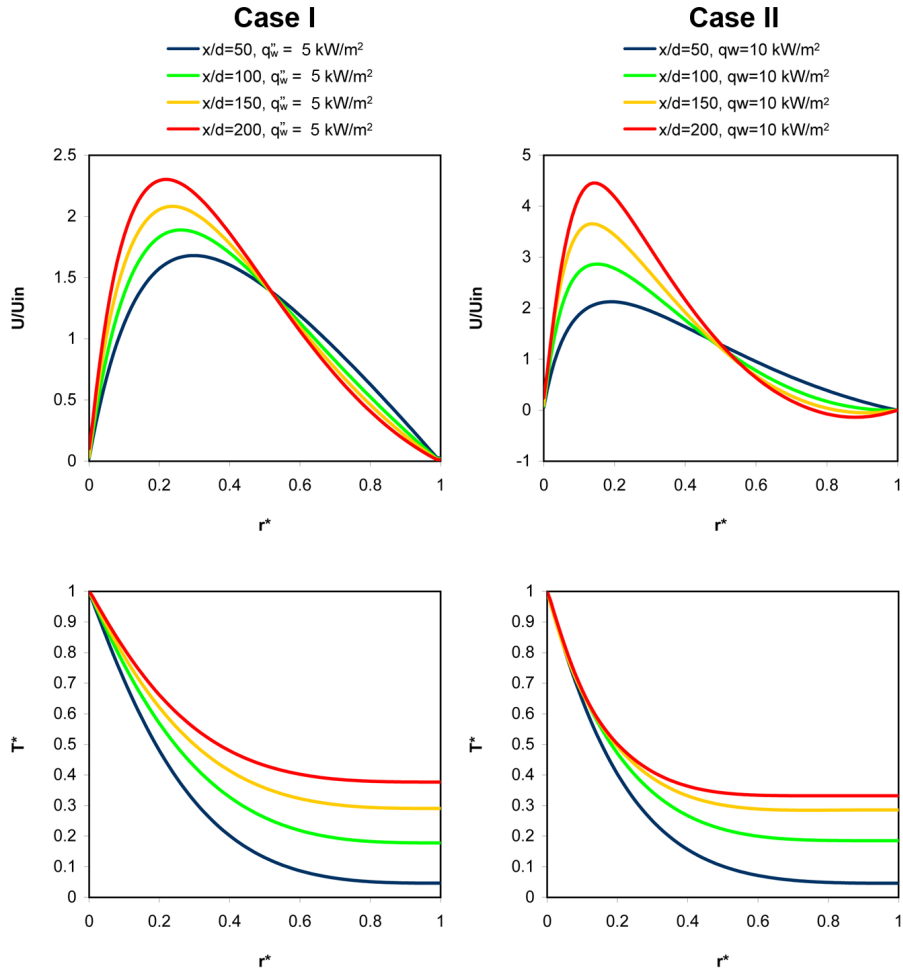


Figure 6.5: Radial plots of velocity U/U_{in} and temperature ($T^* = \frac{T-T_{in}}{T_w-T_{in}}$) for different positions along the axial length of the annulus (x/d). $Pe=1613$. $q_w = 5000 \text{ W/m}^2\text{K}$ (left column) $q_w = 10000 \text{ W/m}^2\text{K}$ (right column).

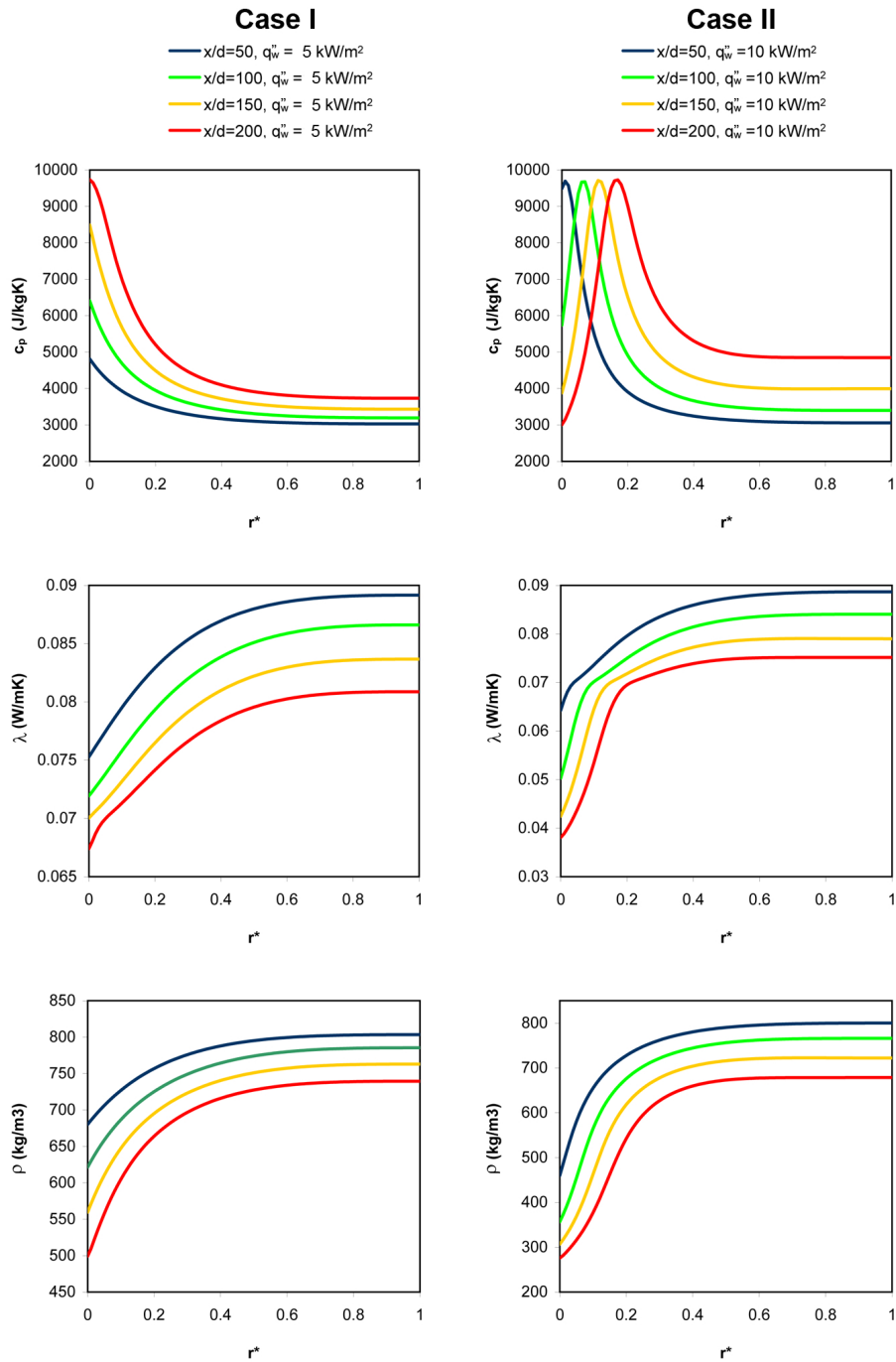


Figure 6.6: Radial plots of the properties ρ , c_p and λ for different positions along the axial length of the annulus (x/d).

becomes smaller if the heat flux is increased; this is investigated below.

Influence of wall heat flux and inlet mass flux on the thermal boundary layer

The thermal profile of three cases in the developing region ($x/d=10$) have been plotted in figure 6.7. From this figure it can be seen that lowering the inlet mass flux (or Pe-number) causes the boundary layer to be larger. This is qualitatively speaking not different from constant property cases. A higher wall heat flux causes the boundary layer to become smaller. This effect is partially due to the increase in c_p and the decrease in λ . For a higher heat flux, λ and c_p decrease and increase more quickly, respectively. It was shown before that an increase in c_p and a decrease in λ makes the boundary layer smaller. The decrease in density (not considering acceleration) enlarges the thermal boundary layer.

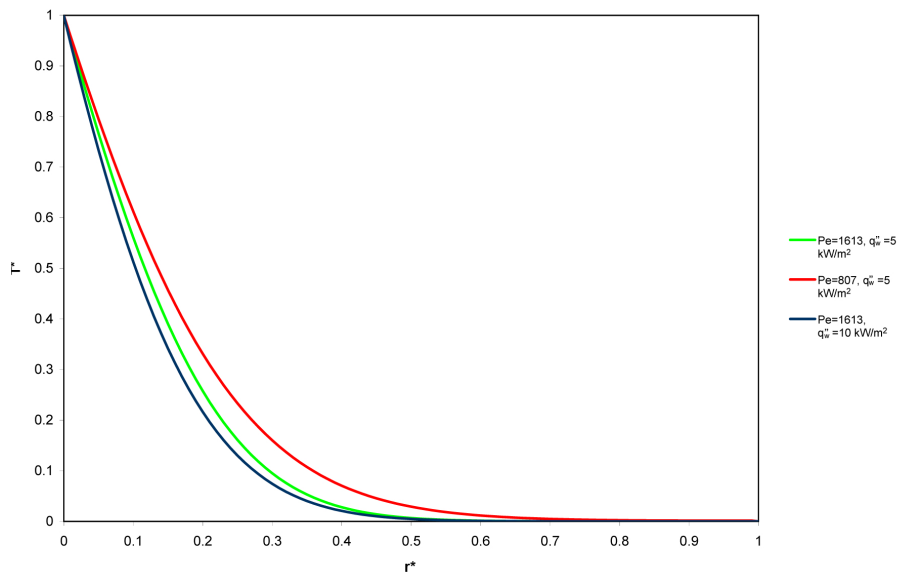


Figure 6.7: Radial plots of the temperature profile for three cases at an axial position $x/d=10$.

Local heat transfer enhancement

It was explained in the previous section that the local increase in heat transfer coefficient is due to the increase in c_p and due to acceleration. The sharp decrease in the heat transfer coefficient very near to the inlet is due to the uniform temperature profile imposed at the inlet. Thus the local minimum, or onset of local heat transfer enhancement, can be regarded as the point where the variation of properties becomes dominant and the point where the inlet effect is no longer apparent. The length between this point and the inlet is called here *the thermal boundary layer development length* L_{thb} .

In the cases presented in figure 6.4, it is seen that the minimum in the heat transfer coefficients shifts towards the inlet for increasing wall heat flux and decreasing mass flux. It is also seen that for a larger heat flux the shift becomes smaller. This is due to the steeper increase in c_p . Looking at the minimum for $Pe=807$, $q_w''=5000$ kW/m² and $Pe=1613$, $q_w''=10000$ kW/m² it is found that the minimum occurs at $x/d=37$ and $x/d=38$, respectively. This suggests that the heat transfer coefficient minima for different cases occur at the same position if q_w''/Pe is of the same value.

Before looking further into this however, it is interesting to look one more time at equations 6.5, 6.9 and 6.16. These functions show that the boundary layer is a function of q_w'' , Pe , β , ϵ , γ and T_{in} . It is assumed here that the length at which the inlet effect disappears directly related to the development of the boundary layer thickness. The length at which the inlet effect disappears is therefore also written as a function of these parameters. Using dimensionless forms of these parameters, it is proposed here that:

$$L_{thb}/d = f \left(Pe, \beta \frac{q_w'' d}{\lambda}, \gamma \frac{q_w'' d}{\lambda}, \epsilon \frac{q_w'' d}{\lambda}, \beta T_{in}, \gamma T_{in}, \epsilon T_{in} \right) \quad (6.17)$$

To study the effect of inlet Peclet number and wall heat flux, the effect of the inlet temperature is not considered in the remainder of this chapter. To investigate the claim that a minimum in heat transfer occurs at the same axial position if q_w''/Pe is of the same value, L_{thb} was plotted against the dimensionless parameter $\frac{\beta q_w'' d}{\lambda Pe}$ in figure 6.8.

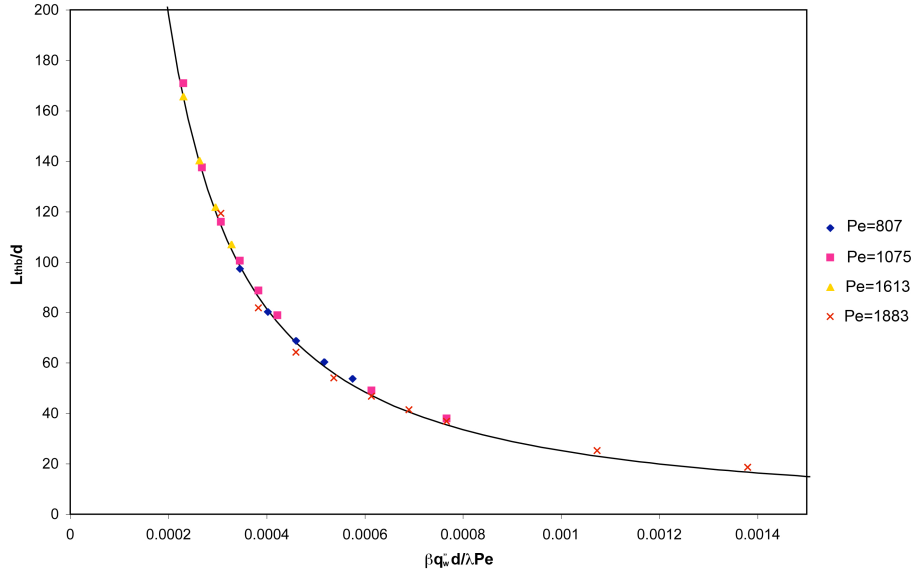


Figure 6.8: L_{thb} plotted against $\frac{\beta q_w'' d}{\lambda Pe}$.

To make this plot, the four listed Peclet numbers were investigated while varying the wall heat flux in a range of $q_w''=1-10$ kW/m². The position of the minimum

was in some cases (roughly $L_{thb}/d > 150$) difficult to find, due to small oscillations (typically of order ± 0.1) in the heat transfer coefficient near the minimum. In those cases, the axial coordinate was interpolated as the average of two coordinates with clearly a higher h_{tc} than the oscillating part ($+0.5 \text{ W/m}^2\text{K}$). The oscillatory part was not longer than $3d$. Not all cases showed a minimum in heat transfer. It is possible that this minimum occurs at $x/d > 200$ or that it never occurs at all. From figure 6.8 it can be seen that L_{thb} becomes smaller for higher values of q_w'' and for lower values of Pe . The reason for this is already discussed above. To model this behaviour, a suitable function is selected of the form (also shown in figure 6.8):

$$L_{thb}/d = a \left(\frac{\beta q_w'' d}{\lambda Pe} \right)^b \quad (6.18)$$

With Origin 7.5, it was found that $a = 0.0036$ and $b = -1.2816$ and their respective standard errors are 0.0005 and 0.0161. To see how well this equation predicts the simulation results of L_{thb} , a comparison is presented in figure 6.9.

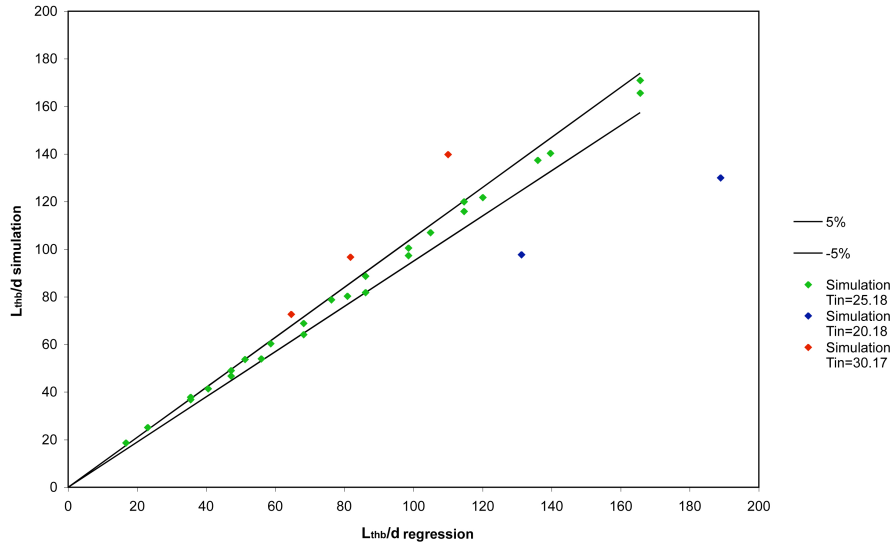


Figure 6.9: Numerical results of the supercritical CO_2 cases, plotted against equation 6.18. Also shown are the values of equation 6.18 $\pm 5\%$.

It can be seen that the equation predicts L_{thb} mostly within $\pm 5\%$ of the simulation value. Five other cases are plotted in figure 6.9 as well. Two cases with an inlet temperature of $20.18 \text{ }^\circ\text{C}$ and three cases with an inlet temperature of $30.17 \text{ }^\circ\text{C}$. Equation 6.18 does not accurately predict L_{thb} for these inlet temperatures. This means that the inlet temperature has to be taken into account into equation 6.18 as well. The dimensionless parameters presented in equation 6.17 could be of use here. This was not investigated, because there is too little data available with regard to inlet temperature.

6.3 Numerical results for supercritical water

Heat transfer to supercritical water at 25 MPa was investigated as well, but to a lesser extent. The same geometry was used, however, this time with supercritical water entering the annulus with a fully developed velocity profile and a uniform temperature profile of $T_{in}=330^{\circ}\text{C}$. The heat transfer coefficient was investigated for $Pe=236$ and 393 . The wall heat flux was varied from 10 kW/m^2 to 24 kW/m^2 . The heat transfer coefficient for $Pe=393$ and four wall heat fluxes is shown in figure 6.10.

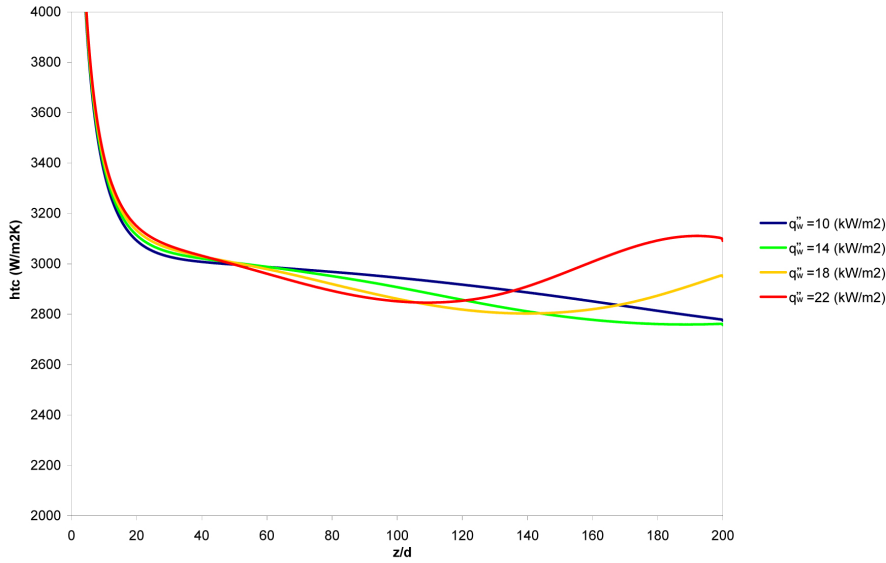


Figure 6.10: Heat transfer coefficient plotted as a function of the axial length for supercritical water (25Mpa).

The cases presented in figure 6.10 show some similarities with the supercritical CO_2 cases. Both show the inlet effect and an increase in heat transfer coefficient. The supercritical water heat transfer coefficients also show a slight dent just after the inlet effect. This is possibly due to the property variations.

The minima were investigated further using the same methods as in the previous section. The location of the minima are plotted in figure 6.11 as a function of $\frac{\beta q_w'' d}{\lambda Pe}$ in figure 6.11. Equation 6.18 was used again to fit the numerical data. It was found that $a=0.0181 (\pm 0.0035)$ and $b=-1.1163 (\pm 0.0243)$.

Although far less data was used in the numerical simulations of water, the data seem to indicate that L_{thb} is a function of $\frac{\beta q_w'' d}{\lambda Pe}$. To check the accuracy of the power regression, the numerical data was plotted against the values predicted by equation 6.18 in figure 6.12.

It can be seen that equation 6.18 predicts the numerical data within 5%. From the results presented for water at 25 MPa, it can be seen that the onset of local heat transfer enhancement can be predicted in the same manner as for CO_2

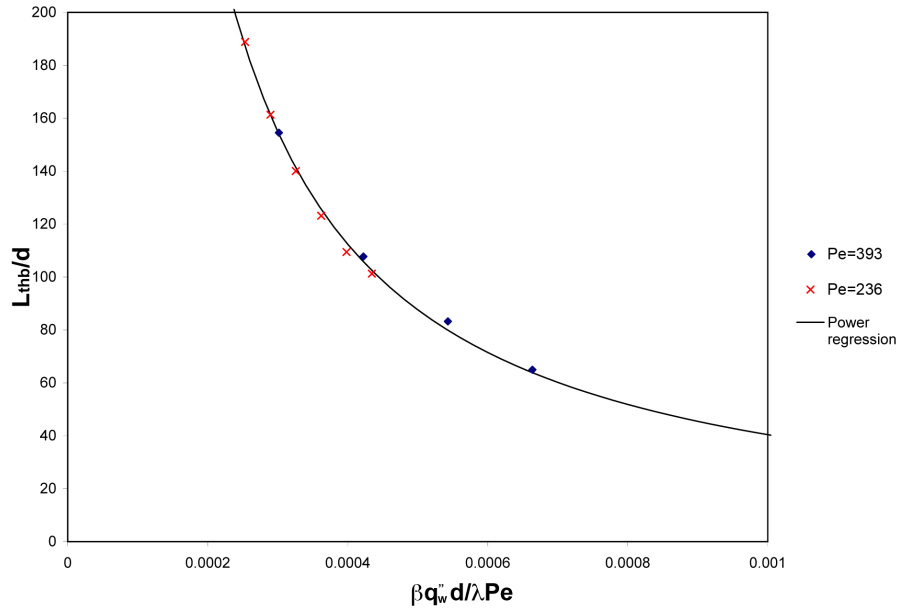


Figure 6.11: Heat transfer coefficient plotted as a function of the axial length for supercritical water (25Mpa).

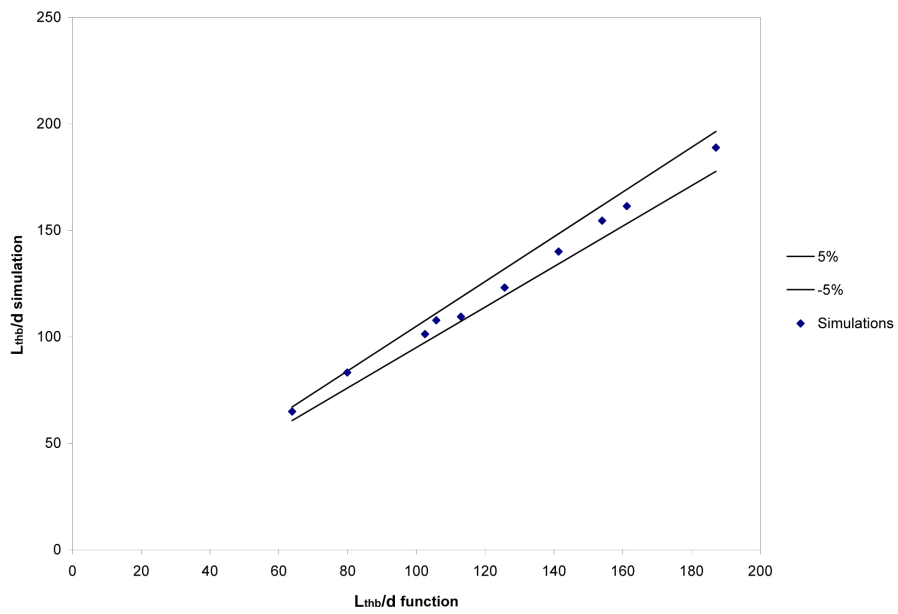


Figure 6.12: Numerical results of the supercritical water cases, plotted against equation 6.18.

6.4 Summary and discussion

With a semi-analytical model, it has been shown that in flows in which c_p increases with increasing temperature the heat transfer is enhanced and that the boundary layer thickness is decreased compared to a constant property case. For decreasing ρ with increasing temperature, the heat transfer is lower and the boundary layer thickness is increased (not considering acceleration effects). For decreasing λ with increasing temperature, the heat transfer is decreased and the boundary layer thickness is decreased.

These qualitative results have combined with literature to explain numerical results of supercritical CO_2 flowing upward through an annulus, heated by a uniform wall heat flux, with an inlet temperature lower than the pseudo-critical point. The heat transfer is increased locally due to the increase of c_p and due to flow acceleration. For higher heat fluxes and lower inlet mass fluxes (lower inlet Peclet number), the local increase shifts towards the inlet. If the heat flux is high enough, or if the inlet mass flux is low enough, the heat transfer first increases and then decreases, because c_p decreases again, even though the flow keeps accelerating. The local maximum in the heat transfer coefficient is located between the axial coordinates where $T_{wi} = T_{pc}$ and $T_b = T_{pc}$. This is consistent with literature. The value of the maximum heat transfer coefficient is increased with increasing values of q_w^* . This is different from turbulent cases reported in literature.

A relationship based on the analytical derivations was proposed for the location of the local minimum in heat transfer, determined from data gained from four different Peclet numbers at different heat fluxes. The relationship predicts the coordinate at which a minimum occurs within 5% of the numerical data. The relationship does not work well for different inlet temperatures. To include the effect of the inlet temperature, the various dimensionless groups given in equation 6.17 could be investigated. For example the effect of β , γ and ϵ could be averaged between the inlet and pseudo-critical temperatures, or bulk temperatures. Such a method, as well as the current relationships are only valid for L_{thb} if $T_{in} < T_{pc}$.

The relationship will most likely not work for turbulent cases, because it is known from literature that laminarization occurs for high heat fluxes, which causes the maximum htc to decrease.

The relevance of the newly proposed length L_{thb} can be explained as follows; the relationship gives the axial coordinate where the inlet effect disappears and where heat transfer is dominated by buoyancy and varying properties. This information might be very useful for experimental set-ups aimed at studying these effects in detail. The proposed relationship also shows that this heat transfer effect is a function of system parameters⁵, which makes it easy to use. Possibly, similar relationships can be found for the occurrence of the maximum heat transfer coefficient. Such a relationship would be very valuable in designing heat transfer equipment with supercritical fluids. From the results presented in this chapter, it seems that there is a heat flux for which the local maximum in heat

⁵inlet mass flux, wall heat flux, geometry dimension.

transfer could disappear. This critical heat flux could also be determined as a function of system parameters.

The relationship was found by using a fully developed inlet profile for velocity. This could mean that imposing a uniform velocity profile at the inlet could change the location of the local minimum in heat transfer. With the relationship from Poole[45], the development length for the lowest Reynolds number ($Re=336$) was calculated to be $x/d=7.5$. This length is well below the minimum L_{thb} that was found. Therefore, the velocity profile at the inlet will not likely change the relationship much for the investigated range of Pe and q_w'' . This was confirmed with simulations.

A mesh sensitivity analysis was performed for Case II. Two meshes of sizes (2000×100 and 1500×100) were used. The local minimum was found in both cases at almost the exact coordinates: $x/d=37.95$ and $x/d=37.93$, respectively. The fact that the development length for momentum is much smaller than L_{thb} and that a mesh sensitivity analysis was performed for a case with strong radial property gradients adds to the credibility of the relationship. A similar relationship was found for water, which shows that heat transfer in both fluids are governed by the same principles.

In the numerical simulation reported here, it was found that flow reversal can occur due to the decrease in density near the heated wall of the annulus. The smallest parameters for which flow reversal occurred in the domain were $Gr = 3.84 \cdot 10^6$, and a Peclet number of 807 at a dimensionless length of $x/d=195$. For $Gr = 9.87 \cdot 10^6$ ($Pe=807$), flow reversal occurred at $x/d=30$. This means that the length at which flow reversal occurs is a function of q_w'' . The local minimum of the heat transfer coefficient was found always upstream of the point where flow reversal occurred.

Chapter 7

Conclusions and Recommendations

For convenience, the goals stated in the introduction are repeated here:

- 1) *to investigate the thermal boundary layer thickness in laminar upward supercritical flows in an annulus*
- 2) *to find a relation between the thermal development length and the system parameters mass flux and wall heat flux.*
- 3) *to investigate the performance of OpenFOAM, with respect to modelling heat transfer to supercritical fluids.*

7.1 Thermal boundary layer development

7.1.1 Conclusions

Heat transfer to heated upward supercritical CO₂ flows at 9.52 MPa were numerically simulated with OpenFOAM in an annular geometry. A uniform heat flux was imposed on the inner wall, whereas the outer wall was considered to be adiabatic. Heat transfer phenomena were investigated for different Pe -numbers and wall heat fluxes. The inlet temperature was lower than the pseudo-critical temperature. A semi-analytical study was made to help explain the heat transfer phenomena in supercritical flows.

The heat transfer coefficient h_{tc} shows a steep decrease near the inlet after which it starts to increase again. This increase is due to the increase in specific heat capacity near the wall. This effect, together with the effect of acceleration outweigh the effect of decreasing λ and ρ (not considering the acceleration effect). Downstream of the position where $T_w = T_{pc}$, the heat transfer coefficient starts to decrease. The maximum of the heat transfer coefficient lies between the axial coordinates where $T_w = T_{pc}$ and $T_b = T_{pc}$. A higher wall heat flux results in higher radial property gradients and a smaller boundary layer thickness. The minimum in heat transfer coefficient (or onset of locally enhanced heat

transfer) shifts towards the inlet for a higher heat flux. With each increment in heat flux, this shift becomes smaller, because c_p increases faster as well near the wall. The local minimum in heat transfer can be regarded as the point where heat transfer is dominated by variable fluid properties and where the inlet effect is no longer apparent. A relation to predict the length between the inlet and this point (thermal boundary layer development length) was found. The relation predicts the numerical data mostly within 5%. A similar relation was found for supercritical water at 25 MPa. These relations do not work well for different inlet temperatures.

7.1.2 Recommendations

In the present study, the effects of variable properties in supercritical flows on heat transfer were studied. It is known from literature however, that acceleration in upward heated flows enhances heat transfer, especially if flow reversal occurs. To make the present study more complete, the acceleration effect in upward heated supercritical flows should be investigated. It was found in the present study that the point where flow reversal occurs moves to the inlet for higher heat fluxes. A relation based on system parameters could be developed to predict this. Such an investigation will possibly help to understand the effect acceleration has on heat transfer in laminar heated supercritical flows.

In order to increase the usefulness of the relations for the thermal boundary layer development length, the effect of the inlet temperature should be accounted for. A possibility for this is to create a “lumped” model. The dimensionless parameters that were identified as a result of the analytical study could serve as a starting point. The semi analytical model was based on simple parameters β , γ and ϵ , which do not represent the variation of properties well. Taking the average of these in a range of T_{in} to T_{pc} , would yield for $\gamma = \frac{c_p(T_{pc}) - c_p(T_{in})}{c_p(T_{in}(T_{pc} - T_{in}))}$. To find relations for these “lumped” parameters will take a considerable amount of time, because many parameters would have to be investigated for many different system parameters (inlet temperature, wall heat flux and mass flow). The influence of the dimensions of the geometry should also be investigated.

The difference between the heat transfer coefficient values of the local minimum and local maximum seems to become smaller for higher heat fluxes. There could be a critical heat flux for which the local minimum and maximum disappear. Such a study would provide an upper limit to the relations for the thermal boundary layer development length, but could also further help to understand the effect that variable properties have on heated supercritical flows.

7.2 OpenFOAM

7.2.1 Conclusions

In the present study, the open source CFD-package OpenFOAM was validated using cases from different authors. These cases fall into three categories: constant property, mixed convection and supercritical fluid cases. The results of the OpenFOAM code are in good to excellent agreement with the selected cases for the constant property cases. Although OpenFOAM uses only the cartesian

coordinate system, cylindrical (-coordinate) heat transfer problems in OpenFOAM have been successfully validated.

Buoyancy is accounted for in OpenFOAM via a decoupling of the total pressure into the dynamic pressure and the hydrostatic pressure. It was found that this works well for the mixed convection case that was considered.

Properties of supercritical fluids were modelled with splines, which were implemented in the OpenFOAM code with the help of boolean functions. Many cases were simulated with unsatisfactory to excellent results. This was investigated further with a parameter study. It was found that for $q^+ < 0.001$, the code gave good results.

7.2.2 Recommendations

It has not been investigated whether or not using a cartesian coordinate system for cylindrical problems is efficient. In these kind of problems, OpenFOAM solves for all three components of momentum, which should not be the case for an axisymmetric problem. Implementing a radial coordinate system for the operators in all differential equations, could reduce the total calculation time required for a fully converged solution. A mesh sensitivity analysis could be carried out in order to see which coordinate system (cartesian or cylindrical) uses less cells in order to produce a certain result. If a cylindrical coordinate system needs less cells, compared to the cartesian one, total calculation time could be reduced.

The simulations described in chapter 6 took 7 to 8 days each to run on a single processor. Using multiple processors will likely lower the total calculation time. The use of booleans in the property splines greatly increases the total calculation time. A first improvement for this is to model the heat diffusivity $K (= \frac{\lambda}{c_p})$ with a spline. The factor $\frac{\lambda}{c_p}$ can then simply be modelled by multiplying the fields ρ and K . However, a great improvement could be made by modelling the fluid properties not with splines, but a function that is valid for a large range of temperatures that are of interest. For example, a property could be written as an algebraic function in T . If such functions can be found, they should be validated against results found in literature.

New validation cases should be selected to model heat transfer to supercritical fluids, in order to investigate whether or not it is able to handle cases with q^+ well or not. The criterion for q^+ chosen in this study was based on the results of cases with high Reynolds numbers, which should not be modelled as a steady state.

Bibliography

- [1] Y. Y. Bae and H. Y. Kim, *Convective heat transfer to CO_2 at a supercritical pressure flowing vertically upward in tubes and an annular channel*, Experimental Thermal and Fluid Science **33** (2009), 329–339.
- [2] A. Barletta, *Analysis of flow reversal for laminar mixed convection in a vertical rectangular duct with one or more isothermal walls.*, International Journal of Heat and Mass Transfer **44** (2001), 3481–3497.
- [3] A. Behzadmehr, N. Galanis, and A. Laneville, *Low reynolds number mixed convection in vertical tubes with uniform heat flux*, International Journal of Heat and Mass Transfer **46** (2003), 4823–4833.
- [4] M. A. Bernier and B. R. Baliga, *Visualization of upward mixed-convection flows in vertical pipes using a thin semitransparent gold-film heat and dye injection*, International Journal of Heat and Fluid Flow **13** (1992), 241–249.
- [5] R. B. Bird, W. E. Stewart, and E. N. Lightfoot, *Transport phenomena*, 2nd ed., John Wiley & Sons, Inc., 2002.
- [6] K. C. Cheng, S. W. Hong, and G. J. Hwang, *Buoyancy effects on laminar heat transfer in the thermal entrance region of horizontal rectangular channels with uniform wall heat flux for large Prandtl number fluid*, International Journal of Heat and Mass Transfer **15** (1972), 1819–1836.
- [7] U. S. DOE Nuclear Energy Advisory Research Advisory Committee and the Generation IV International Forum, *A technology roadmap for generation iv nuclear energy systems*, 2002.
- [8] C. Dang and E. Hihara, *Numerical study on in-tube laminar heat transfer of supercritical fluids*, Applied Thermal Engineering **30** (2010), 1567–1573.
- [9] William M. Deen, *Analysis of transport phenomena*, Oxford University Press, 1998.
- [10] G. Desrayaud and G. Lauriat, *Flow reversal of laminar mixed convection in the entry region of symmetrically heated, vertical plate channels*, International Journal of Thermal Sciences **48** (2009), 2036–2045.
- [11] J. J. Duderstadt and L. J. Hamilton, *Nuclear reactor physics*, John Wiley and Sons, 1976.

- [12] R. B. Duffey and I.L. Pioro, *Experimental heat transfer of supercritical carbon dioxide flowing inside channels*, Nuclear Engineering and Design **235** (2004), 913–924.
- [13] F. Durst, S. Ray, B. Unsal, and O.A. Bayoumi, *The development lengths of laminar pipe and channel flows*, Journal of Fluids Engineering **127** (2005), 1154–1160.
- [14] K. Fischer, T. Schulenberg, and E. Laurien, *Design of a supercritical water-cooled reactor with a three pass core arrangement*, Nuclear Engineering and Design **239** (2009), 800–812.
- [15] L.F. Glushchenko, S. I. Kalachev, and O. F. Gandzyuk, *Determining the conditions of existence of deteriorated heat transfer at supercritical pressures of the medium*, Thermal Engineering **19** (1972), 107–111.
- [16] W. B. Hall and J. D. Jackson, *Laminarization of a turbulent pipe flow by buoyancy forces*, ASME paper **69** (1969), HT–55.
- [17] K. Hanjalic, S. Kenjeres, M.J. Tummers, and H.J.J. Jonker, *Analysis and modelling of physical transport phenomena*, 2nd ed., VSSD, 2009.
- [18] T. J. Hanratty, E. M. Rosen, and R. L. Kabel, *Effect of heat transfer on flow field at low reynolds numbers in vertical tubes*, Industrial & Chemical Engineering Chemistry **50** (1958), 815–820.
- [19] J. P. Holman, *Heat transfer*, 8th ed., McGraw-Hill, 1997.
- [20] J. D. Jackson, M. A. Cotton, and B. P. Axcell, *Studies of mixed convection in vertical tubes*, International Journal of Heat and Fluid Flow **10** (1989), 2–15.
- [21] P.X. Jiang, Z.P. Ren, and B.X. Wang, *Convective heat and mass transfer in water at super-critical pressures under heating or cooling conditions in vertical tubes*, Journal of Thermal Science **4** (1995), 15–25.
- [22] P.X. Jiang, Y. Zhang, Y.J. Xu, and R.F. Shi, *Experimental and numerical investigation of convection heat transfer of CO₂ at supercritical pressures in a vertical tube at low reynolds numbers*, International Journal of Thermal Sciences **47** (2008), 998–1011.
- [23] P.X. Jiang, Y. Zhang, C. R. Zaho, and R. F. Shi, *Convection heat transfer of co₂ at supercritical pressures in a vertical mini tube at relatively low reynolds numbers*, Experimental Thermal and Fluid Science **32** (2008), 1628–1637.
- [24] Fabian Peng Karrholm, *Numerical modelling of diesel spray injection, turbulence interaction and combustion*, Ph.D. thesis, Chalmers University of Technology, 2008, Appendix p. 71-76.
- [25] A. Keshmiri, *Effects of various physical and numerical parameters on heat transfer in vertical passages at relatively low heat loading*, Journal of Heat Transfer **133** (2011), 092502.

- [26] H. Y. Kim, H. Kim, D. J. Kang, J. H. Song, and Y. Y. Bae, *Experimental investigations on heat transfer to CO_2 flowing upward in a narrow annulus at supercritical pressures*, Nuclear Engineering and Technology **40** (2007), 155–162.
- [27] P. K. Kundu and I. M. Cohen, *Fluid mechanics*, 4th ed., Academic Press, 2008.
- [28] J. Licht, M. Anderson, and M. Corradini, *Heat transfer to water at supercritical pressures in a circular and square annular flow geometry*, International Journal of Heat and Fluid Flow **29** (2008), 156–166.
- [29] OpenCFD Limited, *OpenFoam source code (version 1.7.1)*, 2010, www.openfoam.com/download/source.php/.
- [30] OpenCFD Limited, *OpenFoam user guide (version 1.7.1)*, 2010, www.openfoam.com/docs/user/index.php.
- [31] G. Lorentzen and J. Pettersen, *A new efficient and environmentally benign system for car air-conditioning*, International Journal of Refrigeration **16** (1993), 4–12.
- [32] G. Lu and J. Wang, *Experimental investigation on heat transfer characteristics of water flow in a narrow annulus*, Applied Thermal Engineering **28** (2008), 8–13.
- [33] G. Lu and J. Wang, *Experimental investigation on flow characteristics in a narrow annulus*, Heat and Mass Transfer **44** (2008), 495–499.
- [34] D. P. Mikielwicz, A.M. Shehata, J.D. Jackson, and D. M. McEligot, *Temperature, velocity and mean turbulence structure in strongly heated internal gas flows. comparison of numerical prediction with data*, International Journal of Heat and Mass Transfer **45** (2002), 4333–4352.
- [35] S. Mokry, I. Pioro, P. Kirillov, and Y. Gospodinov, *Supercritical-water heat transfer in a vertical bare tube*, Nuclear Engineering and Design **240** (2010), 568–576.
- [36] A. Moutsoglou and Y.D. Kwon, *Laminar mixed convection flow in a vertical tube*, Journal of Thermophysics and Heat Transfer **33** (1993), 361–368.
- [37] M.S. Kazimi N.E. Todreas, *Nuclear systems I: Thermal Hydraulic Fundamentals*, Talor & Francis Group, LCC, 1990.
- [38] H. Nesreddine, N. Galanis, and C. T. Nguyen, *Variable-property effects in laminar aiding and opposing mixed convection of air in vertical tubes*, Numerical Heat Transfer, Part A: Applications **31** (1997), 53–69.
- [39] F.T.M. Nieuwstadt, *Turbulentie: theorie en toepassingen van turbulente stromingen*, Epsilon Uitgaven Utrecht, 1998.
- [40] A. P. Ornatsky, L. P. Glushchenko, and E. T. Siomin et al., *The research of temperature conditions of small diameter parallel tubes cooled by water under supercritical pressures*, Proceedings of the 4th International Heat Transfer Conference **VI** (1970), B 8.11.

- [41] D. Pavlidis, *Private communication*, 2011, TU Delft, faculty of Applied Sciences, section Physics of Nuclear Reactors.
- [42] B. S. Petukhov, L. G. Genin, and S. A. Kovalev, *Heat transfer in nuclear power equipment*, Energoatomizdat Press, Moscow, 1986, (In Russian).
- [43] I.L. Pioro and R. B. Duffey, *Experimental heat transfer in supercritical water flowing inside channels*, Nuclear Engineering and Design **235** (2005), 2407–2430.
- [44] I.L. Pioro, H. F. Khartabil, and R. B. Duffey, *Heat transfer to supercritical fluids flowing in channels - empirical correlations (survey)*, Nuclear Engineering and Design **230** (2004), 69–91.
- [45] R. J. Poole, *Development-length requirements for fully developed laminar flow in concentric annuli*, Journal of Fluids Engineering **132** (2010), 064501.
- [46] M. Rohde, *Private communication*, 2010, TU Delft, faculty of Applied Sciences, section Physics of Nuclear Reactors.
- [47] R.K. Shah and A.L. London, *Laminar Flow Forced Convection in Ducts*, Academic Press, 1978.
- [48] B. Shiralkar and P. Griffith, *The deterioration in heat transfer to fluids at supercritical pressures and high heat fluxes*, Tech. report, Engineering Projects Laboratory, Department of Mechanical Engineering, Massachusetts Institute of Technology, 1968, 185 pp.
- [49] H. S. Swenson, J. R. Carver, and C. R. Karakala, *Heat transfer to supercritical water in smooth-bore tubes*, Journal of Heat Transfer Trans. ASME, Ser. C 87 (4) (1965), 477–484.
- [50] H. Tanaka, S. Muruyama, and S. Hatano, *Combined forced and natural convection heat transfer for upward flow in a uniformly heated, vertical pipe*, International Journal of Heat and Mass Transfer **46** (1986), 1613–1627.
- [51] U.S. Department of Commerce, *NIST REFPROP, reference fluid thermodynamic and transport properties, database 23 version 8.0*, 2007.
- [52] Y. Vikhrev, Y. Barulin, and A. S. Kon'kov, *A study of heat transfer in vertical tubes at supercritical pressures*, Thermal Engineering **14** (1967), 116–119.
- [53] M. Wang, T. Tsuji, and Y. Nagano, *Mixed convection with flow reversal in the thermal entrance region of horizontal and vertical pipes.*, International Journal of Heat and Mass Transfer **37** (1992), 2305–2319.
- [54] B. Weigand, M. Wolf, and H. Beer, *Heat transfer in laminar and turbulent flows in the thermal entrance region of concentric annuli: Axial heat conduction effects in the fluid*, Heat and Mass Transfer **33** (1997), 67–80.

- [55] F. Xu, L. Guo, and B. Bai, *Mixed convective heat transfer of water in a pipe under supercritical pressure*, Heat Transfer - Asian Research **34** (2005), 608–619.
- [56] K. Yamagata, K. Nishikawa, S. Hasegawa, T. Fujii, and S. Yoshida, *Forced convective heat transfer to supercritical water flowing in tubes*, International Journal of Heat and Mass Transfer **15** (1972), 2575–2593.
- [57] J. You, J. Y. Yoo, and H. Choi, *Direct numerical simulation of heated vertical air flows in fully developed turbulent mixed convection.*, International Journal of Heat and Mass Transfer **46** (2003), 1613–1627.
- [58] E. H. Zaim and G. Nassab, *Numerical investigation of laminar forced convection of water upwards in a narrow annulus at supercritical pressure*, Energy **35** (2010), 4172–4177.

Appendix A

Code excerpts

A few excerpts of the code are shown and explained here. The particular excerpts work only for an annular geometry.

Listing A.1: Declaration of a variable

```
1  volScalarField T
2  (
3      IOobject
4      (
5          "T",
6          runtime.timeName(),
7          mesh,
8          IOobject::MUST_READ,
9          IOobject::AUTO_WRITE
10     )
11     mesh,
12 );
```

Variable T is defined as a volumetric scalar field. `volScalarField` is an OpenFOAM class, whereas T an object. Line 5 to 11 tell OpenFOAM to look for dictionary T (in which the boundary conditions and the initial field values are set), tie T to specific iteration (time) and cells, to read and write T at a specific iteration (as specified in `controlDict`) and finally (line 11), to use the values given in the mesh at the start of the code.

Listing A.2: Momentum equation

```
1  volTensorField gradU = fvc::grad(U)
2
3  tmp<VectorMatrix> UEqn
4  (
5      fvm::div(phi, U)
6      - fvm::laplacian(mu, U)
7      - fvc::div(mu*gradU.T() - scalar(2)/scalar(3)
8        *mu*tr((gradU.T()))*I)
9  );
10
```

```

11 UEqn().relax();
12
13 eqnResidual = solve
14 (
15     UEqn
16 ==
17     fvc::reconstruct
18     (
19         fvc::interpolate(rho) * (g & mesh.Sf()) -
20         (fvc::snGrad(p))*mesh.magSf()
21     )
22 ).initialResidual();

```

`fvc::` is a OpenFOAM class which is used in explicit discretization, whereas `fvm::` is reserved for implicit discretization. After `fvc::` or `fvm::` comes a function, which corresponds to a physical operator, such as a gradient, divergence or laplacian operator. Tied to these functions are the various discretization scheme functions, which are selected in the dictionary `fvSchemes`. `interpolate` means that the function is evaluated at the cell *face*. `mesh.Sf()` is a surface vector and `mesh.magSf()` is its magnitude. Thus, buoyancy and pressure terms are evaluated at the cell faces. The `reconstruct` function transforms the cell face values into cell centred values. The member function `.relax()` under-relaxes the momentum equation, as specified in the dictionary `fvSolution`. Line 13 and 22 represent the solver method, as selected in the dictionary `fvSolution`.

The other equations that are solved for use the same classes and functions.

Listing A.3: Wall heat flux BC

```

1  label innerWallID =
2      mesh.boundaryMesh().findPatchID("innerWall");

3  fixedGradientFvPatchScalarField& innerWallH =
4      refCast<fixedGradientFvPatchScalarField>
5      (h.boundaryField()[innerWallID]);

6  scalarField& gradHInnerWall = innerWallH.gradient();

7  scalarField& cpIW = cp.boundaryField()[innerWallID];

8  scalarField& lambdaIW =
9      lambda.boundaryField()[innerWallID];
10
11 forAll(gradHInnerWall, faceI)
12 {
13     gradHInnerWall[faceI] = q.value() /
14         lambdaIW*cpIW[faceI];
15 }

```

In the `blockMesh`¹ dictionary, the boundary face values are labelled; in this case the inner wall of an annulus is labelled as `innerWall`. For a uniform wall heat flux in variable property flow, the gradient (equation 4.18) face value at the inner wall has to be updated each iteration. Line 1 finds this label and gives it a different label inside the code: `innerWallID`. In the second line an object is created containing (amongst other information) the normal gradient face values of the boundary labelled `innerWallID`. The gradient face values are of interest here; these are put in a new object: `gradHInnerWall` (of class `scalarField`). The same is done for the values of λ and c_p at the wall. In wall line 11-14, the gradient face values for h are calculated, based on the local values of c_p and λ . `q` is a previously specified object of the class `dimensionedScalar` (it has multiple members, of which the member `value` is used here).

The inlet boundary conditions for velocity were made in a similar way, but with few different steps in the beginning. To *access* the coordinate y , for example, the following is used: `y = (mesh.C()).component(1);`, in which `.C` is used to get the cell centred values. In this case, `y` must be declared as described above in the beginning of this chapter.

Listing A.4: Spline implementation

```

1  forAll (mesh.cells(), i)
2      {
3          rho[i] =
4              #include "estrhoater.H"
5          cp[i] =
6              #include "estcpwater.H"
7          lambda[i] =
8              #include "estlambdewater.H"
9          mu[i] =
10             #include "estmuwater.H"
11         T[i] =
12             #include "esthwater.H"
13     }

```

The fluid properties and the temperature field are updated here for all cells within the mesh. The header(.H) files contain the actual spline functions. The variable properties at the boundaries are calculated in a similar manner, by looping over the boundary cell face values.

Listing A.5: Density spline `estrhoater.H`

```

1  (
2      (
3          1.0876e-10 * pow((h[i]-103070),3)
4          -2.0933e-010 * pow((h[i]-103070),2)
5          -6.13213e-005 * (h[i]-103070)+1009.6
6      ) * bool(103070<=h[i]) * bool(h[i]<201900)
7      +(...)
8  );

```

¹This is where the mesh is specified

`pow(a,b)` is a^b . `bool` is a boolean. `h` here has an index according to the loop described above. (...) stands for the rest of the spline function.

Listing A.6: Calculation of *htc*

```

1  float SUM [NL];
2  float NORM [NL];
3
4  scalarField TUA = rho*cp*U.component(2)*T;
5
6  fvPatchScalarField Tbw =
7      refCast<fvPatchScalarField>(Tb.boundaryField()
8          [lowerWallID]);
9  fvPatchScalarField Twall =
10     Tb.boundaryField()[lowerWallID];
11 fvPatchScalarField htcWall =
12     htc.boundaryField()[lowerWallID];
13
14 forAll (Tbw,j)
15 {
16     forAll (mesh.cells(),i)
17     {
18         if (z[i] <- (j+1)*dZ)
19         {
20             if (z[i] > j*dZ)
21             {
22                 SUM[j] += TUA[i]*y[i];
23                 NORM[j] += (U.component(2)
24                     *rho[i]*cp[i]*y[i]);
25             }
26         }
27     }
28     Tbw[j] = SUM[j]/(NORM[j]+1e-10)
29     htcWall[j] = q.value()/(Twall[j]-Tbw[j]+1e-10);
30 }
31
32 Tb.write();
33 htc.write();

```

The first two lines create two arrays with a length `NL` (which contain floats). `NL` must be larger than or equal to the total number of cells in the length of the geometry in order to avoid a *segmentation fault*. In the lines 2-11, help variables are created to make the code to calculate *htc* look more clear. In line 10, a loop is created to go through the coordinate *z*. In the second loop, the *z*-coordinate is checked against that of the primary loop. If there is a match, $\int \rho c_p U T dr$ is calculated as a sum, as well as $\int \rho c_p U dr$. To avoid any *floating point exceptions*, `1e-10` has been put in each denominator. In the last two lines, the values of the wall temperature and the heat transfer coefficient are written in the variable dictionaries `Tb` and `htc`. The friction factor and the wall shear stress are calculated in the same manner.